Dissertations, Theses, and Masters Projects   Theses, Dissertations, & Master Projects

2003

A semi-empirical cellular automata model for wildfire monitoring from a geosynchronous space platform

Brian D. Killough
College of William & Mary - Arts & Sciences

Follow this and additional works at: https://scholarworks.wm.edu/etd

Part of the Aerospace Engineering Commons, Applied Mechanics Commons, Forest Sciences Commons, and the Remote Sensing Commons

A SEMI-EMPIRICAL CELLULAR AUTOMATA MODEL FOR WILDFIRE

MONITORING FROM A GEOSYNCHRONOUS SPACE PLATFORM

————————

A Dissertation

Presented to

The Faculty of the Department of Applied Science

The College of William and Mary in Virginia

In Partial Fulfillment

Of the Requirements for the Degree of

Doctor of Philosophy

————————

by

Brian D. Killough, Jr.

May 2003

APPROVAL SHEET

This dissertation is submitted in partial fulfillment of

the requirements for the degree of

Doctor of Philosophy

Brian D. Killough, Jr.

Approved, May 2003

Mark K. Hinders
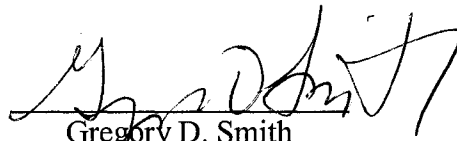
Gregory D. Smith
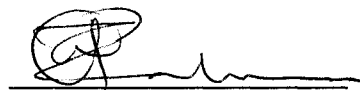
Zia-ur Rahman
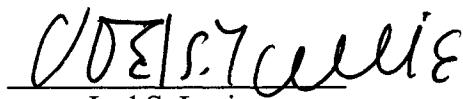
Joel S. Levine
NASA Langley Research Center

ii

TABLE OF CONTENTS

ACKNOWLEDGEMENTS

This dissertation benefited from the critical review of committee members, Dr. Mark K. Hinders, Dr. Gregory D. Smith, Dr. Zia-ur Rahman, and especially from the support and guidance of my research advisor, Dr. Joel S. Levine. Critical data was provided by Jianmei Pan of Rockwell Science Corporation for Chapter I, by Richard E. Davis of the NASA Langley Research Center for Chapter II, and by Frances Fujioka of the USDA Forest Service for Chapter III. I am grateful to all of them for their help.

I would like to thank Dr. Joel S. Levine for his patience and support in my quest for a research topic, and Steven P. Sandford and Barry D. Meredith for their support and consistent desire to see me succeed.

Finally, I would like to thank my wife Cynthia and my children Courtney and Laura. Their encouragement to reach this goal in the midst of a busy family life is greatly appreciated.

LIST OF TABLES

LIST OF FIGURES

vii

viii

x

ABSTRACT

The environmental and human impacts of wildfires have grown considerably in recent years due to an increase in their frequency and coverage. Effective wildfire management and suppression requires real-time data to locate fire fronts, model their propagation and assess the impact of biomass burning. Existing empirical wildfire models are based on fuel properties and meteorological data with inadequate spatial or temporal sampling. A geosynchronous space platform with the proposed set of high resolution infrared detectors provides a unique capability to monitor fires at improved spatial and temporal resolutions. The proposed system is feasible with state-of-the-art hardware and software for high sensitivity fire detection at saturation levels exceeding active flame temperatures. Ground resolutions of 100 meters per pixel can be achieved with repeat cycles less than one minute. Atmospheric transmission in the presence of clouds and smoke is considered. Modeling results suggest fire detection is possible through thin clouds and smoke. A semi-empirical cellular automata model based on theoretical elliptical spread shapes is introduced to predict wildfire propagation using detected fire front location and spread rate. Model accuracy compares favorably with real fire events and correlates within 2% of theoretical ellipse shapes. This propagation modeling approach could replace existing operational systems based on complex partial differential equations. The baseline geosynchronous fire detection system supplemented with a discrete-based propagation model has the potential to save lives and property in the otherwise uncertain and complex field of fire management.

A SEMI-EMPIRICAL CELLULAR AUTOMATA MODEL FOR WILDFIRE

MONITORING FROM A GEOSYNCHRONOUS SPACE PLATFORM

INTRODUCTION

The impact of wildfires on property and human life is significant. According to the National Fire Data Center (www.usfa.fema.gov), the U.S. has one of the highest fire death rates in the industrialized world. In 1999, over 3500 Americans lost their lives as the result of fire. Furthermore, fire kills more Americans than all natural disasters combined. According to the National Interagency Fire Center (www.nifc.gov), there were 122,827 wildfires in the U.S. in 2000, accounting for over 8.4 million acres of burned land. There were as many as 86 large fires active in one day, which is officially defined as a fire that covers an area of 100 acres or more. The estimated yearly cost of fire suppression was $1.3 billion. It is likely that the fire season of 2000 will be one of the worst recorded seasons in history. Since that time there has been a slight reduction in wildfire activity, but the impact on lives and property continues to be substantial. Thought this example refers to wildfires in the U.S., the problem is not constrained locally, but extends globally. The ability to save lives and decrease fire suppression costs on a global basis are worthy goals of any fire management approach and one of the motivations for this research.

Though wildfires have a significant impact on property and human life, the impact of global biomass burning on the Earth's atmosphere cannot be overlooked. The trace gases emitted during the biomass burning process are responsible for changes in gas cycling, photochemistry, greenhouse gas production, acid rain deposition, and aerosols

that influence cloud behavior. The emission rates of these gases are not well known on a global and yearly basis. As the distribution and duration of biomass burning has increased, so has the release of emission products, and their corresponding impacts on the environment and climate (Penner et al., 1992; Andreae, 1991; Crutzen and Andreae, 1990). Trace gas and aerosol emissions are dependent on the biomass fuel type, the intensity of the fire, and the duration of the combustion process (Lobert and Warnatz, 1993). The amount of time spent in flaming versus smoldering conditions directly impacts emission rates (Cofer et al., 1996). At present, it is commonly assumed that the time spent in each phase is 50 percent (Levine, 1991). Accurate emissions models require detailed knowledge of fire events that does not currently exist. A dedicated fire monitoring satellite would allow these measurements over local regions to improve model correlation and assess future impacts on the environment. According to the USDA Forest Service National Strategic Plan (Anon, 1999), emission models should be linked to models of fire behavior in a geographically resolved system and provide for aggregation or scaling to all spatial scales. Quantitative information about the spatial and temporal distribution of fires is critical to fire ecology and management, atmospheric chemistry and forestry (Levine, 1991). In order to effectively manage and suppress a wildfire, the behavior of the fire must be predictable. This research will introduce a method to acquire temperature and propagation histories of fires that will directly benefit fire management and biomass emission models.

The study of biomass burning and its impacts is an important and diverse problem. NASA is particularly interested in studying fire extent and severity to evaluate the impact on global warming (Levine et al., 1995). For example, NASA Langley

Research Center submitted a proposal for the first dedicated space-based fire monitoring system called "FireSat" in response to the NASA Office of Earth Science Announcement of Opportunity for the Earth System Science Pathfinder (ESSP) Mission in 1996 (Levine et al., 1996a). According to NASA's Earth Science Enterprise Research Strategy Plan (www.earth.nasa.gov), which defines the strategic vision for the next 10 years, one of the primary research themes is "Biology and Biogeochemistry of Ecosystems and the Global Carbon Cycle". Fire may produce as much as 40% of the global annual production of CO_2 (Levine, 1994, 2001; Levine et al., 1997a), which is the overwhelming greenhouse gas in our atmosphere. Another impact of biomass burning is the direct and indirect impacts of smoke aerosols on climate (Kaufman and Fraser, 1997; Hobbs et al., 1997; Christopher et al., 1996, 1998). Smoke aerosols from biomass burning directly impact the radiative balance by increasing reflected shortwave radiation and indirectly impact the radiative balance by acting as cloud condensation nuclei to precipitate the formation of cloud particles. The combination of these two impacts yields a net radiative cooling that may be comparable to the net radiative warming due to atmospheric carbon dioxide (Houghton, 1990). Finally, global biomass burning also impacts the biogeochemical cycling of nitrogen and carbon gases from the soil to the atmosphere (Levine et al., 1997b). Recent NASA studies of the nitrogen and carbon budget (Levine et al., 1996b) suggest improved fire detection is required to assess biogeochemical cycling with adequate accuracy. With a global increase in the occurrence of biomass burning, there will certainly be a corresponding increase in the release of emission products and their detrimental impact on our environment and climate. Aside from the secondary processes of chemistry and climate change, one cannot underestimate the direct human health

problems associated with fire. The World Health Organization (www.who.int) has identified particulates and gases emitted from fires as detrimental to human health and the cause of human respiratory problems (Levine, 2000). Each of the aforementioned problems can directly benefit from improved fire research as we learn more about biomass burning processes and the extent of their scientific and human influence.

One can envision a geosynchronous space satellite 35,000 kilometers (km) above the Earth monitoring the U.S. for active fires at a resolution of 100 meters. A large fire, greater than 100 acres, is detected in the West. The infrared (IR) detector system scans toward the fire and focuses on the scene to obtain time-dependent temperatures as the fire propagates quickly toward a community. Scene information is correlated with a Geographical Information System (GIS) to precisely locate the fire on land maps. These empirical temperature data are used as inputs to a cellular automata model that quickly predicts the future propagation of the fire. The results are processed on-orbit and then relayed to firefighters in the field within minutes of the last measurement. Fire managers are able to efficiently deploy and adjust resources ahead of the moving fire front in an effort to control the fire. Post-fire data are compiled by atmospheric scientists to determine the biomass burning emissions during the event and the overall impact to the atmosphere and land. Temperature histograms over the entire fire scene allow correlation with emission models to predict the gaseous emissions. These emissions are further used in climate change models to assess the impact of biomass burning on our atmosphere. All of these products are possible with a dedicated set of instrumentation and algorithms. Though futuristic in its approach, the results are achievable with minor improvements in technology and modeling.

No satellite currently exists with the direct intention of providing real-time data and fire modeling results for scientific and fire management purposes. The existing data for fire modeling and management comes from aircraft operations or as a secondary product from earth observing satellites. In all cases, these data sets are either insufficient in spatial or temporal sampling to provide useful information. In the case of aircraft operations, the local spatial sampling is excellent as the aircraft is typically flown at low altitudes with high-resolution sensors, but the coverage is poor as the aircraft is only able to cover limited ground within the allotted flight time. Temporal sampling of aircraft is better than low-altitude spacecraft, but still lacks suitable repeatability over all parts of the fire to develop accurate propagation measurements. An Earth observing spacecraft has a different set of concerns. The spatial sampling is broad, in that the ground footprint can cover an area much larger than an aircraft, but the ability to achieve adequate coverage for fire detection and growth monitoring depends on the orbit. Low-Earth orbit satellites have limited orbit repeat cycles so their temporal sampling is limited. Geosynchronous orbits provide the best combination of spatial and temporal sampling, but they have yet to provide a consistent global data product (Prins and Menzel, 1994). Though global coverage is not achievable for locating wildfires throughout the world with one satellite system, adequate regional ground resolution can be obtained with a dedicated geosynchronous system. Ideally, a family of geosynchronous satellites could be used to provide continuous monitoring of major parts of the Earth's land surface, but the cost of such a system of satellites would be prohibitive. Providing a constant Earth view is the temporal benefit of a geosynchronous orbit and an essential requirement for

fire detection and propagation monitoring. This baseline geosynchronous approach will serve as the focus of this research.

The presented research is separated into three chapters: (I) Fire Detection, (II) Radiation Modeling, and (III) Propagation Modeling. Chapter I. (Fire Detection) presents a review and comparison of existing satellite systems, presents a detector system uniquely suited for geosynchronous applications, and defines the resolution capabilities of such a system for identifying and tracking fires. Chapter II. (Radiation Modeling) focuses on the selection of infrared wavelengths for active fire detection, presents a method for fire scene identification and assesses expected detector performance and measurement degradation due to clouds and smoke. Chapter III. (Propagation Modeling) presents a review and comparison of existing fire propagation models, presents a new cellular automata model and compares the model to theoretical ellipse shapes and to real fire events. In summary, this research defines and analyzes the performance of a remote sensing fire detection system for geosynchronous orbit and presents a specific propagation modeling application suitable for the fire management community. Such a system would be superior to existing space-based and ground-based systems and has the potential to significantly contribute to future fire research and benefit the fire management community.

CHAPTER I. FIRE DETECTION

Fire Detection from Space

Several satellites currently provide data for fire monitoring and assessment. Their capabilities vary considerably in terms of spatial resolution, temporal resolution, spectral bands, and temperature saturation threshold (Table 1-1). In all cases these satellite systems are tailored for radiation studies not directly focused on fire detection and monitoring. The fire monitoring capabilities of these systems are a secondary benefit that has been increasingly realized over time. Up to now, only the extent of fires has been measured from satellites, but detailed information vital for fire fighting is needed from these space-based systems. Data from future space-based sensors can be integrated with resources on the ground for effective fire management. Until that goal is realized, there will be significant shortcomings in science data for fire research.

8

Satellite	Instrument	Detector Wavelength (um)	Detector Saturation (K)	Spatial Resolution (m/pixel)	Temporal Repeat Cycle
NOAA-9	AVHRR (1)	3.7	327	1000	9 days
GOES	VAS (2)	3.9	335	13800	Continuous
EOS	MODIS (3)	4.0	500	1000	16 days (4)
Research	Research	3.6	1800	100	Continuous

Table 1-1. Summary of fire detection capabilities from space. Saturation temperature and spatial resolution are key improvements over existing platforms. References: (1) Kennedy et al., 1994; (2) Prins and Menzel, 1992; (3) Kaufman and Justice, 1998; (4) Killough, 1997.

The current satellite system most often used to detect fires is the NOAA Polar Orbiting Satellite and the Advanced Very High Resolution Radiometer (AVHRR) instrument. The most recent NOAA satellite (NOAA-12) started instrument operations on September 17, 1991 (Kennedy et al., 1994). All of the NOAA satellites are in near-polar sun-synchronous 833-870 km orbits with various equator crossing times. Satellites 7, 9, and 11 have ascending orbit crossing times in the early afternoon (2:30 pm) and satellites 6, 8, 10, and 12 have orbit crossing times later in the day at 7:30 pm. Though intended for clouds and aerosol research, the instrument has been increasingly used for biomass burning detection. Fire detection using AVHRR data has been well studied (Robinson, 1991; Giglio et al., 1999; Kaufman et al., 1990; Matson et al., 1987). Spectral channels in the visible, near-IR and thermal-IR allow detection of active fires and associated background regions. Ground resolution can approach 1-km for Local Area Coverage (LAC) data sets and 4-km for Global Area Coverage (GAC) data sets.

Researchers use various spectral combinations to identify fire scenes and discriminate smoke from fire (Kaufman and Justice, 1998).

The GOES satellite uses a 5-channel imaging radiometer in geosynchronous orbit. This orbit remains fixed over the Earth in a constant position, thus providing the needed temporal resolution over the critical fire regions of the United States (U.S.). The major disadvantage with the current system is the limited spatial resolution (13.8 km) in the mid-IR fire channel. This data set has been used by Prins and Menzel (1992, 1994) to study fire scenes in South America over large scale areas using an Automated Biomass Burning Algorithm (ABBA).

The EOS-TERRA platform (launched December 18, 1999) and the EOS-AQUA platform (launched May 4, 2002) will provide a multi-spectral narrowband radiometer (MODIS) for biomass burning detection. This instrument is well suited to studying the impacts of biomass burning on a global basis due to sun-synchronous polar orbits with equatorial crossing times of 10:30 a.m. and 1:30 pm, respectively. Specific MODIS fire data products will be available from the EOS-TERRA and EOS-AQUA spacecraft (Kaufman and Justice, 1998). The MODIS fire products use the 1 km resolution channels at 3.9 μm and 11 μm with improved saturation levels of 500K and 400K, respectively, to detect active fires. Fire observations will be made two times a day from the TERRA platform (10:30 am and pm) and four times a day when the AQUA platform (1:30 pm and 1:30 am) is also in orbit. These MODIS data products build on heritage algorithms for operational fire monitoring used with the GOES and AVHRR sensors. The MODIS fire products provide information on the location of a fire, its emitted energy, the flaming to smoldering ratio, and an estimate of area burned. MODIS cloud masks will be used to

detect cloud contamination of the scene. This MODIS data set will be the most comprehensive fire data product available in the near future.

There have been a few other attempts to utilize existing instrumentation for fires. These include the Defense Meteorological Satellite Program (DMSP) Optical Linescan System (OLS) and the Visible and Infrared Scanner (VIRS) on the Tropical Rainfall Measuring Mission (TRMM). The DMSP OLS instrument possesses a wide swath, high overpass frequency measurement in the visible to near infrared (0.58 to 0.91 μm) for active fire monitoring. Due to the limited capability to accurately distinguish fires from solar contamination, it has primarily been used to supplement nighttime verification of AVHRR fire measurements (Fuller and Fulk, 2000). The VIRS instrument has been recently used for remote sensing of fires and the study of smoke aerosols (Giglio et al., 2000; Rosenfeld, 1999). The TRMM platform was launched on November 28, 1997 with a 350 km altitude and a 35 degree inclined orbit (Kummerow et al., 1998). This platform covers the mid-latitude regions with a precessing orbit that allows sufficient diurnal sampling. The VIRS narrowband radiometer has five sensor channels that are similar to those used by AVHRR, but with a lower instantaneous field-of-view (IFOV) limited to 2.11 km. Though relatively new to the fire detection community, VIRS data will likely be studied in more detail and supplement future fire detection research.

This research considers a geosynchronous satellite system for fire monitoring due to its continuous temporal sampling. In order to achieve high spatial resolution, one must consider the optical design constraints of large primary mirror structures. Ground resolution from a geosynchronous platform is primarily limited by diffraction at the edge of optical components. This is commonly referred to as diffraction-limited resolution.

For a satellite at altitude h, the ground resolution at nadir is a function of the aperture or

primary mirror size D and wavelength λ (Wertz and Larson, 1999):

$$X = \frac{2.44\, h\, \lambda}{D} \qquad (1\text{-}1)$$

In the case of a geosynchronous satellite with an infrared detector at 3.7 μm, the primary

mirror diameter would be 3.2 meters for a ground resolution of 100 meters. Though this

may seem large for existing Earth monitoring systems, one should consider the 2.4 meter

diameter of the Hubble Space Telescope (HST). This is currently the largest unclassified

primary mirror structure in space. Advancements in technology could lead to future

space telescopes that are 100 times larger than HST, or on the order of 250 meters in

diameter. These large structures will certainly require lightweight, deployable, thin-film

technology advancements that may be in their early stages, but have already captured the

interest of NASA officials and the remote sensing community (www.sandia.gov). The

Next Generation Space Telescope (NGST) Project, located at NASA Goddard Space

Flight Center has projected that the active primary mirror for its next planned mission in

2009 will be nearly 8 meters in diameter and capable of deploying on orbit

(www.gsfc.nasa.gov). This primary mirror diameter would allow ground resolutions

better than 33 meters per pixel for future fire monitoring. For the purpose of this

research, a ground resolution of 100 meters per pixel will be assumed. This order of

magnitude improvement in spatial resolution will allow detection of many fires in their

earliest stages of growth that would otherwise be undetected by existing space systems.

Detector Approach

The specific wavelength bands for the two detectors in this research will be shown in Chapter 2 (Radiation Modeling). At this point, the detector system along with its operational constraints and performance will be discussed.

The detector system will consider a pixel ground resolution of 100 meters by 100 meters. Therefore, each pixel corresponds to a ground area of one hectare (ha), which is commonly used by fire researchers to describe burn areas. It is anticipated that the instrument would be focused on the continental U.S. as its primary target. The total area of the U.S. is approximately 960 megahectares (Mha) or 3.8 million square miles. This assumes an approximate North-South dimension of 2400 km and an approximate East-West dimension of 4000 km. It is anticipated that scanning the entire country continuously is not necessary. Rather, one would scan smaller portions of the country to look for critical fire events in locations that have been defined as fire hazards. Once located, the instrument could focus its attention on the active fire event to obtain critical temperature and time history data of the fire scene. In any case, it is obvious there are many approaches to fire monitoring that are both desirable and feasible. Several of these operational cases are presented below.

A recent survey of infrared detector capabilities was conducted by Rockwell Scientific (Pan, 2002) to evaluate focal plane array concepts using Mercury-Cadmium-Telluride (HgCdTe) materials. It was determined that several candidate detectors exist

for fire applications, but careful consideration must be given to focal plane array format, operating temperature, scanning methods and pixel integration time. A numerical model (Tennant and Cabelli, 1998) was used to perform parametric studies of these variables to identify a baseline approach that is both feasible and optimal for geosynchronous fire detection. The model was developed applying Planck's Law, semiconductor physics, HgCdTe material properties and other physical device parameters to calculate signal-to-noise (SNR) ratio as a function of detector temperature, scene temperature and integration time. No attempt was made to significantly alter the model, but numerous cases were studied to develop a baseline approach for the presented research. The remaining content of this chapter will present the results of these parametric studies and discuss their implications for fire detection.

As previously mentioned, the goal of this research is to develop a fire propagation model which relies on effective identification and detailed knowledge of the fire scene at any location in the U.S. Three separate approaches could be considered for mapping the country: staring, scanning or nutating (Figure 1-1).

Staring **Scanning**
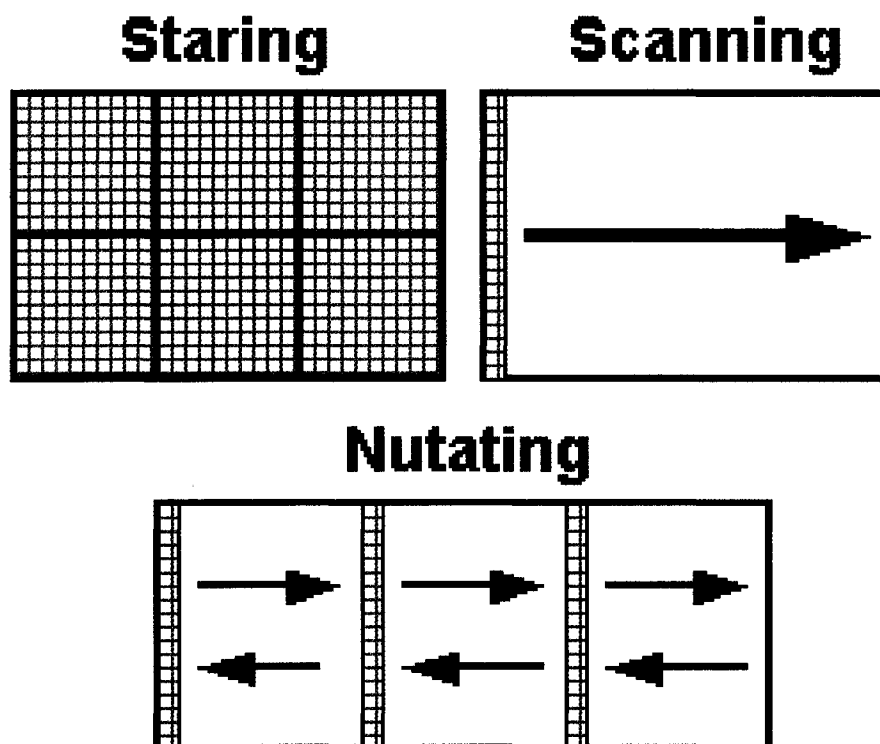
Nutating

Figure 1-1. Various operational scanning methods can be used for infrared fire detectors. The nutating method is a compromise between staring and scanning that enhances performance and reduces engineering complexity.

The staring approach would use large format arrays to stare at large ground footprint areas and move those arrays consecutively from one scene to the next to obtain full ground coverage. Though large arrays are available (Cabelli et al., 2000) there are operational issues that prohibit large charge capacity and fast refresh times, as well as mechanical concerns with moving across the scene. With a typical 1000 x 1000 pixel array, it would require 960 footprints to cover the U.S. (assuming a 2400 km x 4000 km total area) at 100 meter pixel resolution. With a detector integration time of 20 milliseconds (ms), it is possible to cover the U.S. in approximately 19 seconds, not accounting for oversampling or mechanical lag. The real problem with this approach

appears to be the mechanical complexity of stopping and starting the detector optical system. Mechanical lag and oversampling would certainly increase coverage time. For comparison purposes, the large fires experienced in Yellowstone National Park in 1988 (Rothermel et al., 1994) occupied a total burn area of 683,305 ha, with individual fire cells as large as 59,685 ha (September 9 for North Fork Fire cell). The staring footprint could easily acquire measurements for an entire fire scene of this magnitude. This particular fire would have occupied 68% of the total instrument footprint with a pixel resolution of one hectare.

Another approach is linear scanning using long and narrow arrays (1000 x 1). Considering a detector integration time of 20 ms and 2 times oversampling, one could scan the U.S. in 16 minutes, with this method. The advantages of this system are more efficient packaging and higher charge capacity which increases saturation levels and detector sensitivity. Obviously, the drawback to this approach is the slower coverage rate.

The nutating approach is an excellent compromise to scanning and staring. A matrix of linear or square arrays can be arranged such that each element nutates around its center point to allow for redundancy in sampling. Nutation can be accomplished by smoothly rotating the optical assembly in a circular or sweeping pattern. Redundancy could be obtained either by over scan (with appropriate increase in scan time) or by adding additional detectors in a time delayed integration mode. The nutating mode would provide high scene refresh rates while avoiding mechanical complexity in motion. The large detector spacing allows designs with high charge capacity and has the potential for multi-band detectors. From geosynchronous orbit, this nutation approach requires +/-

3.28 degrees of total slew angle to cover the boundaries of the U.S. The nutating approach can also produce repeatable coverage rates approaching one minute, which is desired and appropriate for monitoring fire progression and temperature history. According to Merrill and Alexander (1987), the nominal flame front residence time for forest fires is 30 to 60 seconds. This is the length of time for the flaming zone or front to pass a given point. Refresh or repeat cycle times near one minute would certainly accommodate these residence times and allow active tracking of fire front position.

Detector temperature is another consideration that must be carefully considered in the implementation process. Theoretically, it is possible to detect active fires with room temperature detectors near 300K, and these FPA devices do exist (Tennant and Cabelli, 1998). The larger issue becomes detector sensitivity and integration time. Room temperature detectors possess high dark current (inherent device current) that may exceed the photon current of the scene. In this case it is difficult to resolve the background scene temperature. The example in Figure 1-2. uses a 100-meter square fire (1 hectare) at 1000K to show the impact of detector temperature on dark current and SNR.
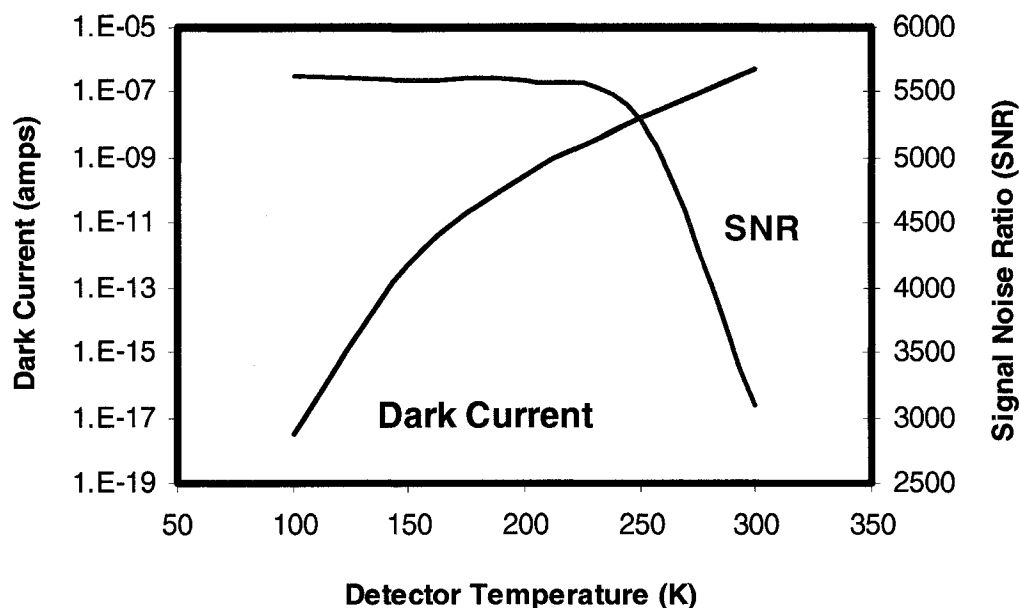
Figure 1-2. Detector dark current and SNR vs. detector temperature. Detector temperatures above 250K suffer severe degradation in SNR and increases in dark current. Assumes 3.4 to 3.8 um detector wavelength, 1000K fire, 1ha fire area, 300K background, 20μs detector integration.

These results suggest a detector temperature near 200K provides optimum SNR. Furthermore, the implications of cooling to 200K are not prohibitive. Active cryocooling is not required for this level of cooling, but thermoelectric cooling (TEC) can easily achieve 200K. These mature devices are typically configured in multistage dewars to produce intermediate cryogenic temperatures of 190K to 200K (Chorier and Tribolet, 2001).

Two important parameters affecting detector performance are signal charge capacity and integration time. These parameters directly impact SNR performance, saturation temperature and overall sensitivity to low temperature fires. For effective fire detection it is desired that SNR be greater than 10 to allow at least one order of magnitude signal to noise separation and thus adequate resolution of a fire signal.

Detector saturation temperature should exceed 1300K to resolve the hottest active fires scenes (Vines, 1981). Finally, low-temperature smoldering fires near 500K (Chandler et al., 1983) should be adequately resolved. Variations in signal charge capacity and integration time can achieve these objectives.

The state-of-the-art 1000 x 1000 infrared detector array has an electron charge capacity of 2.0E+07 electrons, without complex and untested techniques for dynamic range adjustment (Pan, 2002). It is possible to achieve higher capacities of 2.0E+08 for linear arrays (1000 x 1) with future capabilities even approaching 2.0E+09. This order-of-magnitude improvement in charge capacity will result in higher SNR for fire scenes (Figure 1-3).
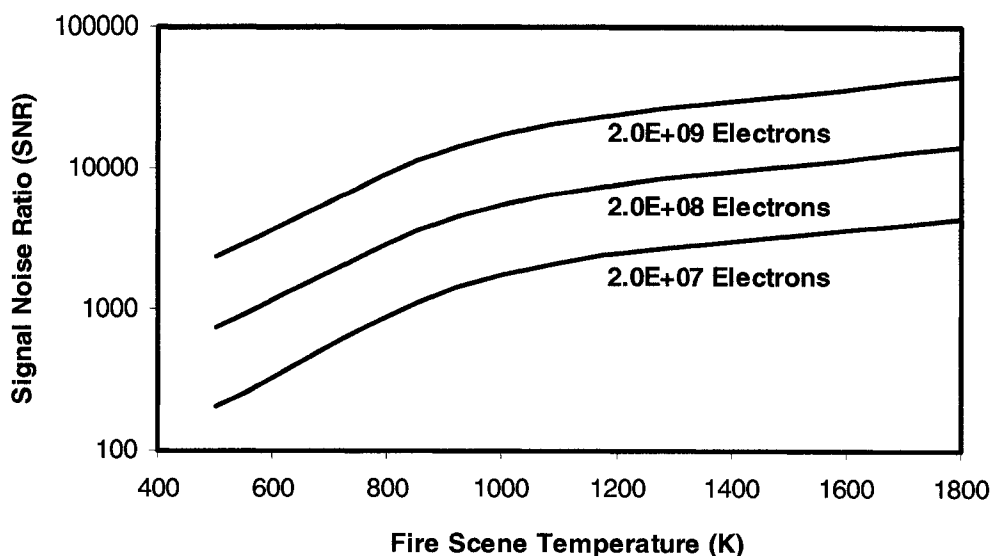
Figure 1-3. Detector SNR vs. fire scene temperature for detector electron charge capacities of 2.0E+07 to 2.0E+09. Improvements in electron charge capacity greatly enhance SNR over typical fire scene temperatures. Assumes 3.4 to 3.8 um detector wavelength, 200K detector, 1ha fire area, 300K background, 20μs detector integration.

Another parameter impacting detector performance is pixel integration time. This is the cycle time required to discharge the detector capacitor and remove the absorbed electron charge from incident scene radiation. Optimal integration time requires system tradeoffs considering detector architecture and operational strategy. The current technology allows integration times between 2 microseconds (μs) and 20 ms for square staring arrays. Faster integration times and even variable integration times are possible with linear arrays that allow more space for electronics. Faster integration times and high charge capacity allow high saturation temperatures necessary for detection of active fires. Figure 1-4 shows detector saturation temperatures as a function of signal charge (2.0E+07 to 2.0E+09 electrons) and pixel integration times (2 μs and 20 ms).
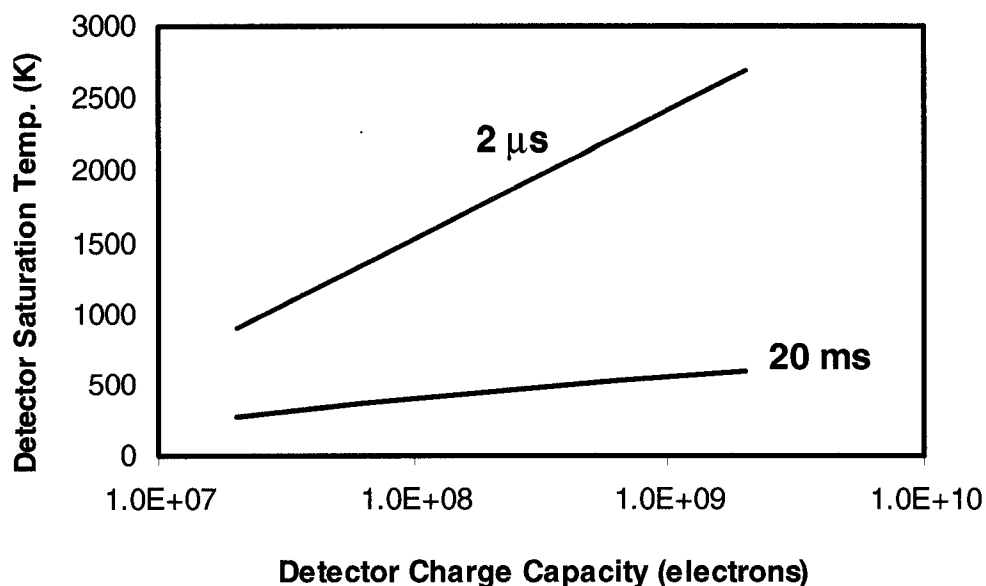
Figure 1-4. Detector saturation temperature (K) vs. detector charge capacity (electrons) for detector integration times of 2 μs and 20 ms. Current state-of-the-art charge capacities of 2.0 E+08 electrons and integration times of 2 μs allow a detector saturation temperature near 1800K. Assumes 3.4 to 3.8 um detector wavelength, 200K detector, 1ha fire area, 300K background.

Saturation temperatures above 1000K are possible for all charge capacity cases

with an integration time of 2 μs. Though this high saturation level is desired for the

resolution of active fires, sensitivity to low temperature fires near 500K will be degraded

(Figure 1-5). This degradation may not be detrimental if SNR remains high, but in all

cases, optimization of saturation temperature, integration time, and charge capacity must

be considered for the design of an operational fire detector.
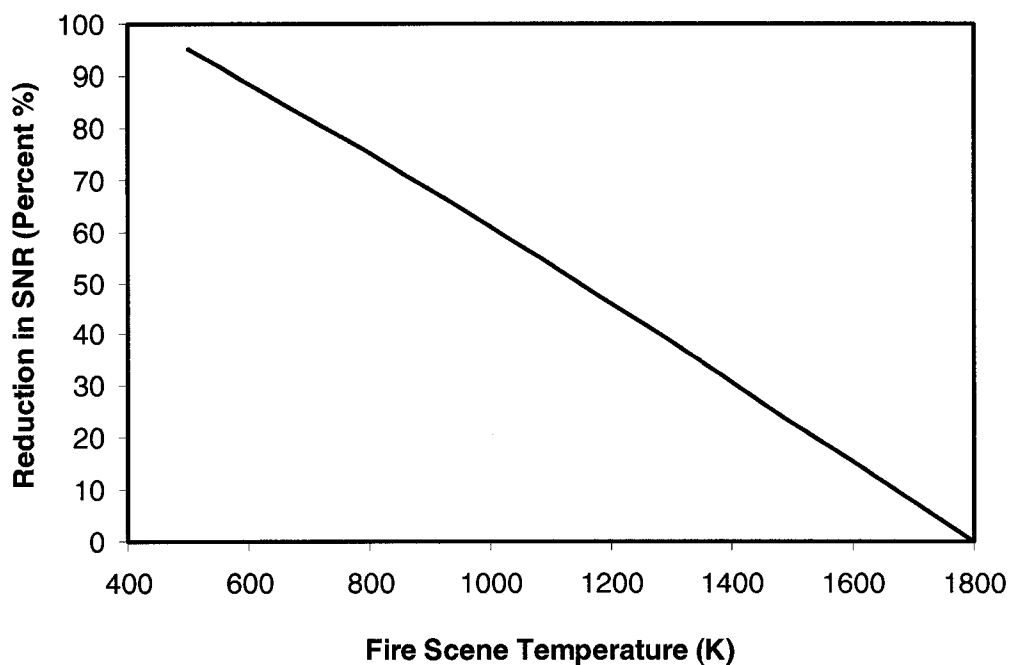
Figure 1-5. Percent reduction in Signal to Noise Ratio (SNR) vs. fire scene temperature
(K). Sensitivity to low temperature fires near 500K is greatly reduced for detector
systems with saturation temperatures near 1800K. Assumes 3.4 to 3.8 um detector
wavelength, 200K detector, 1ha fire area, 300K background, 20μs detector integration
time and 2.0E+08 charge capacity.

Pixel format and detector packaging are also important considerations for a fire detection system in space. Large format arrays will require significant electronics support and additional cooling capabilities. Smaller linear array formats will relieve some of these constraints. Rockwell Scientific (Sarlot et al., 1999) currently produces large format (1024 x 1024) and linear arrays with pixel dimensions of 18.5 μm. Assuming a linear array (1000 x 1) aligned with the North-South direction across the U.S. to cover 2400 km, the detector array length would approach 0.5 meters to accommodate 24 linear detectors. Additional detectors could be added in the East-West direction for redundancy or overlap without increasing the overall dimensions beyond 0.5 meters (Figure 1-6). Practical engineering judgment suggests this is not an unrealistic detector size and future technology advancements will likely improve this constraint.

North

40 Rows of Detectors in
East-West Direction

West

East

24 Detectors in
North-South Direction

South
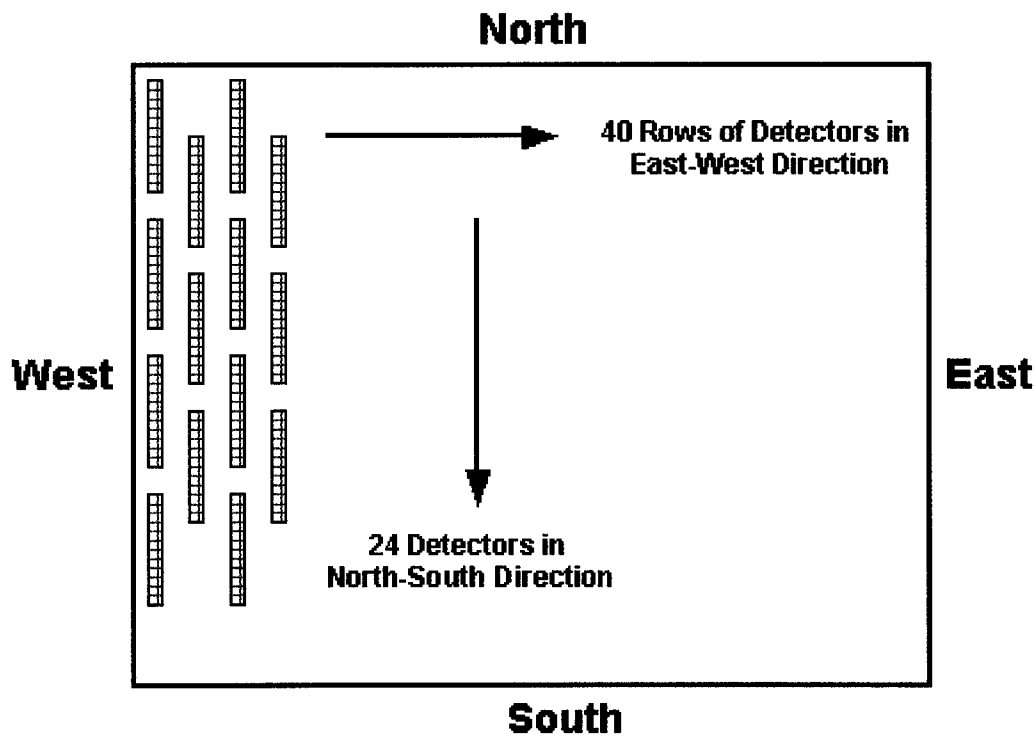
Figure 1-6. Example layout of linear (1000 x 1) detector arrays. This layout could be used to scan the entire U.S. (2400 km by 4000 km) using a nutating approach.

Detector sensitivity is best measured by a parameter called Noise Equivalent Temperature Difference (NETD). For a given wavelength band and scene temperature, the NETD is the smallest resolvable temperature difference that the detector can resolve when SNR = 1.0.

Assume $\Delta T \ll T$ and S is the detector signal, then

$$\frac{S(T+\Delta T)-S(T)}{S(T)} = \Delta T \cdot \beta \tag{1-2}$$

where β is a constant. Assume

$$\text{NETD} = \Delta T = \frac{S(T + \Delta T) - S(T)}{S(T) \cdot \beta} = \frac{\Delta S}{S(T) \cdot \beta} \qquad (1\text{-}3)$$

and $\Delta S = N$ if SNR = 1.0. If $\Delta T = 1K$ then

$$S(T + 1) - S(T) = \beta \cdot S(T) \qquad (1\text{-}4)$$

Substituting into the NETD equation yields:

$$\text{NETD} = \frac{N}{S(T) \cdot \beta} = \frac{N}{S(T+1) - S(T)} = \frac{1}{\dfrac{S(T+1)}{N} - \dfrac{S(T)}{N}} \qquad (1\text{-}5)$$

Using this equation, NETD can be evaluated by calculating SNR at two temperatures separated by 1K, assuming a known and fixed detector noise, N.

The 3.4 to 3.8 μm wavelength band was used to evaluate NETD at a detector temperature of 200K and an integration time of 20 μs (Figure 1-7). The peak detector sensitivity is located near 800K since the chosen wavelength band has a peak radiation emission near that temperature according to the Planck function (Figure 2-1). This clearly shows how detector sensitivity can be optimized for a given scene temperature. In this case, a 650K to 1400K active fire can be detected within 0.1K accuracy. Adjustments in the detector wavelength band will tend to shift this curve such that the best sensitivity always coincides with the peak of the Planck radiance function as defined by Wien's Law (Figure 2-2).
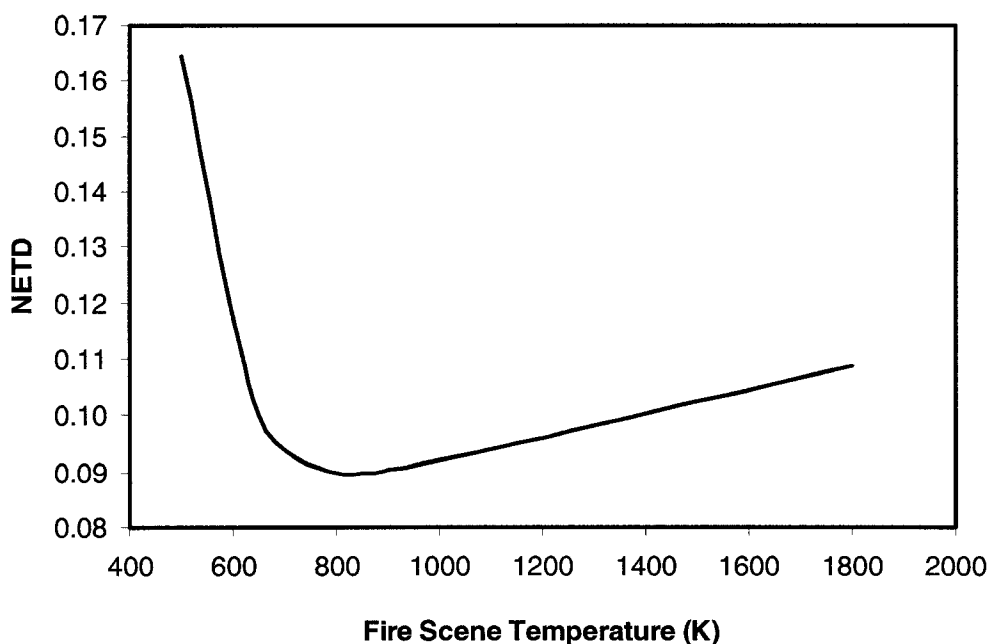
Figure 1-7. Noise Equivalent Temperature Difference (NETD) vs. fire scene temperature (K). Active fires near 1000K can be detected within 0.1K accuracy. Assumes 3.4 to 3.8 um detector wavelength, 200K detector, 1ha fire area, 300K background, 1800K saturation, 20μs detector integration time and 2.0E+08 charge capacity.

Considering the presented parameter studies, a baseline fire detection system is presented. This system appears feasible with state-of-the-art hardware and software, though improvements are certainly expected in the near future. This detector system would have significant impact on our ability to monitor active fires and provide the necessary inputs to the cellular automata model developed in Chapter III of this research. A summary of the baseline fire detector system is shown in Table 1-2.

Parameter	Value
Array Type	HgCdTe
Wavelength	3.4 to 3.8 μm
Array Format	1000 x 1 Linear
Pitch per Pixel	18 μm
Temperature	200K
Scan Type	Nutating 24 x 40
Integration Time	20 μs
Charge Capacity	2.0E+08 electrons
Saturation Limit	1800K
Refresh Rate	40 sec (Entire U.S.)
Resolution	100 sq.meters
Primary Mirror	3.2 m diameter
NETD Sensitivity	0.093K at 1000K

Table 1-2. Baseline detector parameters for a fire detection and monitoring system. The combination of these parameters yields a feasible system with high saturation temperature, fast refresh rates and outstanding temperature sensitivity.

The desire to achieve shortwave infrared data (near 3.6 μm) and longwave infrared data (near 10 μm) simultaneously, is an additional requirement that may be solved by recent multi-color detector advancements (Waterman et al., 2002). Separate detector devices require mechanical and optical constraints that significantly add to instrument complexity. The ability to measure both the active fire signature and the surface background temperature simultaneously is now possible by stacking detector arrays to achieve passive filtering of the scene (Figure 1-8). Along the same optical path one can collect shortwave infrared energy and then transmit the remaining longwave infrared energy to the next detector layer. Alignment and complex electronic configurations are no longer critical engineering issues. This approach could easily allow

on-board processing with a Dozier (1981) algorithm to achieve outstanding sub-pixel

resolution with minimal calibration and post-processing.
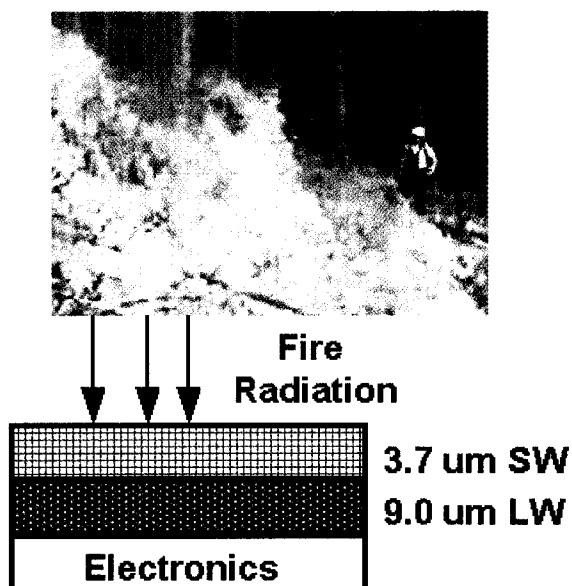
Figure 1-8. A multi-wavelength detector approach allows absorption of shortwave (SW) energy and transmission of longwave (LW) energy to the underlying layer. Mechanical and optical constraints are considerably reduced.

Active Fire Testing

Detector saturation is another important parameter for active fire detection from space. Saturation occurs when the fire scene energy exceeds the measurement range limit of the detector channel and only the maximum possible value is reported for all temperatures above this threshold. The importance of a high temperature threshold detector can be seen in recent testing conducted at the NASA Langley Research Center. A small controlled burn was conducted on January 31, 2001 at the Impact Dynamics Facility in cooperation with the City of Hampton, Virginia Fire Department. Two prototype detectors were tested to determine their performance capabilities for monitoring active fires in the field. Data was obtained over a 30 by 30 foot area of Christmas trees and hay bales using a 320 by 240 pixel array at 1-minute time intervals for the duration of the burn. Visual (Figure 1-9) and infrared images (Figure 1-10) of the fire scene easily verify the burning and non-burning areas according to temperature. An accurate determination of an active fire perimeter requires detectors with high temperature thresholds, such as those used in this field test.
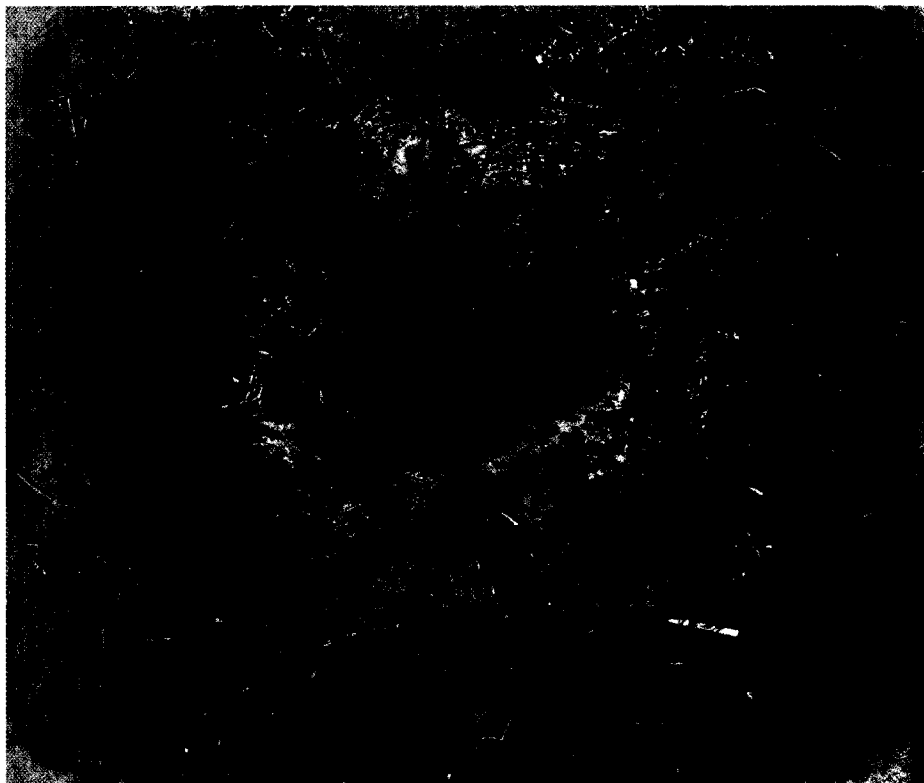
Figure 1-9. Visual image of a controlled burn test 7 minutes after ignition. Active flames can be seen in a circular pattern near the middle. NASA Langley Research Center, Hampton, Virginia, January 31, 2001.

805 °C

20 °C
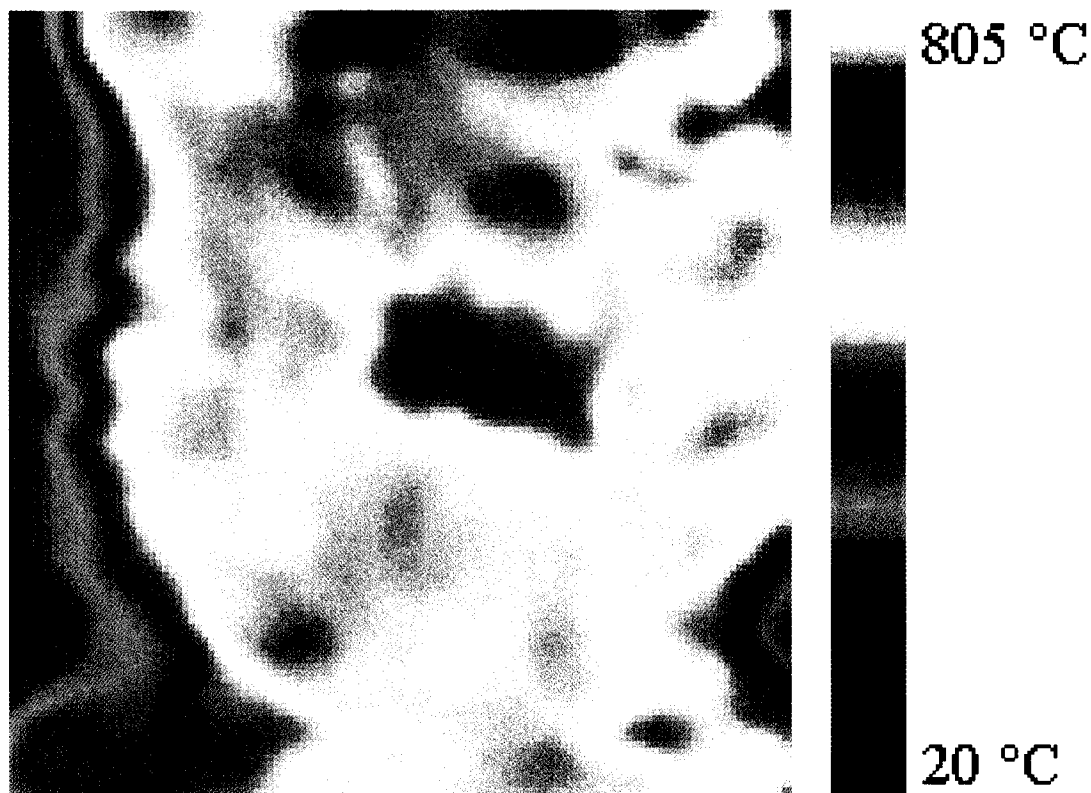
Figure 1-10. Infrared image of a controlled burn test 7 minutes after ignition. Temperatures correspond to the active flames seen in Figure 3. NASA Langley Research Center, Hampton, Virginia, January 31, 2001.

Figure 1-11 shows the range of pixel temperatures measured over the entire burn period. Temperatures range from ground conditions near 300K to flaming conditions over 1000K. A temperature and time history of any fire event could be used to assess the maximum burn temperatures and thus allow correlation with biomass burning emission models. Therefore, high temperature detectors have two important features for fire monitoring. First, the fire perimeter can be accurately identified and tracked with no scene discrepancies due to the ability to measure high temperatures. Second, the temperature and time history of a fire event could be used to assess biomass burning emission rates and help to improve future models.
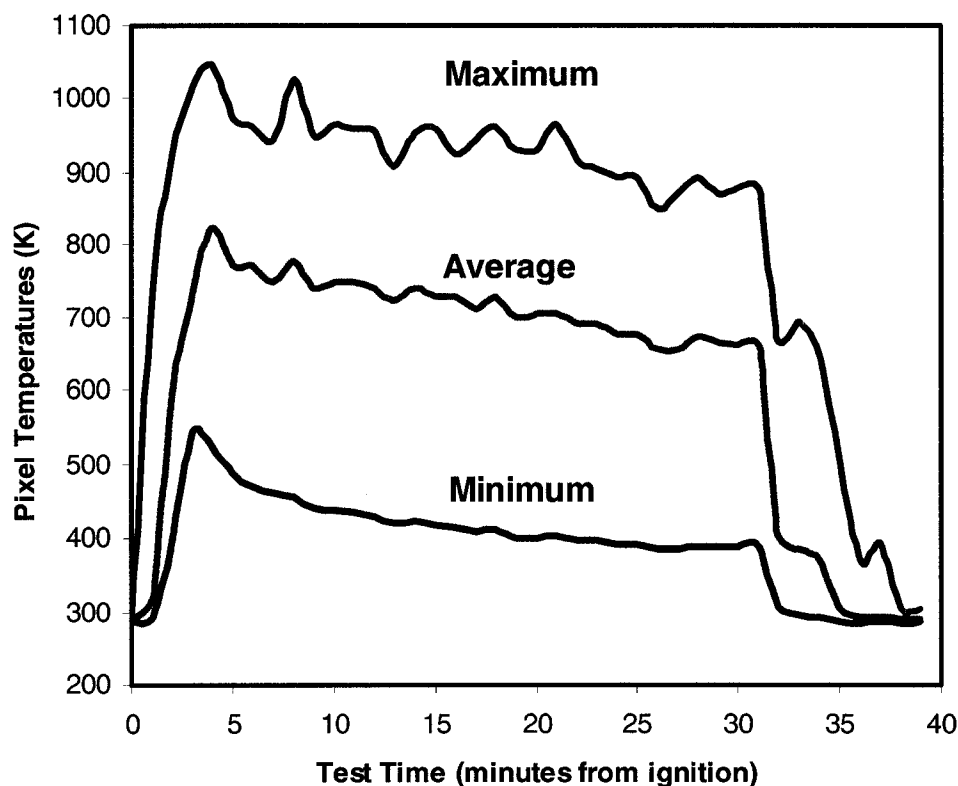
Figure 1-11. Pixel Temperature vs. Time of the controlled burn test. Measured temperatures ranged from 300K (ground) to 1000K (active fire) over the 40-minute burn test. NASA Langley Research Center, Hampton, Virginia, January 31, 2001.

Wildfire burning yields two general types of fire: flaming and smoldering (Lobert and Warnatz, 1993). Flaming fires tend to burn hot (above 900K) with complete combustion allowing the formation of oxidized compounds such as carbon dioxide. Lower temperature (below 900K) smoldering fires produce incomplete combustion and the formation of carbon monoxide (Andreae, 1991). A major challenge facing those who study biomass burning is determining the amount of time spent in flaming versus smoldering conditions (Tsai, 2000). The presented fire detection system would significantly improve our knowledge of these processes.

Resolution Capabilities

Adequate fire detection relies on the ability to resolve both small fire areas, for the assessment of fire intensity and accurate flaming temperatures, and large fire areas for the assessment of fire boundaries and propagation maps. It will be shown that the presented approach is an improvement over existing fire detection instrumentation, such as the Advanced Very High Resolution Radiometer (AVHRR) and the Visible Atmospheric Sounder (VAS). The resolution capabilities are a function of detector saturation temperature, footprint area and the detector noise limit.

Detector saturation is the key parameter in the evaluation of the maximum resolvable fire area. At fire temperatures above the saturation temperature the resolvable area is smaller than the footprint area due to the increased radiance from the fire scene. Figure 1-12 shows the maximum resolvable fire area per pixel as a function of fire temperature for AVHRR, VAS and the baseline detector (assuming 3.7 μm). All cases show reduced resolution as the fire temperature exceeds the detector saturation. In the case of AVHRR, Kennedy et al. (1994) suggested that a 400 m^2 (4% of a pixel footprint) fire at 800K would saturate the 3.7 μm channel. In the case of VAS, Prins and Menzel (1994) suggested that a 5.0E+06 m^2 (2.6% of a pixel footprint) fire at 450K would saturate the 3.9 μm channel. VAS is less susceptible to saturation than AVHRR due to its larger pixel footprint area (190 times greater). The presented detector shows a clear improvement over AVHRR beyond 500K, but does not approach VAS due to the lower

pixel footprint needed to resolve small fires and flaming temperatures. The choice of 1800K as the detector saturation temperature limits maximum resolution at fire temperatures below this temperature, but improves sub-pixel resolution at temperatures above 1000K where intense flames or high wood fuel temperatures may exist (Vines, 1981). The ability to resolve fires as large as $1000m^2$ (10% of a pixel footprint) at extreme temperatures near 1800K is now possible.
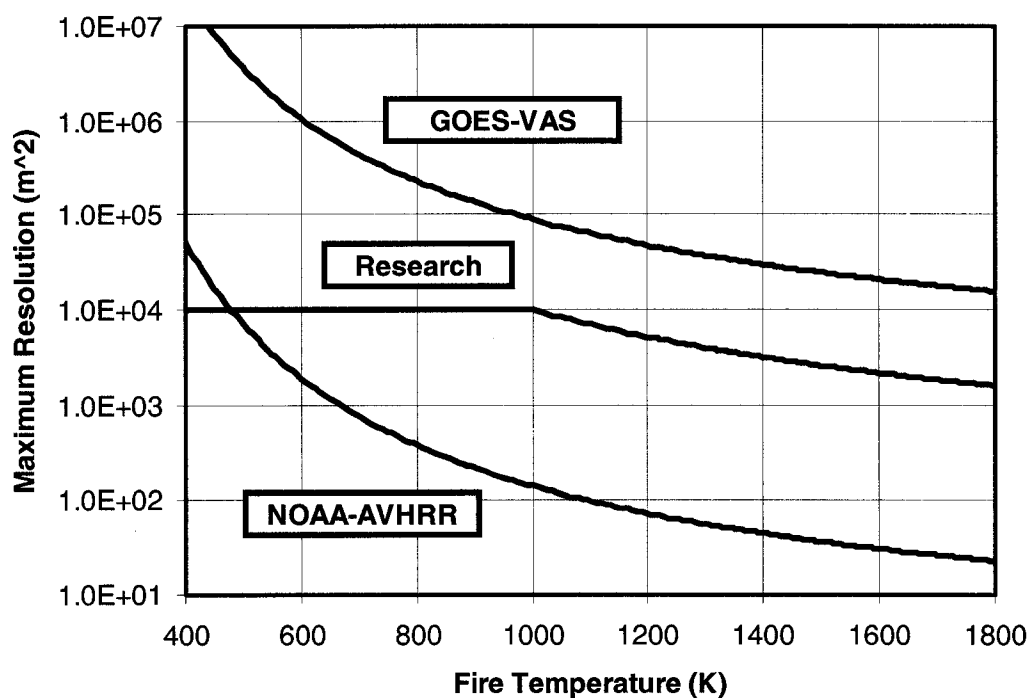
Figure 1-12. Maximum resolvable fire area per pixel vs. fire temperature for existing and presented fire monitoring instrumentation. Resolvable area is limited by saturation and the footprint area of the detector. The presented instrument saturates at 1800K and is limited to one hectare resolution (100 meters by 100 meters square), but shows improvement over NOAA-AVHRR.

The minimum resolvable fire area depends on the sensor noise limitations and footprint area, as the measured radiance must be discernable over the background surface. This is often referred to as the noise equivalent temperature or the equivalent brightness temperature associated with a measurable radiance. AVHRR has a noise limitation of 0.1K and VAS has a noise limitation of 0.2K (Prins and Menzel, 1994). It is expected that the detectors will have noise limitations near 0.1K. Figure 1-13 shows the minimum resolvable fire area per pixel as a function of fire temperature for AVHRR, VAS and the baseline detector (assuming 3.7 μm). Due to its small footprint area (10,000 m^2), the baseline detector will be able to resolve low intensity fires (500K) as small as 0.24 m^2 and high intensity fires (1800K) as small as 49 cm^2. This is a significant improvement over existing instrumentation, including AVHRR (100 times better) and VAS (>10,000 times better). Though detection of small fires is desirable, it is uncertain if areas as small as 49 cm^2 are desired for the extreme cases. Further research and discussions with fire management officials would be necessary to determine the desirable resolution in these extreme minimum and maximum cases.
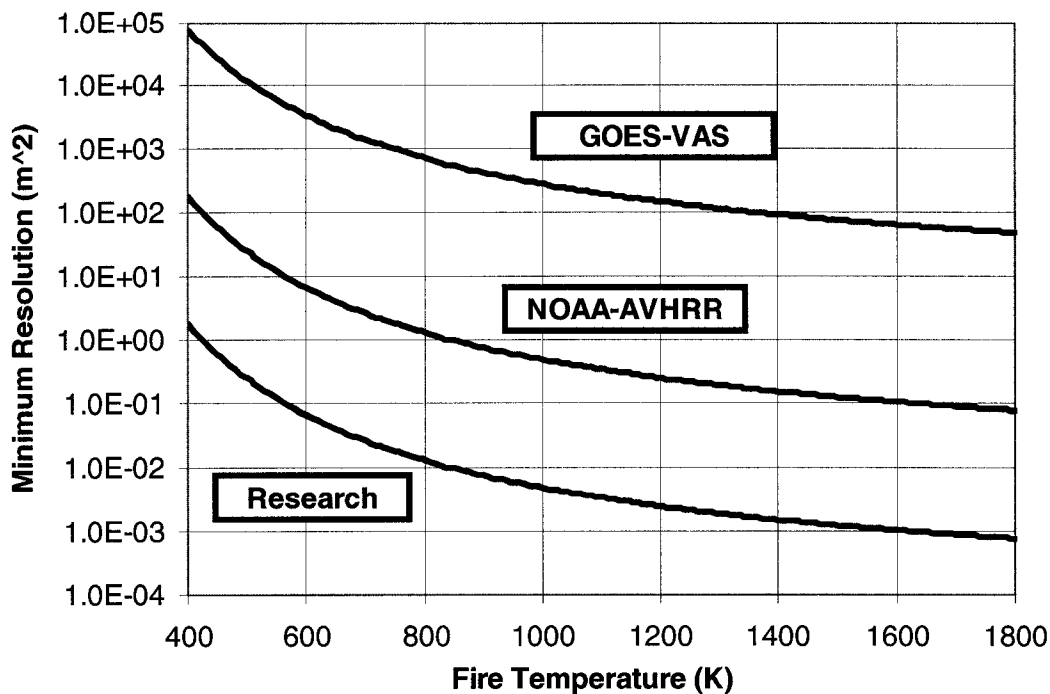
Figure 1-13. Minimum resolvable fire area per pixel vs. fire temperature for existing and presented fire monitoring instrumentation. Resolvable area is limited by noise equivalent radiance and the footprint area of the detector. The instrument will have a noise limitation below 0.1K and a footprint of one hectare (100 meters by 100 meters square). This approach shows significant improvement over both NOAA-AVHRR and GOES-VAS to resolve small fires.

It has been shown that the presented detector system provides improved spatial and temporal sampling over existing instrumentation with the use of dedicated fire channels for efficient and practical fire monitoring. Furthermore, the increased temporal sampling of active fire scene data will provide the necessary inputs to the cellular automata propagation model presented in Chapter III of this research.

CHAPTER II. RADIATION MODELING

Fire detection from space requires an understanding of fundamental radiative energy transfer. This chapter will present the following topics: the radiation principles of fire detection; a method for determining fire scene temperatures; radiation modeling to identify wavelength regions for fire detection; and an analysis of the impact of clouds and smoke on fire detection. This background information and modeling provides the foundation of the planned approach and describes the baseline expected performance of an operational fire detection system.

36

Radiation Principles

The physical principles associated with blackbody radiation are described below with the general equations taken from Wertz and Larson (1999). The total energy radiated from a blackbody source such as a fire on Earth, varies with temperature according to the Stefan-Boltzmann's Law:

$$E = \sigma T^4 \qquad (2\text{-}1)$$

where $E = \text{Energy} (W/m^2), T = \text{Absolute Temperature} (K), \text{and}$

$\sigma = \text{Stefan - Boltzmann Constant} (5.67E\text{-}08\, W/m^2 K^4).$

The spectral distribution of this thermal radiation or blackbody radiation is given by Planck's Law. This is the radiated energy of a source for a specific wavelength.

$$E_\lambda = \frac{2\pi h c^2}{\lambda^5 (e^{\frac{ch}{kT\lambda}} - 1)} \qquad (2\text{-}2)$$

where $E_\lambda = \text{Energy per unit wavelength} (W/m^2 \mu m), \lambda = \text{Wavelength} (\mu m),$

$T = \text{Absolute Temperature} (K), h = \text{Planck's Constant} (6.626E\text{-}34\, Ws^2),$

$c = \text{Speed of Light} (3.0E+08\, m/s), \text{and} \; k = \text{Boltzmann's Constant} (1.38E\text{-}23\, Ws/K).$

Dividing the Planck's Law expression by the solid angle (π steradians) yields the spectral radiance.

$$L_\lambda = \frac{E_\lambda}{\pi}$$

(2-3)

where L_λ is the Spectral Radiance $(W / m^2 \cdot \mu m \cdot sr)$.

In the case of fire monitoring, wavelengths of 3 to 5 μm are suitable for monitoring flaming conditions with blackbody temperatures above 500K and longer wavelengths near 8 to 10 μm are more suitable for measuring Earth background temperatures near 300K (Figure 2-1).
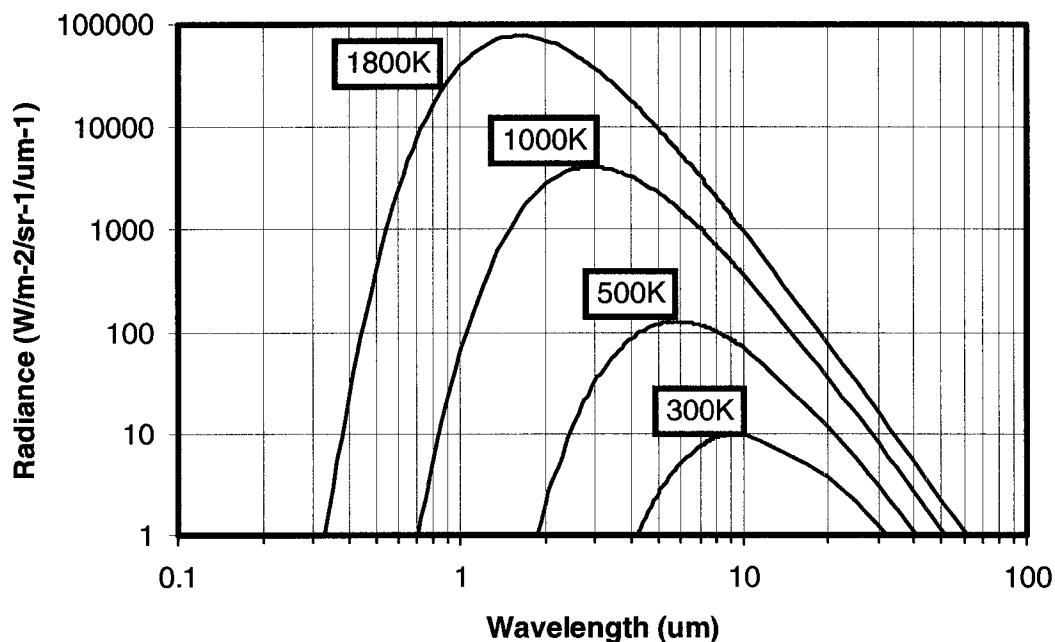
Figure 2-1. Planck's Law radiance as a function of wavelength for various absolute temperatures typical of ground conditions (300K) and active fire temperatures (500 to 1800K).

Analysis of the radiance curves in Figure 2-1 shows that the peak spectral

radiance for a given temperature decreases with wavelength. Differentiating the Planck's

Law function and solving for the wavelength of peak radiance yields Wien's

Displacement Law.

$$\lambda_{max} T = 2898 \tag{2-4}$$

This expression shows that a forest fire with a maximum flame temperature of

1000K would emit at a peak spectral radiance of 2.898 µm (Figure 2-2). A detector with

a spectral response centered at this wavelength would be very sensitive to these fires, as

compared to detectors at other wavelengths. The challenge in identifying any detector

wavelength will be to use this spectral information along with atmospheric attenuation to

achieve the optimum wavelengths for fire detection and monitoring. In the case of the

detector suite presented for this research, the wavelengths will be chosen to identify high-

temperature boundaries of an active fire along with the low-temperature Earth

background.
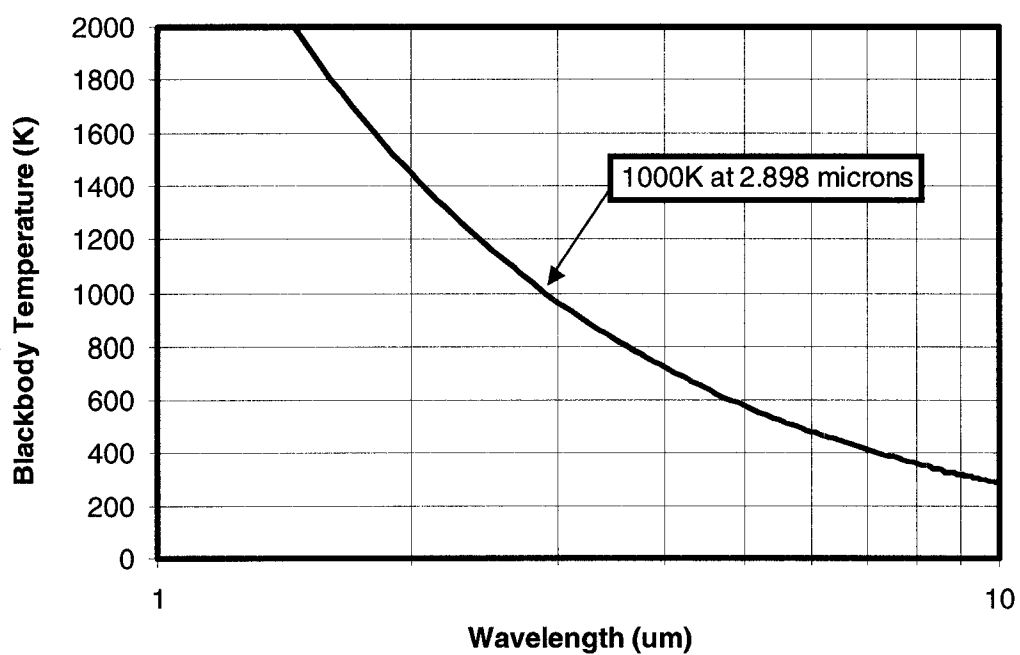
Figure 2-2. Wien's Law distribution as a function of wavelength and temperature. At a given blackbody temperature the peak emitted radiance is found at the corresponding wavelength. For an active fire at 1000K this wavelength is 2.9 microns.

Temperature Inversion

Determination of pixel temperatures in a wildfire scene is critical for evaluating the fire frontal location and the corresponding high intensity regions of the fire. To date, there are three basic approaches for scene temperature measurement from a space instrument. These are (1) single-channel temperature thresholds, (2) multi-channel contextual techniques, and (3) multi-channel sub-pixel resolution techniques. The lattermost approach is known as the Dozier (1981) model and will be the baseline method for this research. A brief explanation of the advantages and disadvantages of each approach is included in this section.

The single-channel temperature threshold approach is the simplest to employ, in that only one detector is required to identify fire scenes. The method is based on emitted scene radiance, such that the emitted radiance L_λ, from the Earth's surface received at the detector is a function of Planck's Law $E(\lambda, T)$ and the spectral response function of the detector $\phi(\lambda)$. Assuming a constant emissivity ε over the small range of wavelengths for a single detector channel, the total emitted radiance of the scene is:

$$L_\lambda = \frac{\dfrac{\varepsilon}{\pi} \displaystyle\int_0^\infty E(\lambda, T)\phi(\lambda)\, d\lambda}{\displaystyle\int_0^\infty \phi(\lambda)\, d\lambda} \qquad (2\text{-}5)$$

In order to determine the scene brightness temperature T_B for a given radiance, the spectral response function of the detector $\phi(\lambda)$ must be known. Assuming this is the case, the scene brightness temperature (T) can found by inverting the emitted radiance function and Planck function:

$$T_B = \frac{ch}{k\lambda \cdot \ln\left(1 + \dfrac{2\,h\,c^2\,\varepsilon}{L_\lambda\,\lambda^5}\right)} \qquad (2\text{-}6)$$

For the case of AVHRR, the 3.7 μm channel has been used for fire discrimination (Pereira and Setzer, 1993; Chuvieco and Martin, 1994) by employing a temperature threshold equivalent to the saturation temperature (322 to 331 K) of the detector (Robinson, 1991; Kidwell, 1991). Unfortunately, this approach has been the subject of many reports scrutinizing and discussing its effectiveness in mixed scenes where saturation is caused by reasons other than active fires (Robinson, 1991; Giglio et al., 1999; Setzer and Verstraete, 1994; Kennedy et al., 1994). In particular, deserts and high albedo targets have been known to cause saturation without the presence of fires. For this reason, the presented detector for near-infrared detection of active fires will utilize a maximum temperature saturation well above the devices on existing platforms. Additional discussions on this topic and detector wavelength will be discussed in the following sections of this chapter.

The multi-channel contextual approach utilizes the discrete responses from detectors with spectral bands located in the mid-infrared (active fires) and the thermal-infrared (background). In this case fire discrimination is determined by employing a

series of specific thresholding criteria that test for fire on a pixel-by-pixel basis. This

general technique considers threshold values (k_1,k_2,k_3) for the near-IR channel

brightness temperature T_A and the mid-IR channel brightness temperature T_B , as well as

a combination of both. This approach has been widely used for fire detection using

AVHRR (Lee and Tag, 1990; Flasse and Ceccato, 1996; Flannigan and Vonder-Haar,

1986).

$$T_A > k_1 \;\; ; T_A - T_B > k_2 \;\; ; T_B > k_3 \qquad (2\text{-}7)$$

The threshold values are determined empirically and typically vary by region.

The main disadvantage of this approach is that it is insensitive to variations in usual land

surface temperature changes during the time period and for the area under study. Prins

and Menzel (1994) used this approach as the basis for their GOES VAS Automated

Biomass Burning Algorithm (ABBA), but later switched to a Dozier (1981) algorithm.

In all of the cases, temperature thresholds are still used to make the final assessment of

fire existence. Although simple to apply, they are still prone to saturation problems in the

mid-IR channels and lack the subpixel discrimination necessary to determine

temperatures.

Dozier Algorithm

The favored approach to fire scene identification is a multi-channel sub-pixel resolution technique developed by Dozier (1981). This theoretical method uses a bispectral approach to derive the sub-resolution brightness temperatures of both the active fire and the background scene in a composite image. The non-linear behavior of Planck's Law produces large increases in radiance for mid-IR wavelengths (near 3.7 μm) even for small increases in temperature. For thermal infrared wavelengths near the peak emissions of the background Earth (near 11.0 μm) the relative change in emission with temperature is an order of magnitude smaller (Figure 2-3). It is this characteristic that forms the basis for the Dozier algorithm and allows the sub-pixel resolution capabilities.
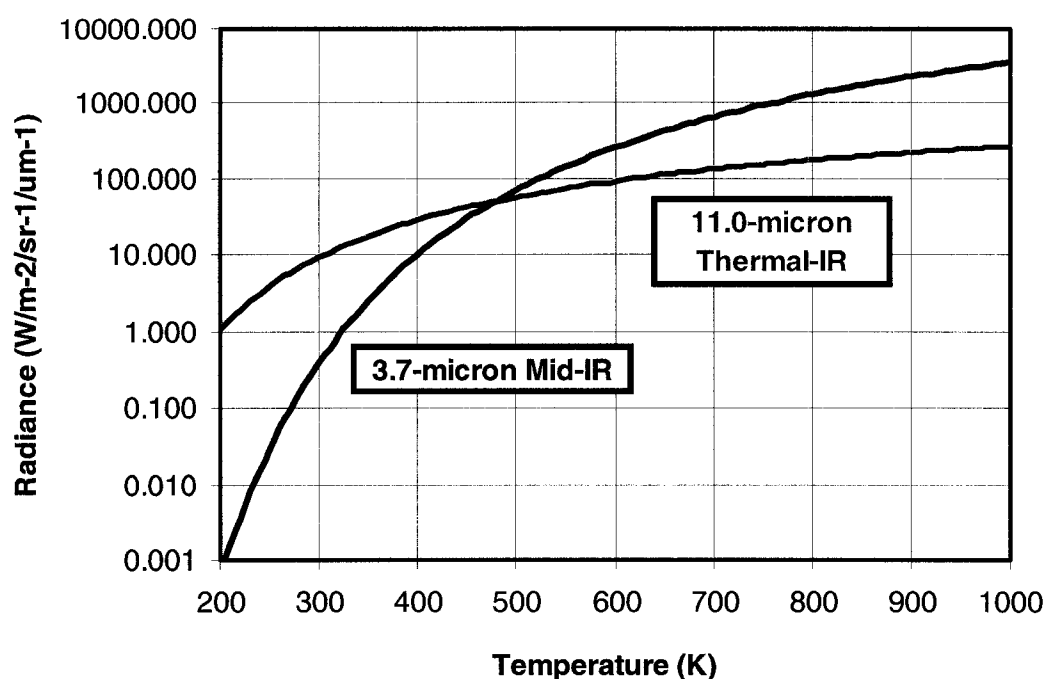
Figure 2-3. Planck Radiance vs. Temperature for Mid-IR (3.7 μm) and Thermal-IR (11.0 μm) spectral bands over a range of temperatures (300K ground to 1000K active fire) representing fire scenes. The differential response is the basis for the Dozier sub-pixel resolving algorithm.

This general approach has been used extensively for the analysis of fire scenes using AVHRR data (Prins and Menzel, 1992; Lee and Tag, 1990; Flannigan and Vonder-Haar, 1986). The capability to resolve small fires within a large footprint is the major benefit of this approach. A sub-pixel fire (one that occupies only a small portion of the pixel footprint) increases the mid-IR radiance significantly more than the thermal-IR radiance. In the case of an active fire at 1000K (typical of the NASA LaRC controlled burn test shown in Figures 1-9 and 1-10) a mid-IR channel (3.7 μm) would receive 375 times more radiation than a thermal-IR channel (11.0 μm) at a background temperature of

300K assuming no atmospheric attenuation. It is this differential response which is the

basis for the Dozier algorithm.

The Dozier algorithm approach is applicable to a geosynchronous satellite system

to yield improved spatial resolutions. The presented set of detectors for this research will

consist of a near-infrared channel λ_A near the peak flame temperature of active fires T_A,

and a mid-infrared window channel λ_B near the peak background ground temperature

T_B. The basic premise of the Dozier algorithm is that a measured scene radiance in a

given channel is an amalgamation of radiances from various scene sources. For example,

if an active fire covers a fraction (f) of the pixel's area, then the fraction ($1 - f$) may be

considered to be at another (non-fire) background temperature (T_B). The fire scene

temperature (T_A) is a function of the inverted radiances (L_A and L_B) and the fractional

radiance of the two sources A and B.

$$L_A T_A = f \cdot T_A(T_{Fire}) + (1 - f) \cdot L_A(T_{Background}) \qquad (2\text{-}8)$$

$$L_B T_B = f \cdot T_B(T_{Fire}) + (1 - f) \cdot L_B(T_{Background}) \qquad (2\text{-}9)$$

These two non-linear equations can be solved numerically (Flannigan and

Vonder-Haar, 1986) since they only contain the unknowns T_A and f. Once solved, the

fraction of the scene containing fire will be known as well as the temperature of the

active fire.

Radiation Modeling

Not all emitted radiation from a fire scene or the Earth's surface will reach a detector in geo-synchronous space orbit. Atmospheric absorption or scattering imposes transmission losses. Understanding these losses is critical to choosing the appropriate wavelength bands for a fire monitoring spacecraft. The transmission must be maximized to design an optimal detector capable of measuring small radiances and resolving small temperature variations. This research will include an examination of gaseous absorption and the effects of smoke and clouds on the radiance measured by the detectors. Identifying the limitations and sensitivity in satellite detection of fires is important to justifying the planned approach. It will be shown that fire detection can be made with the presented detector in the presence of thin clouds and smoke of moderate optical depth.

The initial modeling cases in this chapter did not consider which wavelengths would be best for detecting fires. One must consider atmospheric transmission and the impact of gaseous or molecular continuum absorption as a first step in identifying optical spectral regions and eliminating spectral bands with large attenuation or opaque regions. Additionally cloud and smoke properties must be evaluated to determine their impact on the measured radiance.

All radiation modeling in this research uses the PcModWin program by Ontar Corporation (Anon, 2001) to calculate atmospheric transmission and radiance over specified wavelength regions. PcModWin provides a PC-compatible program to run the

MODTRAN (MODerate resolution TRANsmission) atmospheric code, developed by the

U.S Air Force Research Laboratory. Various versions of the code have been widely used

over the past 25 years, beginning with the original LOWTRAN code. The code

calculates spectral transmittance and radiance for user-defined atmospheric paths at all

frequencies from the microwave through the visible part of the spectrum with a

maximum resolution of 2 wavenumbers (cm^{-1}).

The MODTRAN transmission calculations use three temperature dependent

parameters: absorption coefficient, line density and average line width. Absorption due

to lines (specific wavelengths) is calculated using the Curtis-Godson approximation and

the Voigt line shape. Absorption and scattering due to gas molecules and particulates

(aerosols) are included. Radiation calculations include atmospheric self-emission, direct

solar irradiance and solar scattering. The governing equations for MODTRAN are based

on radiometric principles found in many radiative transfer texts. These equations are far

too extensive to list, and they are beyond the scope of this research. The capability and

flexibility of MODTRAN allows a preliminary assessment of fire scene radiance in a

single computer program.

The choice of a mid-IR wavelength for active fire detection depends on the

expected fire scene temperatures. Approximately 470K-550K is required to sustain

exothermic reactions in cellulostic fuels (Chandler et al., 1983), 570K-650K is required

for flaming combustion (Albini, 1980), 800K is typical for burning grass (Langaas and

Muirhead, 1988), intense flames burn near 1300K (Vines, 1981) and wood fuels have

maximum burning temperatures of 1700K-1800K. As an example, the recent controlled

burn tests of trees and hay at NASA LaRC (Figure 1-11) reached a maximum

temperature of 1047K. Therefore, a range of 500K-1800K is expected for active fires, with the most typical range at 500K-1000K (Robinson, 1991). Wien's law (Figure 2-2) shows that the suitable spectral region for these temperatures falls between 2.9 μm and 5.8 μm. This spectral region was analyzed to determine an optimum location for a future detector. PcModWin was used to calculate atmospheric transmission for this wavelength region (Figure 2-4). The simulation assumed total transmission to the top-of-the-atmosphere (TOA) without clouds, smoke or aerosol attenuation, and a 1976 Standard Atmosphere. The curves clearly show peak transmission in the 3.5 μm to 3.9 μm region, which is consistent with existing fire monitoring instrumentation and is appropriate for the fire detection wavelengths in this research.
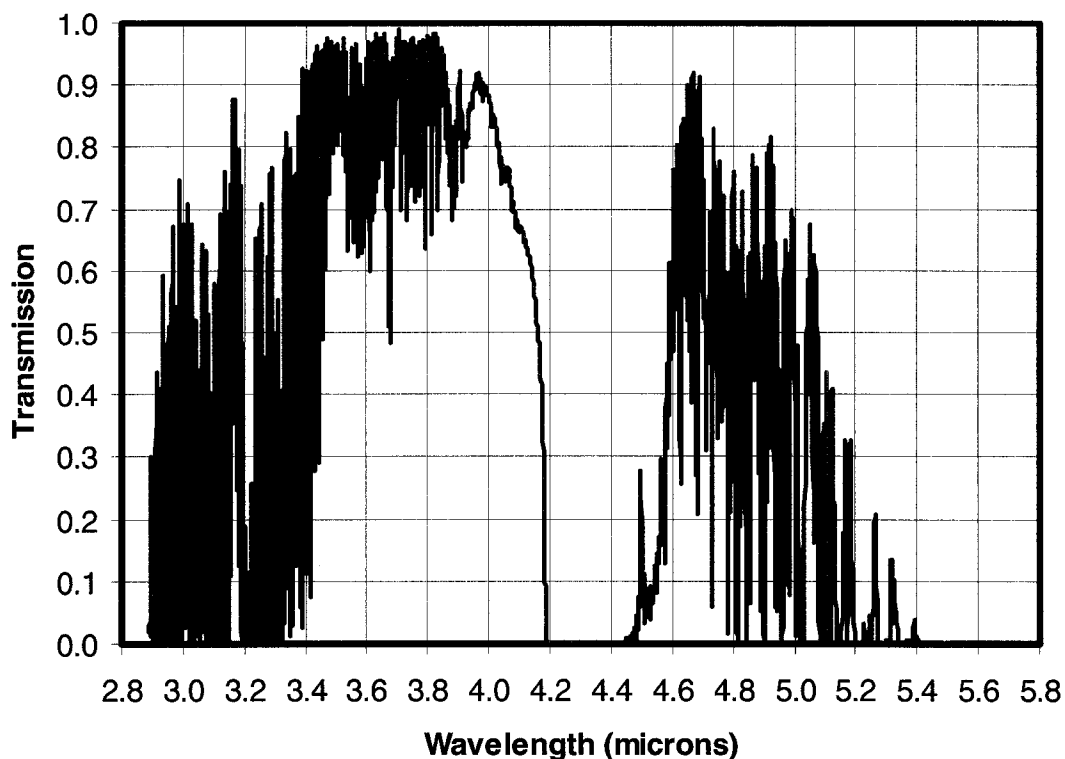
Figure 2-4. Total atmospheric transmission to the top-of-the-atmosphere (TOA) in the mid-IR region (2.9 μm to 5.8 μm), assuming nadir viewing. According to Wien's Law (Figure 2-2), these wavelengths are best suited for monitoring active fires. Transmission is best in the 3.5 μm to 3.9 μm range, which is typical of existing fire detection instrumentation and the approach in this research.

Figure 2-5 shows the transmission losses due to water vapor and carbon dioxide.

The shape of the transmission curve is dominated by water vapor absorption, with the

exception of 4.2 μm to 4.6 μm, which is dominated by carbon dioxide absorption.
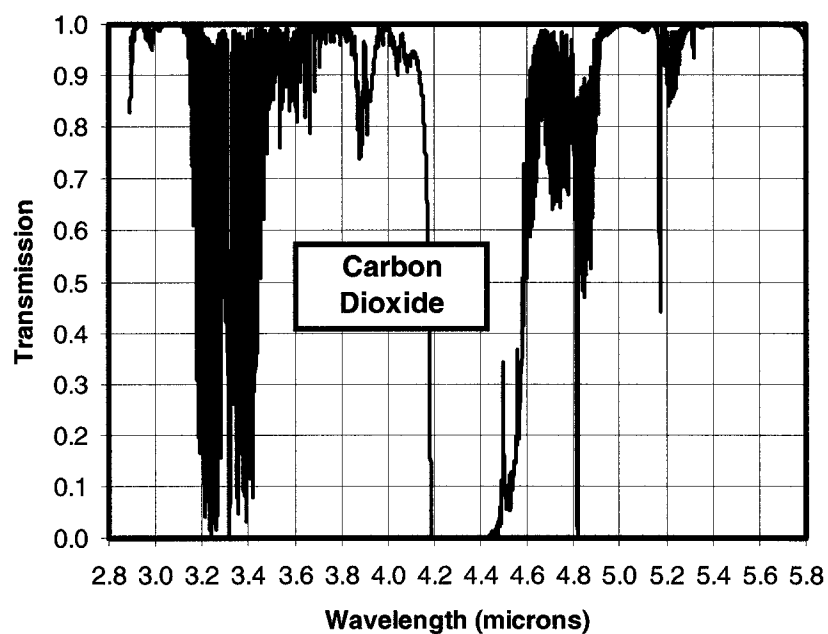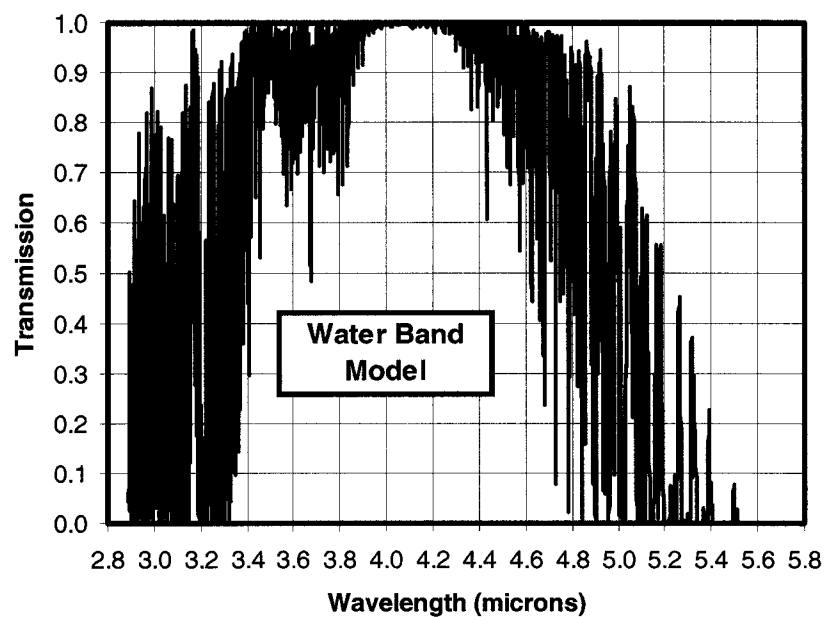
Figure 2-5. Transmission due to water vapor and carbon dioxide to the top-of-the-atmosphere (TOA) in the mid-IR region (2.9 μm to 5.8 μm), assuming nadir viewing. The total opacity (Figure 2-4) near 4.3 μm is primarily due to carbon dioxide and losses across the rest of the spectral region can be attributed primarily to water vapor absorption. Atmospheric absorption is a key element in the selection of fire detection bands to minimize transmission losses and increase detector measured radiance.

To monitor active fires and accurately measure intensity it is imperative to use a detector with shorter wavelengths and higher saturation than is currently utilized in space. Existing systems were not specifically designed for fire monitoring, but in this research, the focus will be to define a system to monitor active fires. According to these preliminary results, a wavelength range of 3.5 μm to 3.9 μm is appropriate for active fire detection.

According to the National Climatic Data Center (NCDC) at the National Oceanic and Atmospheric Administration (NOAA) the long term (1895 to 2000) average annual temperature for the contiguous U.S. is 285K (www.ncdc.noaa.gov). If one considers the summer months of July or August, when fires are typically more severe and numerous, the average surface temperatures will be higher. According to the U.S. Standard Atmosphere (Anon, 1966), the surface temperature in July ranges from 294K (45 degrees North latitude) to 301K (30 degrees North latitude). Wien's Law (Figure 2-2) shows the suitable spectral region for these temperatures falls between 9.6 μm and 9.9 μm. A bias toward higher surface temperatures would require shorter wavelengths below 9.6 μm, but this may not be an efficient wavelength if atmospheric transmission is low. Conversely, fires can occur during the winter months which correspond to cooler surface temperatures and wavelengths above 10 μm. In either case, atmospheric transmission modeling will help to define the appropriate wavelength.

PcModWin was used to calculate atmospheric transmission for a wavelength region of 8.0 μm to 12.0μm , assuming similar boundary conditions as for the mid-IR case. Figure 2-6 shows the total transmission is best from 8.0 μm to 9.3 μm and from 10.0 μm to 12.0 μm . Figure 2-7 shows the transmission losses due to water vapor and

ozone in these same wavelengths. Transmission is dominated by water vapor absorption

with the exception of 9.3 μm to 10.0 μm, which is dominated by ozone absorption.
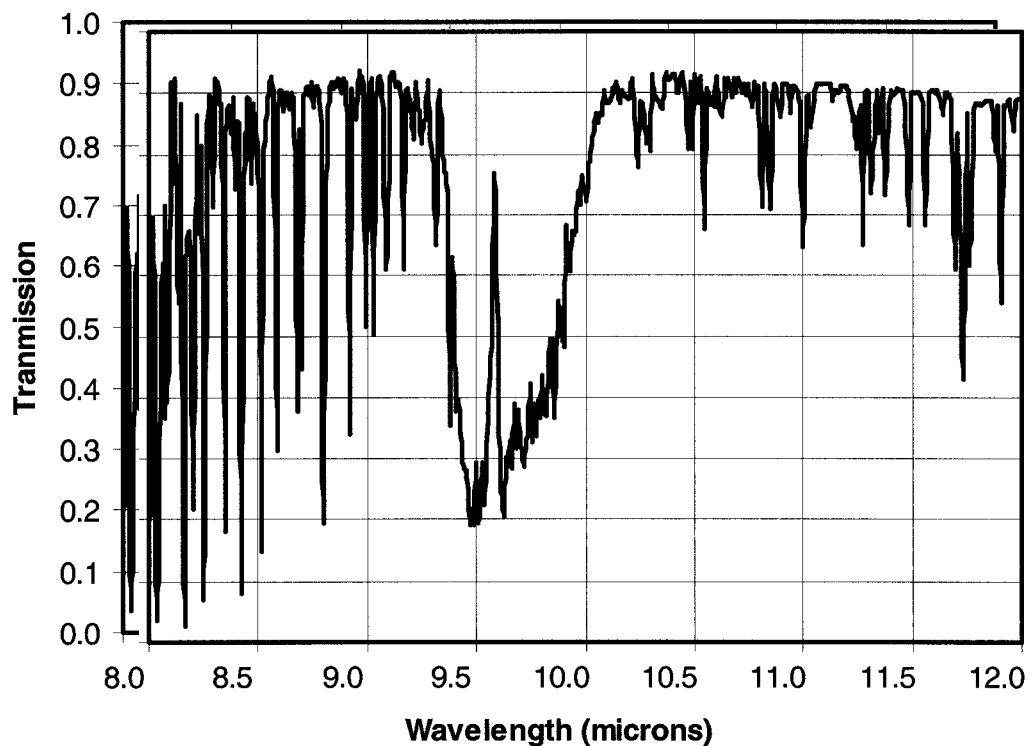
Figure 2-6. Total atmospheric transmission to the top-of-the-atmosphere (TOA) in the thermal-IR region (8.0 μm to 12.0 μm), assuming nadir viewing. According to Wien's Law (Figure 2-2), these wavelengths are best suited for monitoring background surface temperatures. Transmission is best from 8.0 μm to 9.3 μm and from 10.0 μm to 12.0 μm, which is typical of existing fire detection instrumentation.
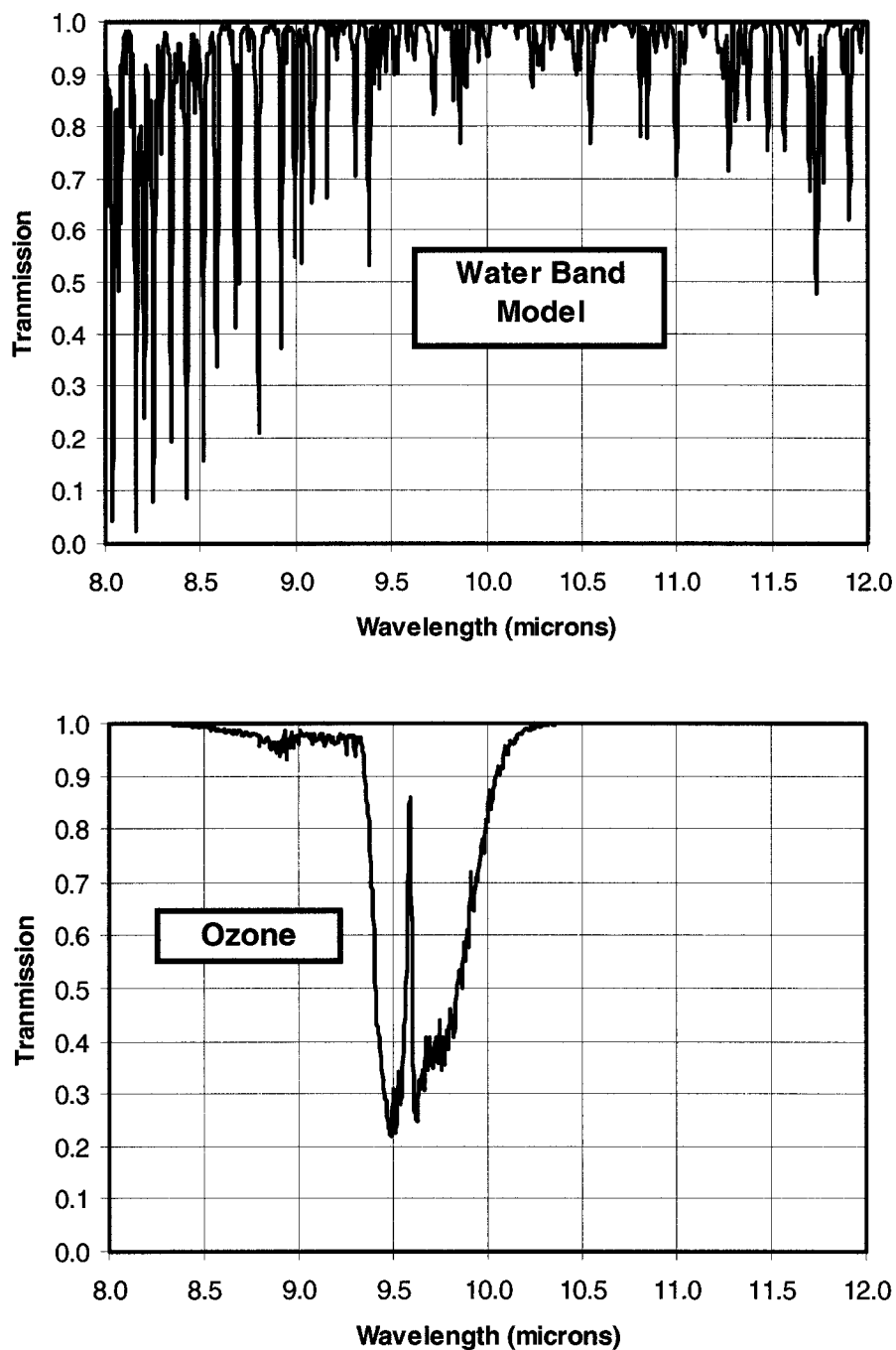
Figure 2-7. Transmission due to water vapor and ozone at the top-of-the-atmosphere (TOA) in the thermal-IR region (8.0 μm to 12.0 μm). The high opacity (Figure 2-6) from 9.3μm to 10.0 μm is primarily due to ozone and losses across the rest of the spectral region can be attributed primarily to the water vapor. Atmospheric absorption is a key element in the selection of fire detection bands to minimize transmission losses and increase detector measured radiance.

The results from these preliminary simulations suggest 3.5 μm to 3.9 μm is the best mid-IR wavelength for active fire detection. This is due to minimal atmospheric transmission losses and a peak emitted radiance at equivalent blackbody temperatures of 743K to 828K, according to Wien's Law. Shorter wavelengths, corresponding to higher temperatures above 1000K, are not feasible due to high opacity from water vapor absorption. The best thermal-IR wavelength for measuring background surface temperature is 10.2 μm to 10.6 μm. Though typical summer surface temperatures (294K to 301K) suggest wavelengths of 9.6 μm to 9.9 μm, this region is dominated by ozone absorption. A more appropriate wavelength is 10.2 μm, which corresponds to the average annual temperature of the contiguous U.S. (285K) and has minimal transmission losses.

Impact of Clouds

The impact of smoke and clouds must be considered in the detector design process and in the operations process. Many existing fire detection algorithms, such as AVHRR and MODIS (Kaufman and Justice, 1998) utilize a process to detect clear-sky scenes without cloud contamination before considering fire detection. This severely limits the data available for monitoring fires from space, because no simple solution exists. It is anticipated that the detector will allow fire detection through thin cirrus clouds and smoke. The atmospheric modeling in this research will aim to define the limitations and capabilities of fire detection under these conditions.

MODTRAN was used to model the effects of three basic cloud types on fire detection: cumulus, stratus, and cirrus. Baseline parameters exist in MODTRAN for each cloud type. The ability to detect a 1000K fire will be measured by calculating the expected SNR for each cloud type as a function of cloud layer thickness. A noise equivalent radiance of 1.3 $W/m^2 \cdot sr \cdot \mu m$ (0.1K resolution at 1000K) was assumed for all cases. As discussed in Chapter I, an SNR above 10 will adequately allow the detection of active fires beyond noise levels. This threshold will be used to determine the potential for detecting active fires whose radiation signal is attenuated by clouds in the atmosphere.

The cumulus cloud cases assumed a cloud base at 0.66 km, a thickness range of 0 to 100 meters, and default cloud extinction coefficient of 92.6 km^{-1} at 0.55 μm. The

extinction is a measure of radiation attenuation due to liquid water droplets and ice

particles along the optical path. The average water droplet size is 10 μm. In the case of

stratus clouds, the cloud base is 0.33 km, the thickness range is 0 to 100 meters and the

cloud extinction coefficient is 56.9 km^{-1}. Figure 2-8 shows SNR for these two cloud

types as a function of cloud thickness. As expected, strong water vapor absorption results

in high attenuation and large optical depth (the product of column density and extinction

coefficient). Due to low SNR at minimal cloud thicknesses, it is doubtful one can detect

active fires through nominal cloud layers of these types. Only in the thinnest cloud layers

may it be possible to resolve an active fire.
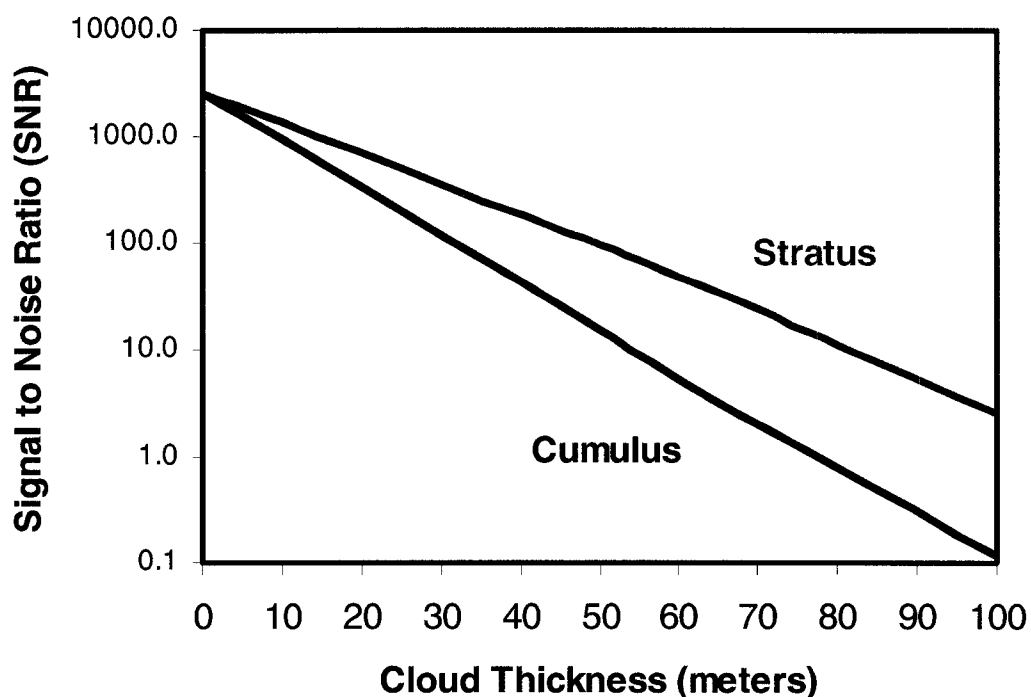
Figure 2-8. Signal-to-Noise Ratio (SNR) as a function of cloud thickness for common
cumulus and stratus clouds. SNR degrades to 10 for cumulus clouds greater than 50
meters thick and stratus clouds greater than 80 meters thick. These low thresholds
suggest fire detection through cumulus an stratus clouds is unlikely.

The cirrus cloud cases are considered separately, since their optical depth is much

lower and cloud attenuation allows fire detection even at large thicknesses. A cloud base

of 10 km, typical of a mid-latitude summer atmosphere, was assumed. Tops of cirrus

clouds are often closely associated with the tropopause boundary, and have been

observed as high as 15 km. A cloud thickness range of 0 km to 5 km was assumed. High

cirrus clouds are known to have a median thickness of 1.0 km (Figure 2-9) and show little

or no variation with season. They also tend to be more persistent than cumulus or stratus

clouds due to the increased levels of ice and lower evaporation rates. Additionally, the

cloud extinction coefficient is a linear function of cloud thickness (0.14 per km) and is

independent of wavelength for the mid-infrared region (Kneizys, 1983).
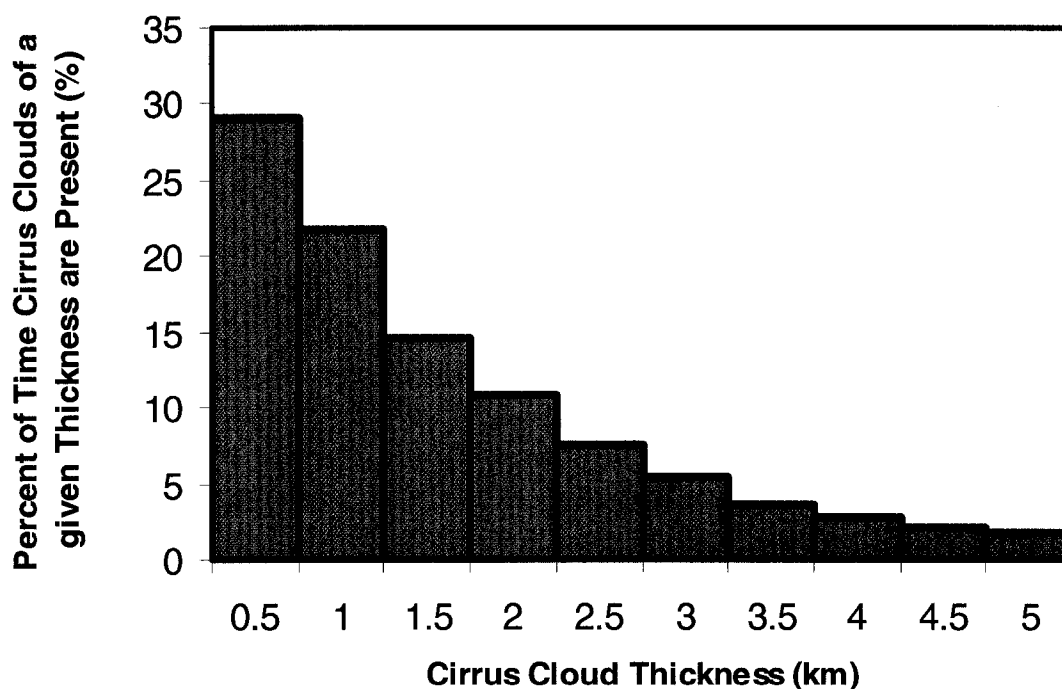
Figure 2-9. Histogram of cirrus cloud thickness. The median cloud thickness is 1.0 km. Since cirrus clouds less than 2 km thick account for 75% of the cirrus cloud cases, the capability to resolve active fires is important to a fire detection system utility.

The previously mentioned baseline assumptions were used to calculate SNR over

the range of cloud thicknesses. Figure 2-10 shows it is possible to resolve fires with

adequate SNR at even the largest thicknesses (5 km) and certainly at the median cirrus

layer thickness of 1.0 km.
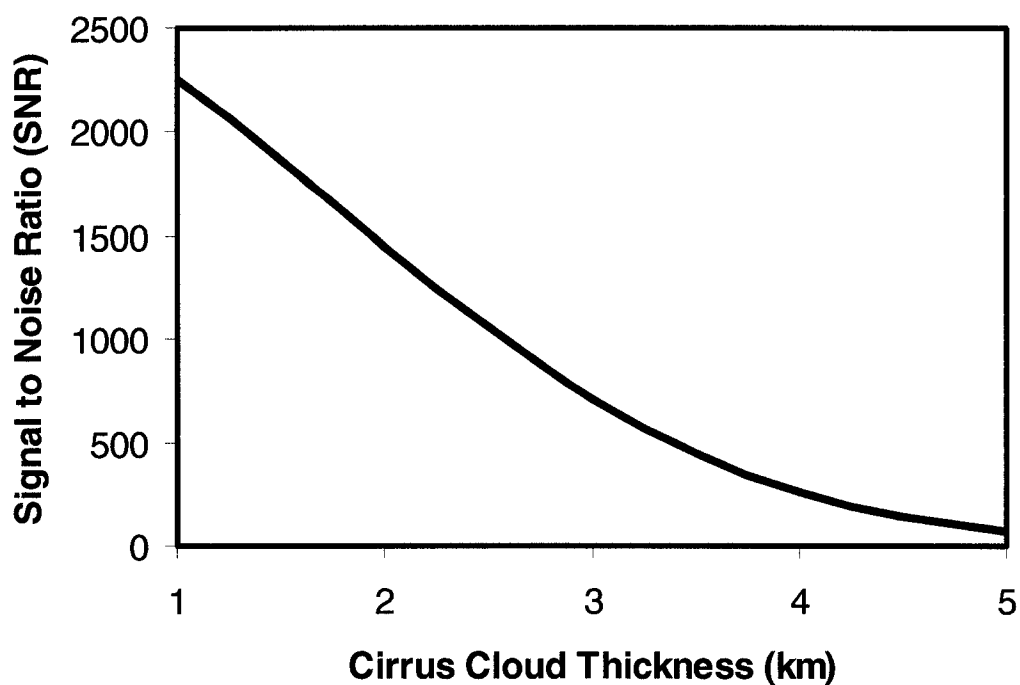
Figure 2-10. Signal-to-Noise Ratio (SNR) as a function of cirrus cloud thickness.
Mid-IR fire detection is possible through a median cirrus clouds of 1.0 km thickness and
even the thickest cirrus clouds near 5 km thickness.

Impact of Smoke and Urban Aerosols

A useful feature of PcModWin is its inclusion of aerosol transmission and emission effects. Though there are several included aerosol models (rural, navy maritime, urban, tropospheric, fog, desert) none of these directly model smoke aerosols. Radiance transmission through smoke is effectively modeled with a user-defined code using the following approach. First, a smoke character (soot or organic), particle size distribution and concentration is chosen. These parameters are based on current smoke research literature. Second, the smoke parameters are used in a Mie calculation code to obtain extinction, absorption and scattering coefficients over specific wavelengths for fire detection. Finally, the aerosol coefficients are placed in PcModWin with a user-defined aerosol input code to obtain the measured radiance through smoke. It is expected that variations in aerosol parameters will allow definition of specific fire detection limitations important to the presented approach. The ability to detect fires through smoke will greatly enhance the capabilities of a future mission.

While extensive measurements of aerosol optical properties are required at various locations and stages of fire growth to fully assess radiation transfer issues, a preliminary assessment can be gained by measuring the sensitivity of radiation transmission and fire detection to variations in smoke aerosol type and size distribution. Smoke aerosol type is largely dependent on fire stage and flame temperature. Flaming combustion yields increased levels of carbonaceous soot whereas smoldering combustion

yields high levels of organic particles. Black carbon mass concentrations vary widely

among smoke aerosol references (Table 2-1).

Reference	Carbon Mass %	Location
Martins et al., 1996	1.5 to 22.5	Washington, U.S.
LeCanut et al., 1996	15	South Africa
Hobbs et al., 1996	5 to 8	Washington, U.S.
Mazurek et al., 1991	1 to 10	Ontario, Canada
Ross and Hobbs, 1998	5 to 11	Brazil
Kaufman et al., 1992	5 to 10	Amazonas
Pereira et al., 1996	5	Brazil
Maximum Range	1 to 22.5	

Table 2-1. Black carbon mass concentrations in smoke over fires. A wide range of carbon concentrations have been measured with a maximum range of 1% (far from the fire) to 22.5% (close to the active flame front). Radiation absorption and scattering depend strongly on carbon content.

Volume and mass distribution also depend on the fire stage. Flaming combustion

yields increased concentrations of carbon soot with smaller mean mass particle sizes near

0.1 μm diameter. Most particles encountered in field experiments (Ross et al., 1998;

Martins et al., 1996) appeared nearly spherical, which is the assumption used in this

research. As fires progress toward the smoldering phase, smoke aerosols grow in size

due to inefficient burning processes and increased coagulation. Measurements by

Martins et al. (1996) show that the diameter of smoke particles increased at an average

rate of 0.11 μm per hour as they were transported downwind of the active fire front.

Smoke aerosol particles have approximately the same size distribution as sulfate aerosols

(Penner et al., 1992) with a median mass diameter of approximately 0.3 μm.

This research will focus on active fire detection in the region nearest the fire front.

For this reason, two particle size distributions were chosen for flaming conditions and

smoldering conditions within 2 hours of fire ignition. This variation will certainly bias

the results towards smaller particles, but will benefit a sensitivity study of fire detection

near active fire fronts. A log-normal distribution is defined for each of the modeled

conditions according to Martins et al. (1996).

$$N(R) = \frac{1}{R\sqrt{2\pi R_S}} \exp\left[-\frac{(\ln(R) - \ln(R_M))^2}{2R_S^2} \right] \qquad (2\text{-}10)$$

Flaming conditions had a mean particle radius (R_M) of 0.069 μm and a standard

deviation (R_S) of 0.50 μm. Smoldering conditions had a mean particle radius of

0.201 μm and a standard deviation of 0.46 μm.
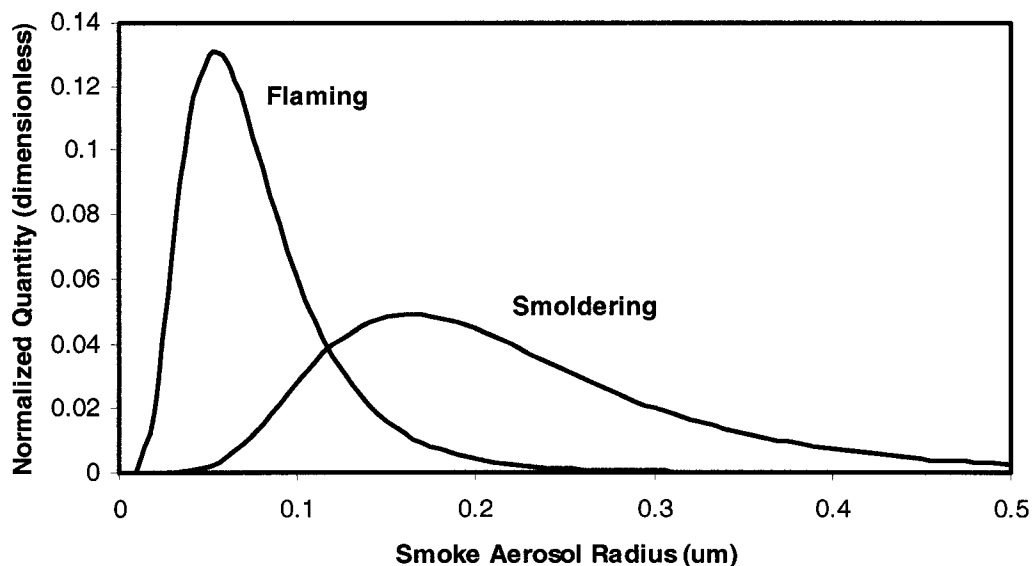
Figure 2-11. Normalized smoke aerosol size distributions for flaming and smoldering conditions according to Martins et al. (1998). A higher concentration of small particles exists near flaming areas and a broader distribution of larger particles exists far from the flame front in smoldering areas. Particle size affects radiation absorption and scattering and the ability to view fires through smoke.

To determine the mass of aerosol material in the atmosphere, an aerosol concentration or average mass density must also be specified. For this study, a value of 1.5 g/cm^3 will be considered. This value was based on a review of several smoke property references (Table 2-2) and represents a mixture of carbon and organic aerosols in typical smoke.

Reference	Aerosol Density (g/cm^3)
Ross and Hobbs, 1998	Carbon 1.8, Organic 1.2
Hobbs et al., 1996	Average 1.5
Martins et al., 1996	Average 1.5
LeCanut et al., 1996	Average 1.3

Table 2-2. Aerosol density variations in smoke over active fires. A wide range of aerosol densities have been measured with an average value of 1.5 g/cm^3. Aerosol density affects radiation attenuation due to absorption and scattering.

Richard E. Davis of the NASA Langley Research Center used the AGAUS82 Mie scattering module of the U.S. Army's EOSAEL radiative transfer suite (Anon, 2001) to perform the Mie calculations over a spectral region of 3.0 mm to 4.0 mm. The standard Mie technique (see for example: Van de Hulst, 1981; or Born and Wolf, 1975) for calculating radiative properties of aerosols provided the single scattering albedo (ratio of scattering extinction to total extinction), and the extinction, absorption and scattering coefficients. These parameters were provided to the author of this research and subsequently used in MODTRAN to develop a user-defined aerosol model. Once the aerosol model was defined for a layer near the surface, the thickness and surface meteorological range of that layer were varied to simulate the impact on attenuation of the fire signal.

The standard Mie scattering technique used in AGAUS82 considers independent homogeneous spherical particles for the calculation of scalar single-scattering properties (Miller, 1983). This technique is based on electromagnetic theory that describes the interaction of a spherical particle and a plane wave. The formal solution of the

Helmholtz equation with the appropriate boundary conditions is the basis for Mie theory

(Van de Hulst, 1981).

$$\Delta^2 \Psi + k^2 m^2 \Psi = 0 \qquad\qquad (2\text{-}11)$$

In this equation k is the wavenumber in a vacuum and m is the index of refraction of the

propagating medium.

$$k = \frac{2\pi}{\lambda_{vacuum}} \text{ and } m = m_{real} + i\, m_{imaginary} \qquad\qquad (2\text{-}12)$$

In most cases, k is replaced with the non-dimensional Mie size parameter.

$$x = k\, r \text{ where } r = \text{particle radius} \qquad\qquad (2\text{-}13)$$

The simple solution to the Helmholtz equation yields:

$$\Psi = e^{ikmz + ikct} \qquad\qquad (2\text{-}14)$$

where c is the speed of sound in a vacuum. In the case of standard atmospheric

extinction, the refraction index m has a negative imaginary part and therefore, the wave

is damped. For the specific Mie case, the equation is transformed to spherical

coordinates and the separable solution becomes:

$$\Psi_{ln} = \begin{Bmatrix} \cos l\theta \\ \sin l\theta \end{Bmatrix} P_n^l(\cos\theta) z_n(mkr) \qquad (2\text{-}15)$$

The first term is either a sin or cosine function, where l and n are integers and $n \geq l \geq 0$. The second factor is an associated Legendre function ($l \neq 0$) and the third factor is a spherical Bessel function.

$$P_n^l(x) = \sqrt{1-x^2} \ \frac{d^l}{dx^l}(P_n(x)) \qquad (2\text{-}16)$$

$$z_n(x) = \sqrt{\frac{\pi}{2x}} \ Z_{n+\frac{1}{2}}(x) \qquad (2\text{-}17)$$

Assuming that the outside medium is a vacuum ($m = 1$), the particle has an arbitrary index of refraction, and the incident radiation is linearly polarized, the scalar solutions of the tangential electromagnetic waves can be written (Van de Hulst, 1981) as:

$$u = -\frac{i}{kr} e^{-ikr+ikct} \cos\phi \sum_{n=1}^{\infty} a_n \frac{2n+1}{n(n+1)} P_n^l(\cos\theta) \qquad (2\text{-}18)$$

$$v = -\frac{i}{kr} e^{-ikr+ikct} \sin\phi \sum_{n=1}^{\infty} b_n \frac{2n+1}{n(n+1)} P_n^l(\cos\theta) \qquad (2\text{-}19)$$

These scalar solutions to the wave equation are related to the electric field strength (E) and the magnetic field strength (H) by the vector fields M_ψ and N_ψ such that:

$$mk\, M_\psi = curl\, N_\psi \tag{2-20}$$

$$E = M_v + i\, N_u \tag{2-21}$$

$$H = m(-M_u + i\, N_v) \tag{2-22}$$

The preceding equations are more general, whereas typical Mie theory is usually characterized by quantities called efficiency factors (Q). These quantities are expressed as Q_e, Q_a, and Q_s, representing extinction, absorption and scattering, respectively. When multiplied by the geometric cross-sectional area of the particle, the efficiency factors give cross-sections (C).

$$C_e = \pi r^2 Q_e = \pi r^2 \left[\frac{2}{x^2} \sum_{n=1}^{\infty} (2n+1)\mathrm{Re}(a_n + b_n) \right] \tag{2-23}$$

$$C_s = \pi r^2 Q_s = \pi r^2 \left[\frac{2}{x^2} \sum_{n=1}^{\infty} (2n+1)\left(|a_n|^2 + |b_n|^2 \right) \right] \tag{2-24}$$

The relationship between all factors considers that the total extinction is a combination of absorption and scattering processes.

$$C_e = C_a + C_s \tag{2-25}$$

The efficiency factors and cross-sections are functions of the complex index of refraction

(m), the radius of the spherical particle (r), and the wavelength of the incident radiation.

The angular dependence of the scattered radiation is found in the Legendre polynomial

phase function (P). This phase function is also a function of radius, wavelength and the

index of refraction.

The extinction efficiency factor (Q_e)and cross-section (C_e) are directly related to

the total attenuation of radiant energy as it passes through the atmosphere and interacts

with a spherical particle. MODTRAN assumes absorption by gaseous particles and

single scattering of energy account for all of the energy loss along a path. The total

transmission (T) along a path length (x) through the atmosphere is expressed as:

$$T = e^{-Q_e x}$$
(2-26)

Calculated efficiency factors are input as a function of wavelength within MODTRAN.

The code assumes the parameters are normalized so that the extinction factor is 1.0 at

0.55 μm. As an example, thick smoke would have a high extinction efficiency factor and

therefore result in low total transmission. This low transmission results in low signal

strength for fire detection.

The general Mie equations provide the basis for the AGUAS82 Mie scattering

calculations. Additional depth on this topic can be found in Mie theory texts (Van de

Hulst, 1981; Born and Wolf, 1975). More specific descriptions of the Mie theory used in

AGAUS82 are found in Miller (1983).

The radiative properties of smoke aerosols depend on the complex refraction index, which is one of the parameters used as input to Mie calculations (Toon and Ackerman, 1981). The complex index of refraction can be linearly weighted for varying carbon mass concentrations to reflect known differences in aerosol types (black carbon and organic). At mid-IR wavelengths near 3.7 μm, the refraction index of carbon soot is $1.900 - 0.570\,i$ and the refraction index of organic aerosols is $1.500 - 0.000\,i$ (Fenn et al., 1985). Assuming a carbon mass range of 1% to 22.5%, the weighted refraction index varies from $1.504 - 0.0057\,i$ to $1.590 - 0.128\,i$, respectively. This parameter variation will be used for Mie calculations to represent smoldering and flaming extremes. Variations in refractive index, size distribution and density were used as inputs for Mie calculations. The following parametric cases were considered (Table 2-3).

Parameter	Case 1	Case 2
Fire Type	Flaming	Smoldering
Real Refraction Index	1.590	1.504
Imaginary Refraction Index	-0.128	-0.0057
Density (g/cm3)	1.5	1.5
Mean Particle Radius (RM)	0.069	0.201
Particle Standard Deviation (RS)	0.50	0.46

Table 2-3. Mie calculation input parameters. Variations in refractive index, density and size distribution will affect absorption and scattering properties of smoke aerosols and impact the visibility of fire through smoke.

Signal-to-Noise Ratio (SNR) was calculated for the two cases in table 2-3 over a smoke vertical thickness range of 0 meters to 800 meters and a surface meteorological range of 10 meters to 1000 meters. This vertical thickness range adequately represents typical forest fire scenes. Studies of forest fires in the Pacific Northwest (Hobbs et al., 1996) indicated smoke plume thicknesses as large as 800 meters, with average plume thicknesses near 400 meters. The surface meteorological range (M_R) is defined in MODTRAN according to

$$M_R = \frac{3.912}{\beta} \qquad (2\text{-}27)$$

where β is the extinction coefficient (km^{-1}) evaluated at 0.55 μm wavelength and M_R is measured in kilometers. M_R is approximately 30% greater than the observer visibility range. A surface meteorological range near 1000 meters is the typical threshold for dangerous aerosol levels in the atmosphere and a range near 10 meters represents extremely thick smoke near an active fire front.

Figure 2-12 shows SNR as a function of M_R for a thin vertical smoke layer (100 meters) and a thick vertical smoke layer (800 meters). As previously discussed, an SNR above 10 should allow adequate signal resolution and successful fire detection. Variations in aerosol physical parameters (flaming or smoldering) had minor impacts on SNR. At detector wavelengths near 3.7 μm there is only a small dependence on aerosol parameters as defined in Table 2-3. Smaller smoke aerosols, typical of flaming conditions (dotted line) had lower radiation attenuation and therefore higher SNR, as

compared to the smoldering (solid line) case. SNR is more dependent on vertical layer

thickness than M_R. Thin vertical layers near 100 meters height will allow fire detection

with a M_R less than 10 meters. Thicker vertical layers near 800 meters height allow fire

detection at a M_R of 20 meters.
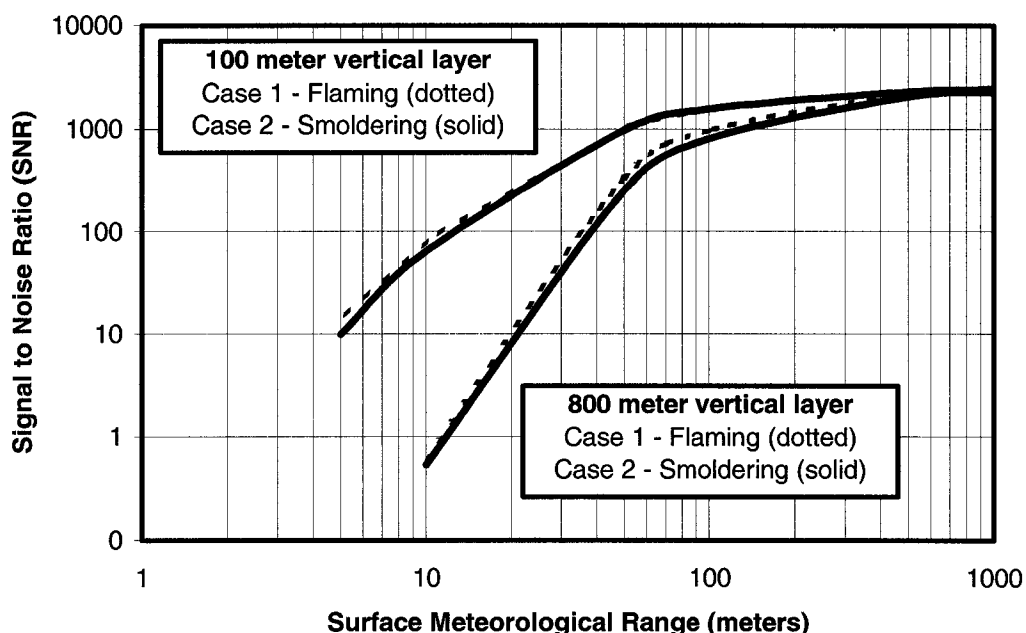
Figure 2-12. Signal-to-Noise Ratio (SNR) as a function of vertical smoke plume
thickness in meters and Surface Meteorological Range (M_R) in meters. SNR is excellent
for M_R values above 100 meters. A mild degradation in SNR occurs for M_R values
below 100 meters, but these visibilities are typical of extreme dense smoke conditions.
The ability to detect active fire fronts through smoke is excellent.

These extreme values of surface meteorological range, or smoke visibility, are not

typical of common fires. Aerosol warning systems often use a hazardous level that

coincides with a M_R of 1000 meters. As an example, the intense smoke from the 1997

fires in Kalimantan and Sumatra, Indonesia (Levine, 1999) yielded visibilities as low as

100 meters. Considering visibilities in this range, the ability to detect an active fire front

through even the thickest smoke is excellent. The smoke cases presented in this research bound the extreme conditions of any fire and support the finding that smoke is generally transparent at 3.7 µm. These results are very promising for the presented detector system.

As a comparison with smoke, the MODTRAN urban aerosol model was used to calculate SNR for a variety of visibility levels (Figure 2-13). The urban aerosol model assumes a boundary layer (0 km to 2 km altitude) of aerosols with a variable surface meteorological range, or visibility. Urban aerosols contain large concentrations of sulfate particles which are similar in size to smoke aerosols (Penner et al., 1992). Penner suggests that effectively all of the optical effects are associated with particles having a mass-averaged radius of 0.3 µm. Therefore, it is expected that radiation attenuation due to absorption and scattering for urban aerosols will be similar for those of smoke, but only slightly higher due to larger particle sizes.
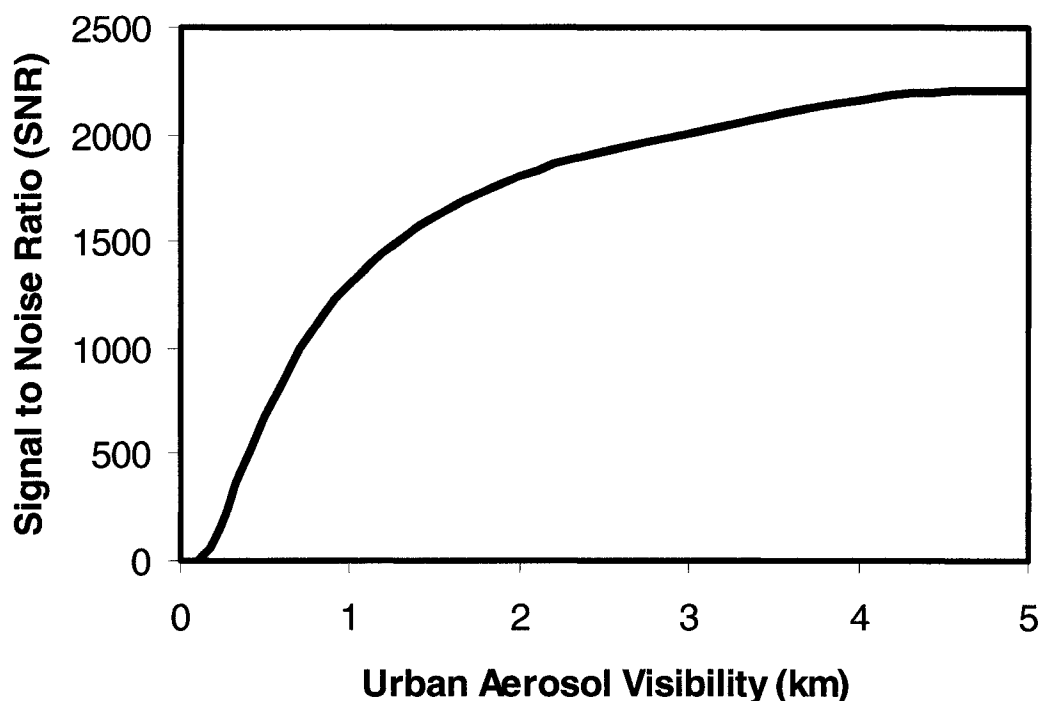
Figure 2-13. Signal-to-Noise Ratio (SNR) as a function of urban aerosol surface meteorological range (visibility) in the boundary layer (0 km to 2 km above the surface). Urban aerosols with high levels of sulfate are similar to smoke aerosols. Fire detection is possible for even intense levels of aerosols with visibility as low as 100 meters.

These results are similar to the expected fire detection performance through smoke aerosols and therefore, add to the credibility of the modeled smoke cases. In both cases, fire detection through these small aerosols is promising for reasonable concentration levels of particulates.

An evaluation of photos from numerous fire scenes suggests an active fire front is frequently not covered with thick smoke inhibiting fire detection. Wind will tend to blow smoke downwind of the active fire region, allowing unobstructed views of the high-temperature flame front (Figure 2-14). In fire events with complicated boundaries from

multiple sources, this may not be true. As fires grow large and boundaries become more

defined, a continuous fire front is more likely.

Figure 2-14. Photograph of an active fire front. Wind driven fires often tend to push thick smoke far downwind of the active fire front allowing the front to have improved exposure for remote sensing. Larger fires with an extended frontal region have a greater tendency to exhibit this behavior.

In all cases the ability to monitor a fire through smoke or clouds will depend on

the sensitivity of the detector and its ability to resolve small changes in radiance. If a fire

is detected in the presence of clouds or smoke one can assess its location and extent, but

the ability to resolve accurate fire temperatures is doubtful. This information would

depend on a knowledge of the cloud or smoke parameters which could only be partially

resolved with more detectors at other spectral bands and even then, is well beyond the

scope of this research. Therefore, this research has concentrated on the limitations of fire

detection as they apply to resolving fire perimeter locations and the extent of their spread

and relative intensity. These results are critical to the fire growth model defined in

Chapter III of this research.

CHAPTER III. PROPAGATION MODELING

Fire Propagation Models

The ability to mathematically model and predict wildland fire propagation for varying fuel and meteorological conditions is an important, difficult and largely unsolved problem. The behavior of wildland fires is based on a complicated set of parameters that describe the rate of spread, the fire perimeter shape and the intensity of the burning biomass (Albini, 1984). The basis for most fire behavior modeling is the Rothermel (1972) model. This model calculates the local intensity and rate of spread for the head of a surface fire based on wind and fuel parameters. The Rothermel local behavior predictions can be combined with a model of fire shape and spread (Anderson, 1983) to predict the spatial spread of a fire over time. The majority of existing fire spread models use the empirical Rothermel algorithms as the basis for calculation. Predicting wildfire behavior has been the subject of much research (Cheney et al., 1998; Richards and Bryce, 1995; Burgan and Rothermel, 1984; Albini, 1984, 1976) over the 30 years since Rothermel first introduced his algorithms. Ground-based fire models such as BEHAVE (Andrews, 1986) and FIREMAP (Vasconcelos and Guertin, 1992) are the most recent examples of operational models for field use based on empirical data. In all cases these approaches rely on an accurate assessment of the fuel conditions and the atmospheric conditions. The availability and variability of these parameters makes it extremely

76

difficult to predict wildfire behavior over long time intervals. In the case of field management, firefighters are able to make measurements of atmospheric and fuel parameters in specific locations and then use handheld computers to predict short-term propagation. Though this is effective in the local region of the measurement, the entire fire region is not sampled. With the aid of satellite imagery, large regions can be sampled to determine their temperature and propagation history. Though this does not provide fuel or atmospheric conditions in the local region, it does provide a real-time history of the fire temperature and propagation, which ultimately depend on these ground-based parameters. It is proposed that these temperature and propagation results could be extrapolated in time and position to predict the propagation of a fire and the areas of high intensity. This extrapolation is based on the assumption that the region near the fire front has homogeneous terrain and atmospheric conditions. This assumption is likely valid for near-term propagation predictions, but as with any fire model, fails at extended time due to fuel and atmospheric variability.

Existing fire models fall into two basic categories: those using a grid-based discrete system, or Cellular Automata (CA) models, and those using a continuous non-discrete system, or differential equation models. This research uses a grid-based discrete system to map the measured empirical fire spread data to discrete locations within the footprint. Once known, these parameters provide the basis for propagating a CA model to achieve fire spread forecasts. Using a non-discrete method for propagating a fire would require numerous boundary conditions, known atmospheric conditions, and a large set of linked partial differential equations. The solution for such a system would be highly complex and require significant computer time.

Partial differential equations can be used to describe the growth of a fire for

homogeneous wind and fuel conditions (Richards, 1995). The fire perimeter can be

located at specific time intervals as closed continuous curves, known as isopleths. Small

discontinuities are typically insignificant and ignored, though large time and spatial

scales are considered. Propagation of a fire over time yields perimeter shapes such as

standard ellipses (Catchpole et al., 1982; Anderson, 1983), double ellipses (Albini, 1976),

lemniscates and ovoids (Peet, 1967) as shown in Figure 3-1. The most common fire

perimeter shape and the one used by most ground-based wildfire models is the standard

ellipse. Whether one uses non-discrete or discrete modeling approaches, a consistent

trend is the use of elliptical spread shapes for fire propagation.
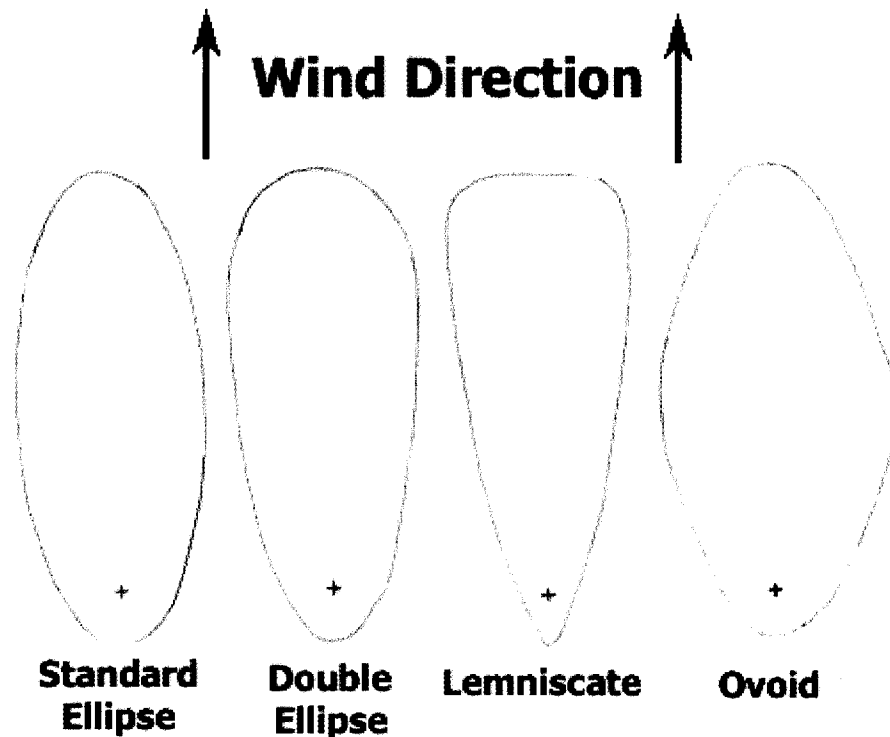
Figure 3-1. Various fire perimeter shapes in the equilibrium phase. Though wind and fire fuel parameters can impact spread shape, the standard ellipse shape is widely accepted and preferred in the fire modeling community.

Most non-discrete models assume elliptical spread shapes with Rothermel (1972) or McArthur (Noble et al., 1980) rate-of-spread functions to predict forward movement. As previously stated, their disadvantage lies in the complexity of the equations and the required boundary condition data. Additionally there are problems with concavities and loops (Richards, 1990; Richards and Bryce, 1995; Knight and Coleman, 1993) in the predicted shapes that require clever numeric solutions which add to the overall computational burden. These problems are nonexistent in discrete methods further exemplifying the complexity of non-discrete methods as compared to a discrete CA approach.

Cellular Automata Modeling

Many physical systems in nature are characterized by their highly complex behavior. These include fluid flow, crystal growth and wildfire propagation. It has been shown that the behavior of these dynamic systems can be duplicated using the simplistic method of CA modeling (Wolfram, 1984). All of the CA models presented in this chapter were developed using FORTRAN-90 (Anon, 1998) on a personal computer. This choice of computer language does not imply that the code is exclusively formulated for FORTRAN-90. Familiarity with FORTRAN coding and subroutines was the primary driver for this choice, though it is entirely possible to formulate this model in any other computer code. A variety of CA cases will be discussed throughout the chapter. Only the generic portion of the final fire propagation code has been listed in Appendix 1, since it is the core of the model and represents the key CA algorithms. Numerous available subroutines and personally developed code were used to verify the elliptical shape algorithms, but the basic set of CA algorithms is the only data required for implementation in a future fire propagation model.

The discrete method of CA fire modeling is based on a homogenous matrix of cells representing the ground footprint of a fire scene. The local state of each cell depends on the burn fraction of that cell. Cells that are unburned have an initial state of 0.0. Cells that are completely burned have a state of 1.0. If a cell state exceeds 1.0, the cell state is reset to 1.0, thereby eliminating infinite cell state values. As a fire progresses

across a landscape, the cells will ignite from the initial state and completely burn after

some time depending on the spread rate of the fire.

The cellular automata method presented in this research could be classified as a

coupled map lattice (CML), since the local state of a single cell depends on the state of its

neighboring cells (Figure 3-2).

$S_{i-1,j+1}$	$S_{i,j+1}$	$S_{i+1,j+1}$
$S_{i-1,j}$	$S_{i,j}$	$S_{i+1,j}$
$S_{i-1,j-1}$	$S_{i,j-1}$	$S_{i+1,j-1}$
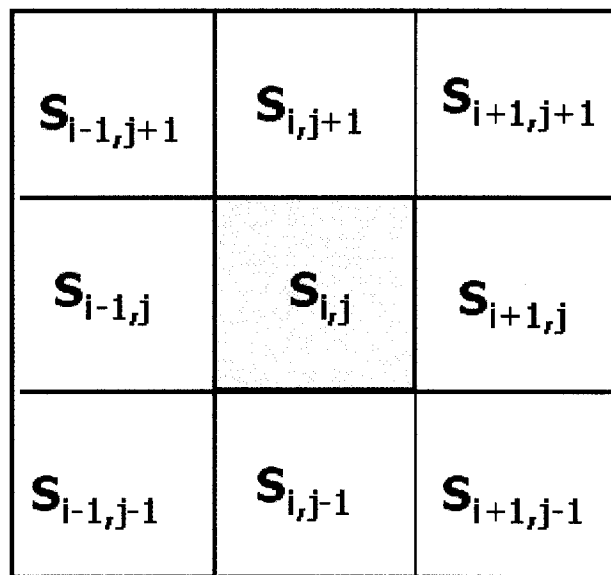
Figure 3-2. Cellular Automata cell structure depicting central cell and surrounding cells in a two-dimensional lattice form. The central cell state is coupled to its surrounding cells and can therefore represent fire ignition and propagation.

The state of the central cell $S_{i,j}$ at some future time step (t+1) can be expressed as

a function of its neighboring cells at the previous time step (t). One can use the four

orthogonal neighbors, known as a Von Neumann neighborhood (Von Neumann, 1966),

or the eight closest neighbors, known as a Moore neighborhood (Toffoli and Margolus,

1985). As previously stated, the state function is limited to cell state values of 1.0, so a

minimization function is also included. These cell state equations are known as the CA rules for this model.

4-Cell Approach:

$$S_{i,j}^{t+1} = \min \begin{bmatrix} 1.0, & S_{i,j}^t + f(S_{i-1,j}^t + S_{i,j+1}^t \\ + S_{i+1,j}^t + S_{i,j-1}^t) \end{bmatrix} \qquad (3\text{-}1)$$

8-Cell Approach:

$$S_{i,j}^{t+1} = \min \begin{bmatrix} 1.0, & S_{i,j}^t + f(S_{i-1,j}^t + S_{i,j+1}^t + \\ S_{i+1,j}^t + S_{i,j-1}^t) + D_o \cdot f(S_{i-1,j+1}^t + \\ S_{i+1,j+1}^t + S_{i+1,j-1}^t + S_{i-1,j-1}^t) \end{bmatrix} \qquad (3\text{-}2)$$

In the case of the eight cell approach, a diagonal factor (D_o) is introduced to decrease the weighting of the diagonal cells connected to the central cell. Karafyllidis and Thanailakis (1997) argued that this diagonal factor is $2(\sqrt{2} - 1) \approx 0.828$. An analysis of the diagonal factor in this research has determined this is in error by a factor of 4. A correctly chosen diagonal factor should yield a near-perfect circular spread shape. The following discussion will justify this finding.

The probability of a fire propagating from cell A to B (P_{AB}) depends on the distance between cell centers (L_{AB}) and the cross-sectional area between cell centers (A_{AB}). The baseline case is a square cell with a side dimension of 1.0 and a probability of ignition between these cells of 1.0 (Figure 3-3).

$$L_{AB} = 1.0$$
$$A_{AB} = L_{AB} * L_{AB} = 1.0$$
$$P_{AB} = 1.0$$
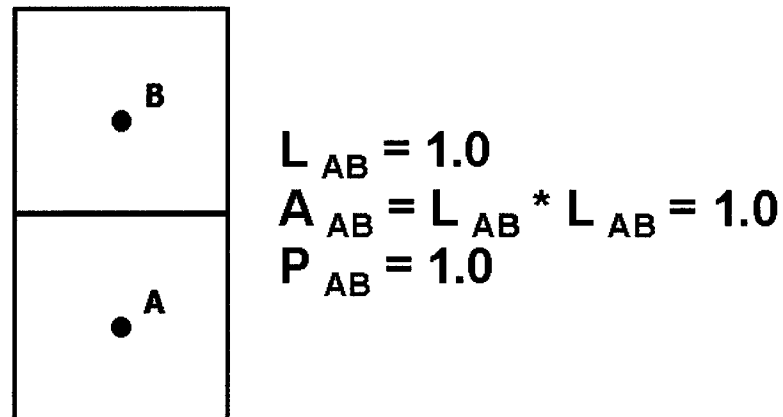
Figure 3-3. Baseline cell configuration with a probability of ignition between A and B of 1.0. Length dimension and Cross-Sectional Area are also 1.0. CA Model rules are based on these ignition probabilities.

If a cell has a dimension of $\sqrt{2}$ the distance between cell centers reduces the

ignition probability to $\sqrt{2} - 1 \approx 0.414$. In this case (Figure 3-4), the cross-sectional area

between cell centers is similar to Figure 3-3, in that the area is the square of the length

dimension. Only the longer distance between cell centers reduces the probability.

$$L_{AB} = \sqrt{2} \approx 1.414$$

$$A_{AB} = \left(\sqrt{2}\right) \cdot \left(\sqrt{2}\right) = 2$$

$$P_{AB} = \left(\frac{A_{AB}}{L_{AB}^2}\right)(L_{AB} - 1) = \left(\frac{2}{2}\right)\left(\sqrt{2} - 1\right) \approx 0.414$$
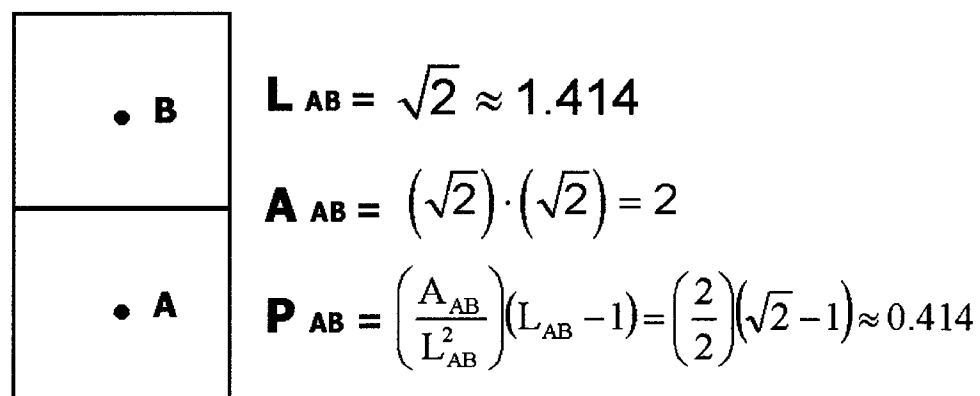
Figure 3-4. Cell configuration with larger dimensions. The cross-sectional area is the square of the length dimension. The increased distance between cell centers reduces to probability of ignition.

Now consider the more interesting diagonal case (Figure 3-5). Assuming a side

dimension of 1.0, similar to Figure 3-3, the distance between the cell centers is

$\sqrt{2}$ (similar to Figure 3-4), but the cross-sectional area is only one-half of the square of

the length dimension. Therefore, the probability of ignition is further reduced to

$\dfrac{\sqrt{2}-1}{2} \approx 0.207$. This value differs from the diagonal factor of Karafyllidis and

Thanailakis (1997) by a factor of 4, since their documented value was 0.828.

$$L_{AB} = \sqrt{2} \approx 1.414$$

$$A_{AB} = \frac{\left(\sqrt{2}\right)\cdot\left(\sqrt{2}\right)}{2} = 1.0$$

$$P_{AB} = \left(\frac{A_{AB}}{L^2_{AB}}\right)(L_{AB}-1) = \left(\frac{1}{2}\right)\left(\sqrt{2}-1\right) \approx 0.207$$
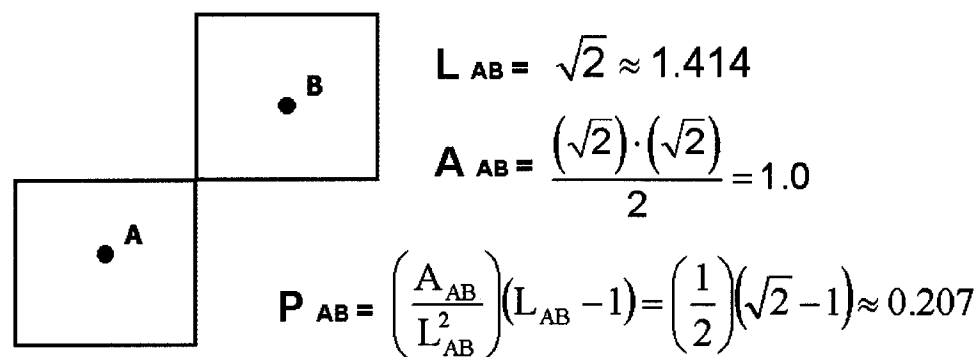
Figure 3-5. Diagonal cell configuration has a reduced probability due to smaller cross-sectional area (one-half of the orthogonal cases) and a larger length dimension (similar to Figure 3-4). This probability factor will replace the factor used by Karafyllidis and Thanailakis (1997) to optimize circular spread shapes.

A variety of diagonal factors were tested in the CA model and compared with

exact circles. The most simplified case of a perfect circle represents fire spread in the

absence of wind. The diagonal factor presented in this research (0.207) yields errors less

than 0.1% (Figure 3-5) when compared to the factor (0.828) used by Karafyllidis and

Thanailakis (1997).
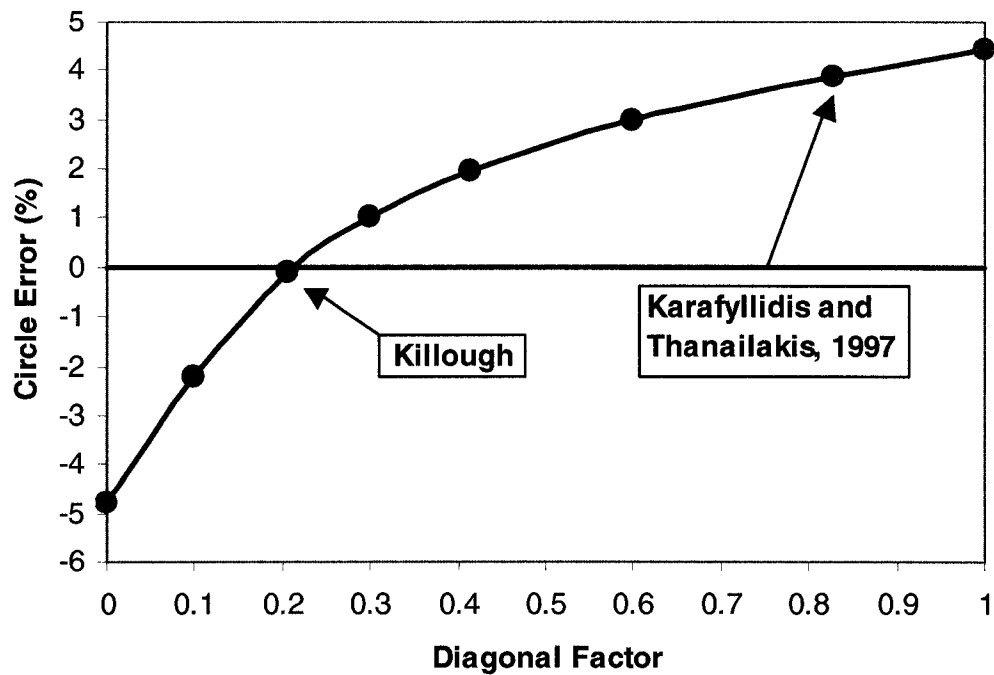
Figure 3-6. Circle shape error versus CA diagonal factor. The shape error is calculated against a perfect circle in 3 locations along the perimeter. The diagonal factor of 0.207 clearly models circular growth better than that presented by Karafyllidis and Thanailakis (1997).

A qualitative comparison of shape error is possible using contour plots from the CA model of simple fire growth with no wind. Figure 3-7 shows contour plots using a diagonal factor of 0.207 and 0.828. The smaller factor clearly represents a smooth circular contour, whereas the larger factor, with shape errors near 4%, displays distorted contour shapes. An accurate diagonal factor is important for an 8-cell CA model to accurately model near-circular spread shapes. Many fires exhibit these shapes in low wind conditions. Additionally, accurate circular models will help to avoid further distortion when translating these CA algorithms to elliptical spread shapes common in wind-driven fire conditions.

Factor = 0.207   Factor = 0.828
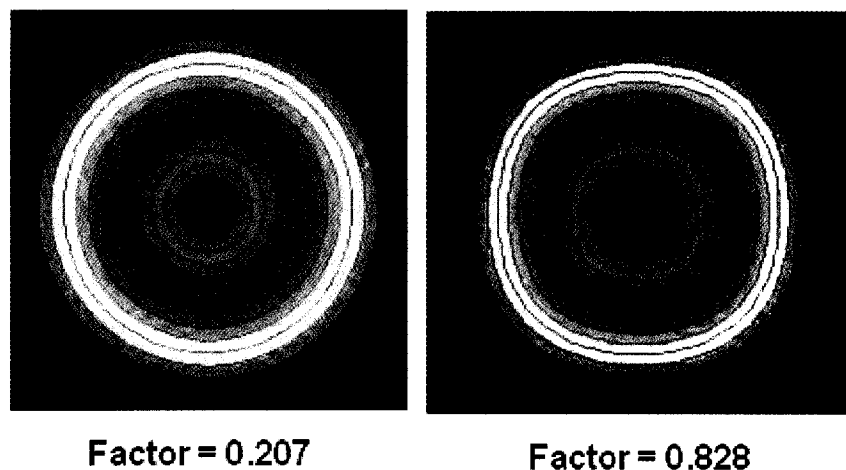
Figure 3-7. Cellular automata spread contours for two diagonal factors. Physical dimensions and time are equal, yet arbitrary. The factor of 0.207 produces near-circular shapes with little or no distortion. The factor of 0.828 produces noticeable contour distortion. Modeling fire spread in low or no wind conditions requires accurate modeling of circular spread.

Wind is the most important driving factor in the spread of wildland fires (Beer, 1993; Richards, 1990; Alexander, 1985; Anderson, 1983; Rothermel, 1983). Though an effective wind velocity in the vicinity of the fire perimeter may be known, its local velocity at the fire front may vary. This local velocity is ultimately responsible for the fire spread at all points along the perimeter. The significance of this situation is that empirical data of fire spread could be used to assess this local wind and fire interaction. Measuring the local fuel and wind parameters along a fire front is not feasible, but measuring fire parameters from remote sensing applications is possible. It is anticipated that fire propagation can be predicted using empirical data from a geosynchronous satellite. The active fire front locations can be identified using high temperature thresholds for flaming conditions. Once these positions are known the rate of spread can

be calculated in the same positions based on time integration over neighboring areas. Assuming homogeneous fuel parameters and a constant wind, the fire can be propagated using a CA model that assumes an elliptical spread shape. This research develops a classic CA approach and then demonstrates its potential use with a satellite fire detection system. The performance of such a system is measured against real fire events, theoretical equation models of fire spread and empirical models of fire spread.

The effect of wind is accommodated in the CA model by adding a non-uniform weighting function to the CA local rule. These weighting functions connect the local cellular structure and can be thought of as variable probability factors for fire spread in a particular direction. For instance, higher weighting factors would equate to a high probability that the fire would spread in that direction. In the 8-cell case the weighting is based on the cardinal wind directions (Figure 3-8) and corresponds to the surrounding eight cells of any one cell in the model. The cardinal wind directions and adjusted CA local rule are:

$$S_{i,j}^{t+1} = S_{i,j}^t + (W7 * S_{i-1,j}^t + W1 * S_{i,j+1}^t + W3 * S_{i+1,j}^t + W5 * S_{i,j-1}^t) +$$
$$D_o \cdot (W8 * S_{i-1,j+1}^t + W2 * S_{i+1,j+1}^t + W4 * S_{i+1,j-1}^t + W6 * S_{i-1,j-1}^t)$$

(3-3)

where W1 = South Wind, W2 = Southwest Wind, W3 = West Wind, W4 = Northwest Wind, W5 = North Wind, W6 = Northeast Wind, W7 = East Wind, and W8 = Southeast Wind.
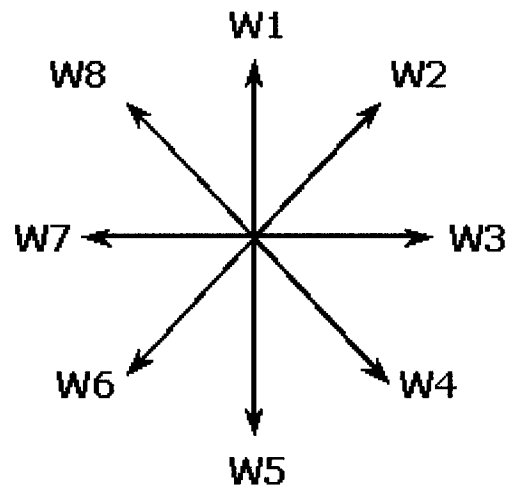
Figure 3-8. Cellular Automata weighting factors representing the eight cardinal wind directions. Weighting factors impact fire position and shape.

Elliptical Fire Spread Shapes

The approach for space is based on measuring real-time locations of the fire perimeter and determining the rate of spread in the heading direction (V_H) and the backing direction (V_B). Careful evaluation of the measured data over time will allow determination of these parameters. This will be accomplished by finding the areas of the detector footprint with high temperatures (likely corresponding to the fire perimeter) and then evaluating their growth rate and direction. Once the maximum heading rate and direction are found, the backing rate and direction will be found by measuring the same parameters in the opposite coordinate direction (180 degrees from the heading direction). In most cases, the backing rate will reflect the lowest spread rate in the entire scene and may not correspond to the direction exactly opposite the heading direction. With the known heading and backing spread rates, the fire will be propagated with specific ellipse spread shapes. The ellipse spread shapes are measured by the length to breadth ratio (L/B) of the ellipse (Figure 3-9).
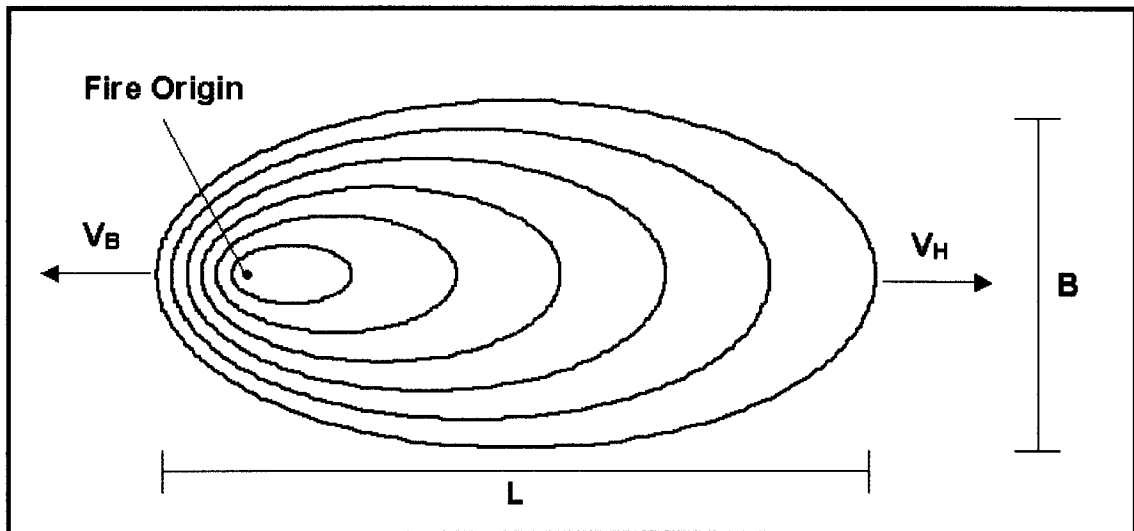
Figure 3-9. Elliptical fire spread shapes are measured by the length (L) and breadth (B) ratio (L/B) corresponding to the heading velocity (V$_H$) and the backing velocity (V$_B$) directions. The heading velocity is in the direction of maximum fire spread rate.

Alexander (1985) developed an empirical relationship between the length to breadth ratio (L/B) of a wind-driven forest fire and the international standard 10-meter open wind speed in kilometers per hour.

$$\frac{L}{B} = 1.0 + 0.0012 \; W^{2.154} \tag{3-4}$$

This relationship was based on data from 29 fires from 1938 to 1983 (Figure 3-10).
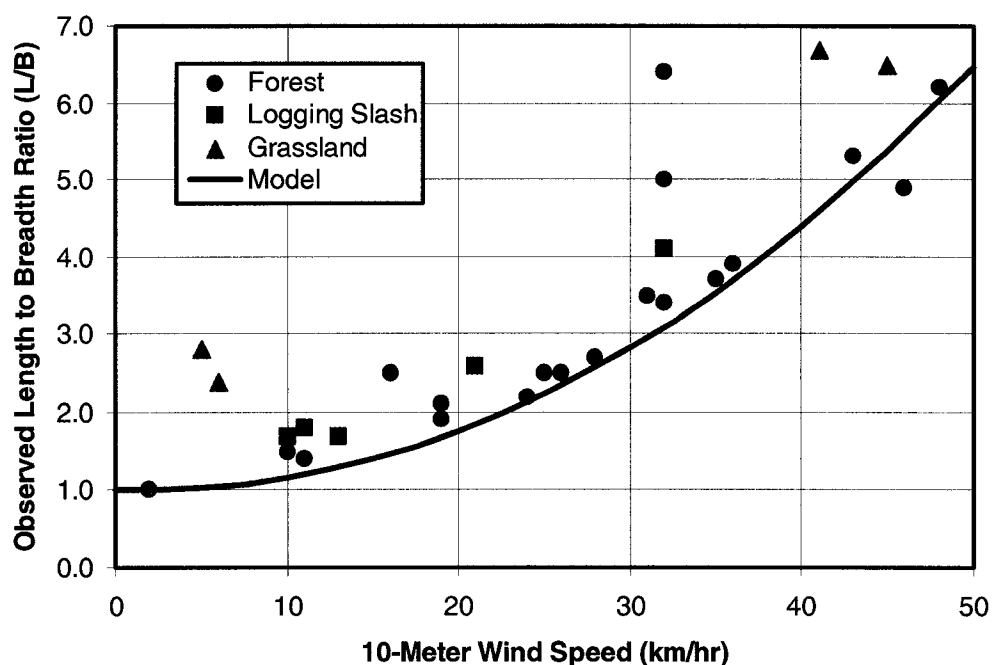
Figure 3-10. Length to breadth (L/B) elliptical fire spread ratio as a function of 10-meter open wind speed for 29 forest fires (Alexander, 1985). The model, developed by Alexander, was primarily fit to forest fuels, but logging slash and grassland were included for comparison. Elliptical spread shapes (L/B) clearly depend on wind velocity.

Though this model is empirical in nature, it clearly shows a relationship between wind speed and fire shape. Obviously, wind speed cannot be measured from space, so other data must be utilized. Therefore, heading and backing spread rates must be determined for propagation modeling from space.

Alexander (1985) developed a relation between the length to breadth ratio (L/B) and the heading to backing velocity ratio (V_H/V_B) that is entirely based on elliptical mathematic equations.

$$\frac{V_H}{V_B} = \frac{\dfrac{L}{B} + \sqrt{\left(\dfrac{L}{B}\right)^2 - 1}}{\dfrac{L}{B} - \sqrt{\left(\dfrac{L}{B}\right)^2 - 1}}$$ (3-5)

The desire was to measure the L/B ratio in the field and predict V_H/V_B ratios. In this approach, the V_H/V_B parameter is the independent variable and thus the equation was inverted to obtain a formula more useful for this research and space applications.

$$\frac{L}{B} = \frac{\dfrac{V_H}{V_B} + 1}{2\sqrt{\dfrac{V_H}{V_B}}}$$ (3-6)

In this case a computed heading velocity (V_H) and backing velocity (V_B) are used to calculate the elliptical L/B ratio which becomes the basis for future propagation. The premise of the approach is that once the heading and backing velocity are computed via space measurements, the fire can be propagated in time with a length to breadth ratio according to this relationship (Figure 3-11).

Ratio of Headfire Spread Rate to Backfire Spread Rate (V$_H$/V$_B$)
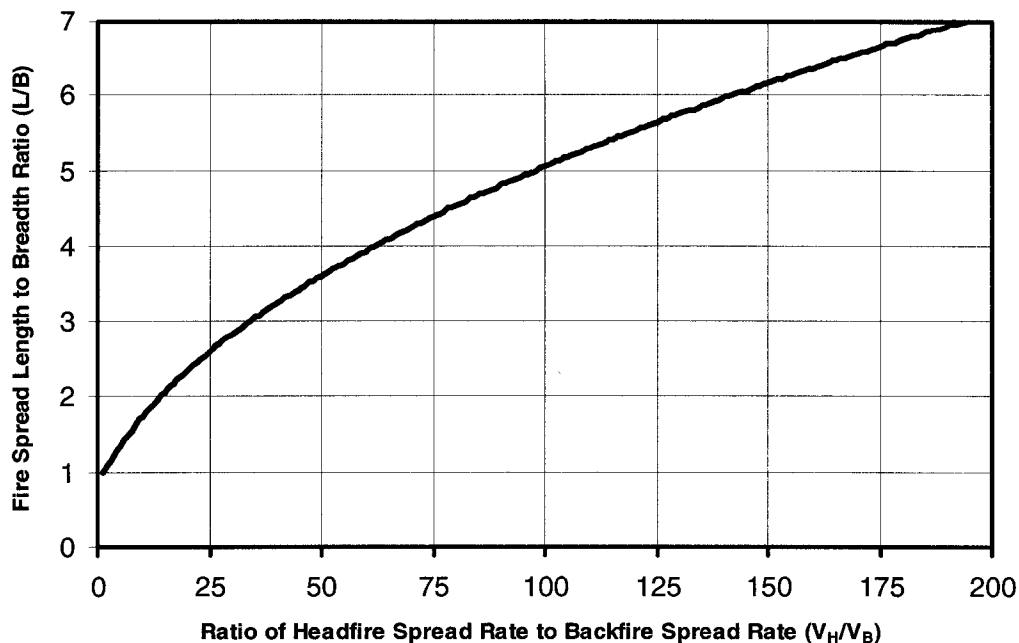
Figure 3-11. Fire spread length to breadth ratio (L/B) as a function of heading to backing velocity ratio (V$_H$/V$_B$). Measured spread velocities from space can be used to propagate a CA model to predict future fire locations according to elliptical spread parameters (L/B).

The real strength in this approach lies in the ability to use space-based information rather than rely on sparse ground-based data that is likely taken at the wrong location and untimely for rapidly changing fires. The spread relationship shown in Figure 3-11 is not based on empirical data, but solely on mathematical manipulations of ellipse equations. Therefore, the only true assumption in the entire process is that fires spread in elliptical shapes (Figure 3-12). As previously discussed, this is a good assumption and one generally accepted by the fire community.

Figure 3-12. Photograph of a typical wildland fire obtained from the USDA Forest Service. The active fire front is propagating downwind in an elliptical shape pattern. These spread shapes are typical of modeled and actual fires.

The ability to accurately represent elliptical spread shapes was tested using 4-cell and 8-cell CA models. The ellipse perimeter contour shapes generated at each time step were compared to a geometrically exact ellipse at three locations (Figure 3-13). First the length-to-breadth (L/B) ratio is calculated at each time step and then the actual perimeter is compared with a true ellipse having the same L/B ratio at three quadrant locations. In the headfire direction, errors are calculated at one-half the semi-major axis and three-fourths of the semi-major axis. In the backfire direction, the quadrant error is only calculated at one-half the semi-major axis.
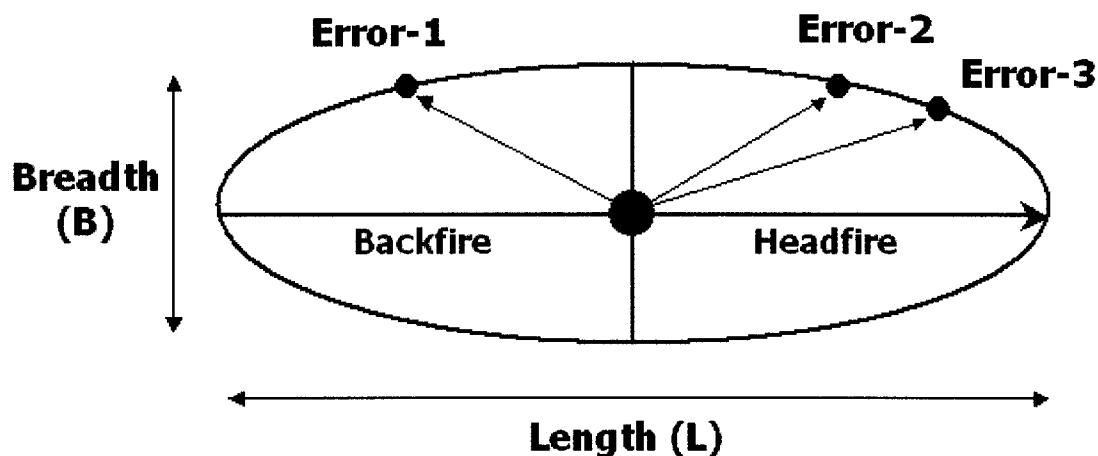
Figure 3-13. CA models of elliptical spread shapes were compared with geometrically perfect ellipses at three quadrant locations. Errors can be minimized to create CA weighting algorithms for accurate fire spread modeling.

Both the 4-cell and 8-cell CA models were tested to simulate theoretical ellipse shapes. Assuming symmetrical growth with respect to the major axis, the 4-cell model has three free weighting parameters (W7, W1, and W3) and the 8-cell model has five free weighting parameters (W7, W8, W1, W2, W3). The factor W3 was fixed at 1.0 for all cases, since the parameters can be scaled with respect to W7 to achieve various rates of spread. Therefore, there were actually two free variables for the 4-cell model and four free variables for the 8-cell model. Scalability and rate of spread will be discussed in more detail in later sections.

The weighting parameters correspond to the cardinal directions shown in Figure 3-8. CA computer subroutines were developed to alter a single free parameter, while fixing the remaining parameters. Though this is not a formal gradient-descent method, the approach yielded adequate results with minimal computational complexity.

An average ellipse quadrant error was calculated in each case to determine the desired change in the variable parameter for the next case. Using this iterative approach it was possible to test ellipse shape errors for the 4-cell and 8-cell models over a L/B range of 0 (circle) to 7 (elongated ellipse). Figure 3-14 shows the average quadrant error for numerous selected cases as well as curvefits for these data. A simplistic qualitative analysis suggests the 8-cell model is superior to the 4-cell model since it yields ellipse shape errors below 2% for all cases. The 4-cell model is too simplistic for simulating near circular shapes and ellipses with low L/B ratios (less than 3). In these cases, the errors are high and produce distorted spread shapes. Quantitatively, it could be argued that the 4-cell model is entirely suitable for L/B ratios above 3.0. The errors for these cases are nearly the same as the 8-cell case and computational complexity is lessened.
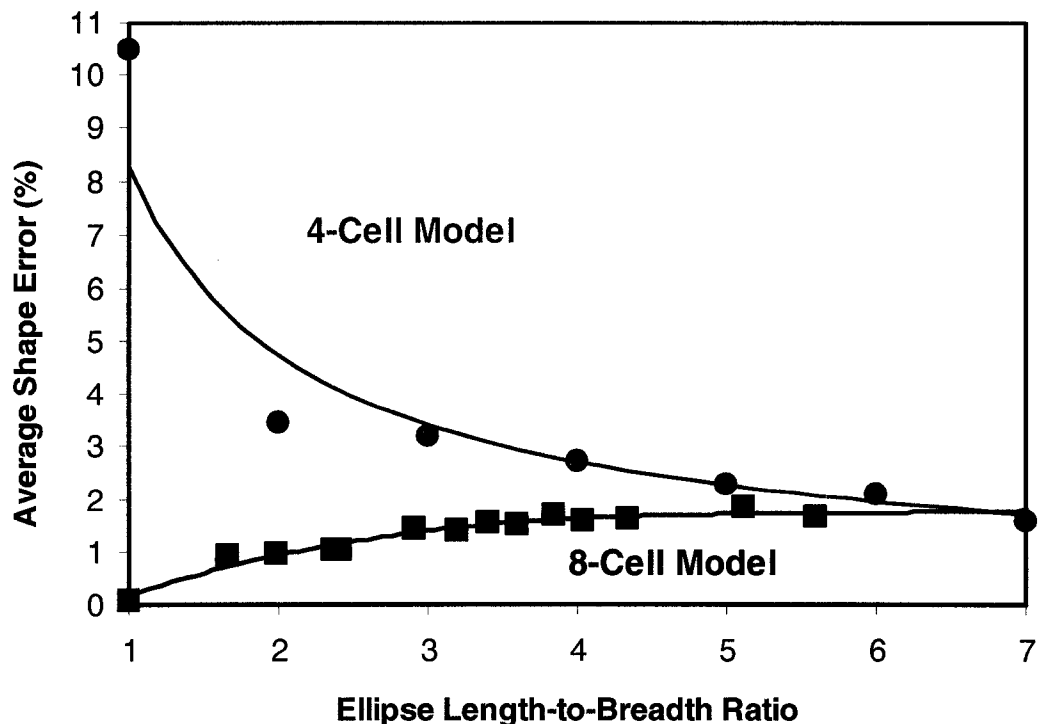
Figure 3-14. Average shape error compared to a perfect ellipse geometry defined by the ellipse length-to-breadth (L/B) ratio. The 8-cell model achieves errors below 2% for all cases, but the simplistic 4-cell model achieves nearly the same errors for L/B ratios greater than 3.0. Polynomial curvefits were used for illustration of general trends.

Further examination of the data raises the question of how much distortion is created with a 5%, 10% or 20% ellipse quadrant error. It may be possible to tolerate larger errors if the shape distortion is not severe. Figure 3-15 displays various distortions (0,5,10, and 20 percent) for a circular (L/B=1.0) case and an elliptical (L/B=3.0) geometry. Qualitatively, errors near 5% appear reasonable, though a 10% or 20% error severely distorts a circular and an elliptical fire.

Circle Model (L/D = 1.0)
Ellipse Model (L/D = 3.0)
Exact Geometry = BLACK line
Distorted Geometry = RED lines
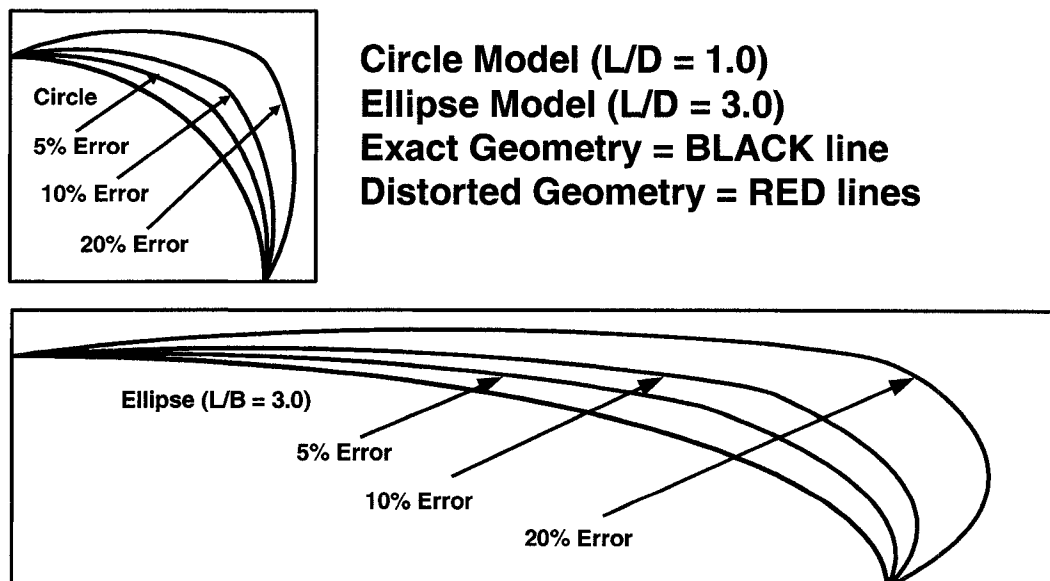
Figure 3-15. Circle (L/B=1.0) and ellipse (L/B=3.0) contour shapes with average distortion errors of 0,5,10, and 20 percent. High shape errors above 5% produce severely distorted spread shapes. Accurate fire propagation models cannot tolerate high distortions while maintaining spread accuracy. The CA algorithm developed in this research achieves less than 2% distortion error.

This qualitative argument supports an approach that utilizes an 8-cell method for L/B ratios between 1.0 and 3.0 and the more simplistic 4-cell method for L/B ratios between 3.0 and 7.0. The following piecewise algorithm was developed from the modeling results. Each free parameter weighting function was fit to an exponential curve for both the 4-cell model (Figure 3-16) and the 8-cell model (Figure 3-17). The final algorithm for each of the 8 reference weighting parameters is shown below as a function of the L/B ratio, which will be designated hereafter as β. These reference parameters are based on an elliptical expansion with a major axis in the vertical direction.

$$S_{i,j}^{t+1} = \min \begin{bmatrix} 1.0, & S_{i,j}^{t} + (W_7(\beta) * S_{i-1,j}^{t} + \\ W_1(\beta) * S_{i,j+1}^{t} + W_3(\beta) * S_{i+1,j}^{t} + \\ W_5(\beta) * S_{i,j-1}^{t}) + \\ D_o \cdot (W_8(\beta) * S_{i-1,j+1}^{t} + \\ W_2(\beta) * S_{i+1,j+1}^{t} + \\ W_4(\beta) * S_{i+1,j-1}^{t} + W_6(\beta) * S_{i-1,j-1}^{t}) \end{bmatrix} \quad \text{where} \quad W_1 = 1.0 \quad 1 \le \beta \le 7;$$

$$W_7 = W_3 = \begin{cases} e^{-3.52(\beta-1.0)} & 1 \le \beta \le 3 \\ 0.4e^{-0.88\beta} & 3 < \beta \le 7 \end{cases} \quad ; \quad W_4 = W_6 = \begin{cases} e^{-2.14(\beta-1.0)} & 1 \le \beta \le 3 \\ 0 & 3 < \beta \le 7 \end{cases} \tag{3-7}$$

$$W_8 = W_2 = \begin{cases} e^{-1.29(\beta-1.0)} & 1 \le \beta \le 3 \\ 0 & 3 < \beta \le 7 \end{cases} \quad ; \quad W_5 = \begin{cases} e^{-2.16(\beta-1.0)} & 1 \le \beta \le 3 \\ 1.44e^{-0.65\beta} & 3 < \beta \le 7 \end{cases}$$
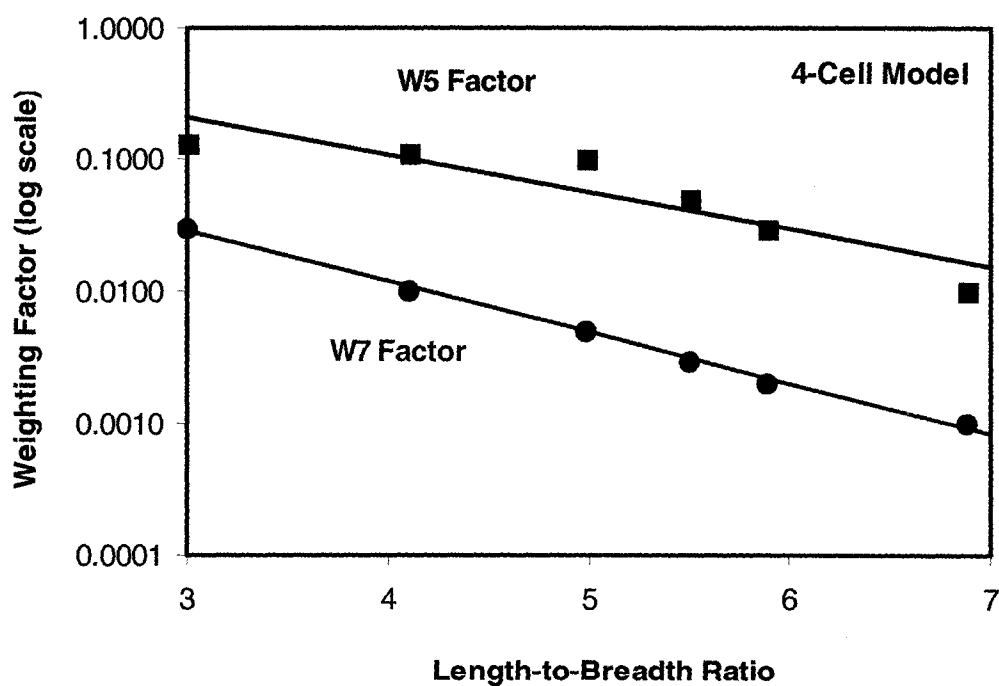
Figure 3-16. Free variable weighting factors as a function of length to breadth ratio for the 4-cell CA model. Exponential curve fits were used to develop a single algorithm for each parameter, W5 and W7. The R^2 regression errors were 0.827 and 0.996, respectively.
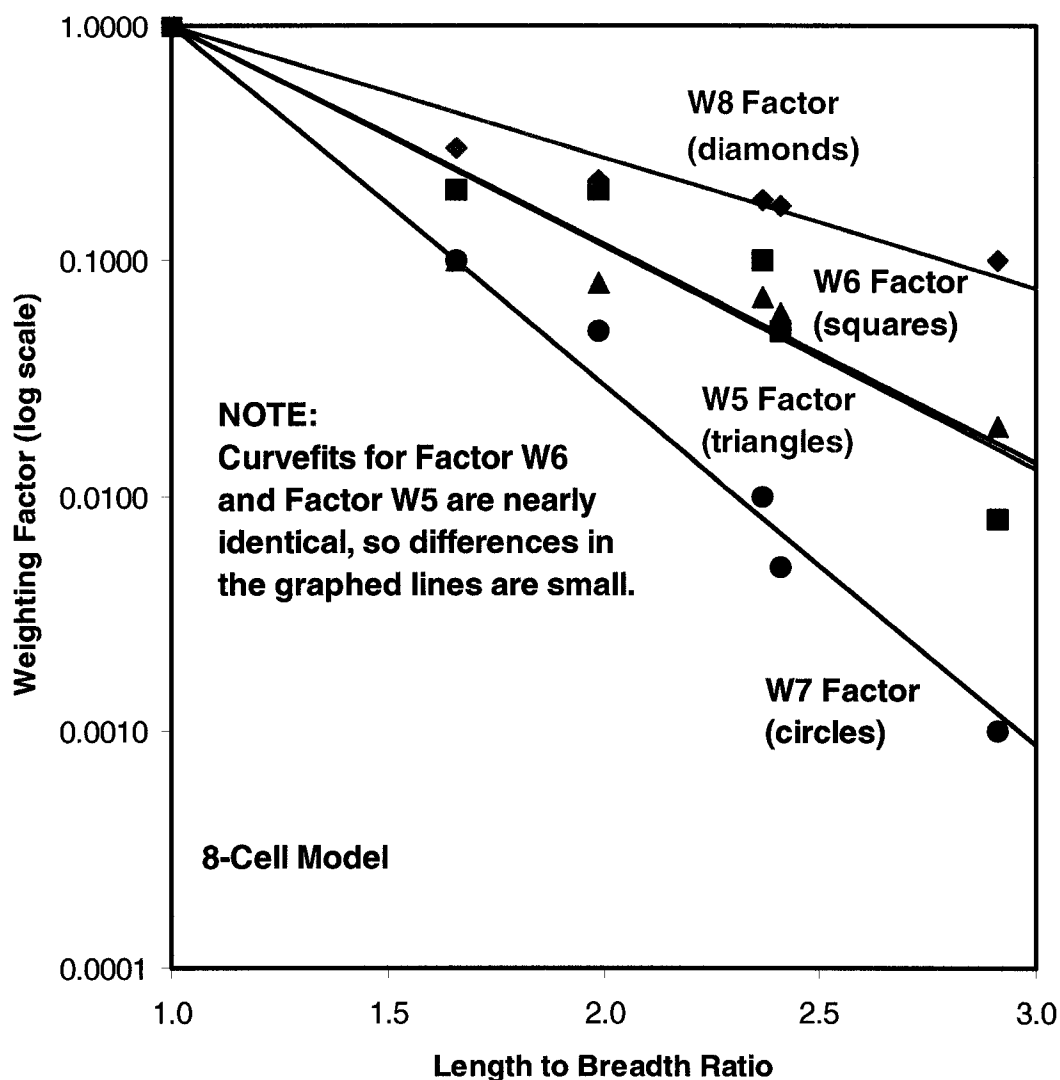
Figure 3-17. Free variable weighting factors as a function of length to breadth ratio for the 8-cell CA model. Exponential curve fits were used to develop a single algorithm for each parameter, W8, W6, W5, and W7. Each curve fit was forced to go through the intercept (1.0,1.0) to achieve a near-perfect circle at L/B = 1.0. The R^2 regression errors for each weighting function were 0.931, 0.905, 0.867, and 0.986, respectively.

Since the final algorithm is a curve fit of numerous weighting factors, its performance was tested over a range of β ratios (Figure 3-18). In all cases, elliptical quadrant errors are below 2% and accurately depict geometric shapes.
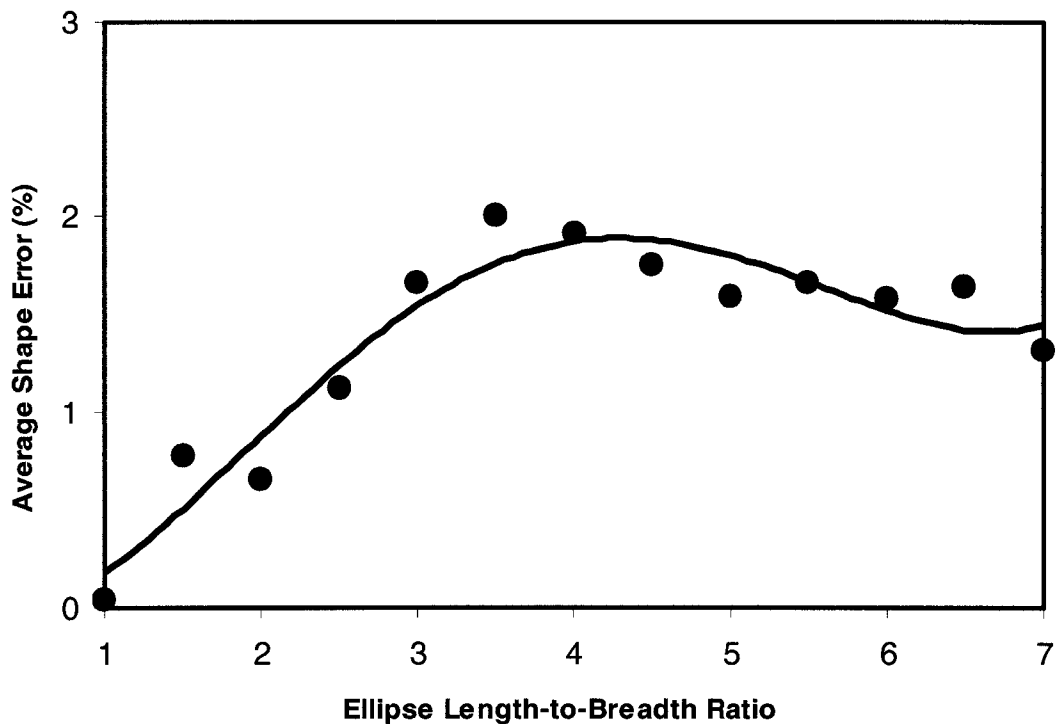
Figure 3-18. Geometric shape error as a function of length to breadth (L/B) ratio for the final CA algorithm. Average errors are below 2% for all cases. The piecewise CA algorithm utilizes an 8-cell model for $\beta \leq 3$ and a 4-cell model for $\beta > 3$. This single algorithm can form the basis for future CA fire propagation codes. A polynomial curve fit of the data is included for visualization purposes only.

Fire Model Algorithm

Now that the general algorithm has been presented, several issues must be considered to implement the code in a practical application case. First, the presented CA model does not produce instantaneous shape convergence. Assuming the fire starts from any fixed point in space, the shape of the fire perimeter will evolve over time to produce a converged value. Figure 3-19 shows the shape error as a function of iteration for a circular case β =1.0 and an ellipse β =4.0. Average errors are reduced below 5% after 120 iterations in both cases. Convergence to the desired elliptical shape requires minimal iterations and therefore minimal computing impact.
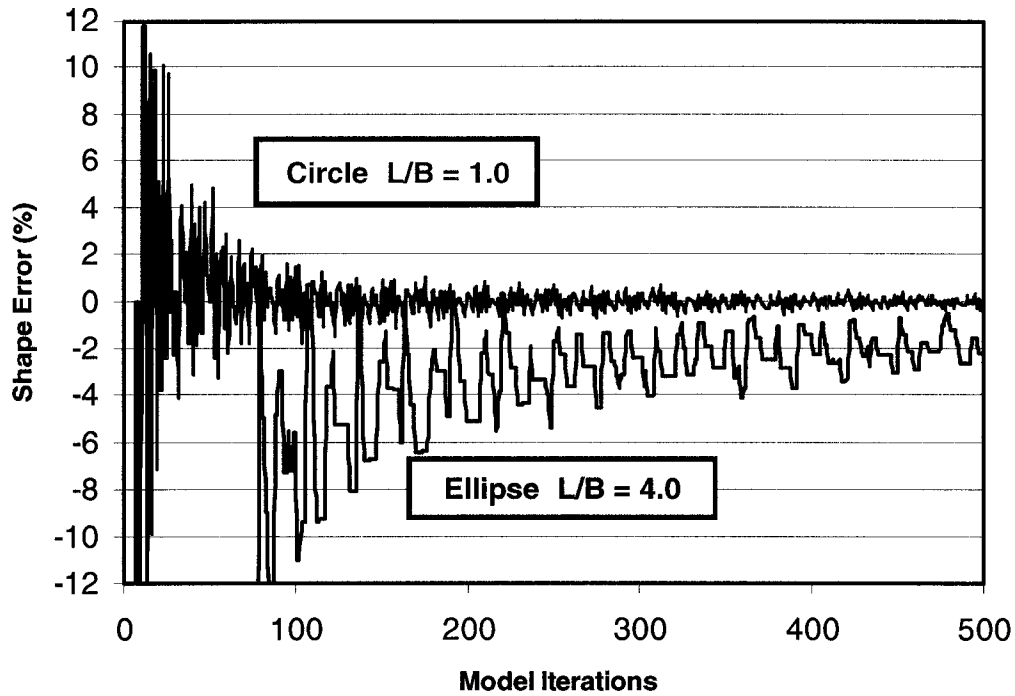
Figure 3-19. Geometric shape error as a function of CA model iterations. Average errors are reduced below 5% after 120 iterations for both the circle case (L/B = 1.0) and the ellipse case (L/B = 4.0). Errors are typically higher for ellipses due to their irregular shape. The small number of required iterations will consume minimal computer time for a real fire application.

Once convergence is met, the position of the fire boundary depends solely on the number of iterations. Each iteration can be thought of as a discrete increment of time which defines the temporal resolution of the model. In order to increase the rate of spread without an increase in iterations, an additional scaling factor (R) can be added to the algorithm.

$$S_{i,j}^{t+1} = \min \left[1.0, \quad S_{i,j}^{t} + R \cdot \begin{bmatrix} (W_7(\beta)*S_{i-1,j}^{t} + W_1(\beta)*S_{i,j+1}^{t} + \\ W_3(\beta)*S_{i+1,j}^{t} + W_5(\beta)*S_{i,j-1}^{t}) + \\ D_o \cdot (W_8(\beta)*S_{i-1,j+1}^{t} + W_2(\beta)*S_{i+1,j+1}^{t} + \\ W_4(\beta)*S_{i+1,j-1}^{t} + W_6(\beta)*S_{i-1,j-1}^{t}) \end{bmatrix} \right] \quad (3-8)$$

This scaling factor has an influence on shape error which grows with higher

spread rates. Figure 3-20 shows shape error as a function of scaling factor (R) for a

circular spread case (1.0) and an ellipse case (4.0). The algorithm developed in the

previous sections used a factor of 0.1 for all cases.
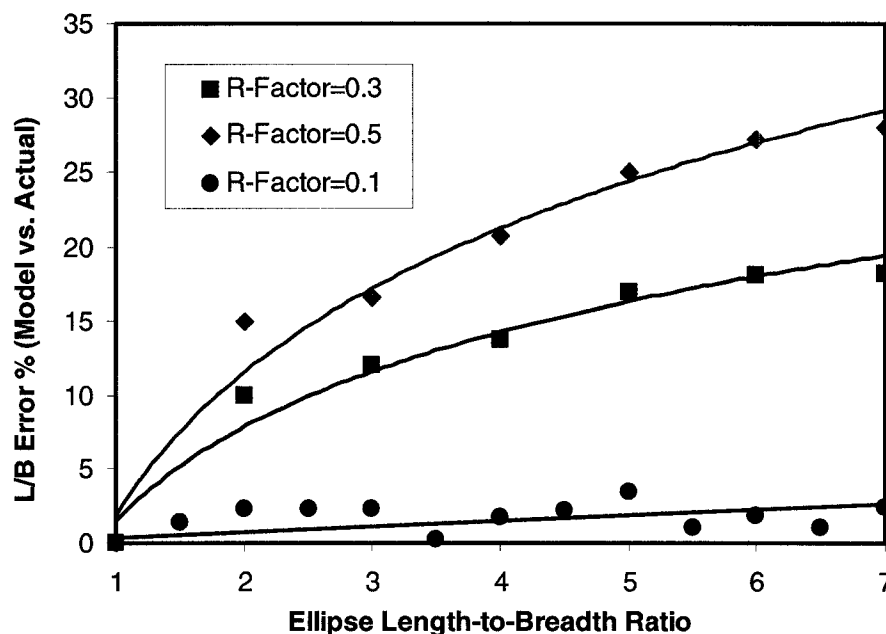
Figure 3-20. Quadrant shape error as a function of scaling factor. Scaling factors above
0.5 may distort spread shapes. Careful balancing of scaling factor and the number of
iterations will allow accurate fire spread rates.

Clearly large scaling factors tend to increase shape errors, but this can be avoided.

Choosing a small scaling factor of 0.10 will limit the shape error, but require more

iterations to achieve the same total spread distance. There are multitudes of combinations

of scaling factor, length to breadth ratio and iteration numbers that can be evaluated in

further research, but are far too extensive to list here. It is suggested that one fix the

scaling factor at 0.10 and specify the number of iterations to achieve the desired spread

rates. Spread rates are dependent on direction, but can be easily measured in the course

of a solution to adjust the number of iterations and achieve the desired spread rate.

Grid dependency is another parameter that should be considered for discrete-

based solutions. Finer cell sizes and larger grids should demonstrate no appreciable

change in the results. Grid dependency was tested for a circular case (L/B = 1.0) and an

elliptical case (L/B = 4.0). Average shape errors were measured for increasing grid size

(Figure 3-21). In each case the circle or ellipse filled nearly the entire grid space. This

was accomplished by increasing the number of iterations for larger grid dimensions.

Larger grid dimensions, corresponding to finer CA meshes, have little or no affect on

shape error results, and therefore, show the CA model is grid independent.
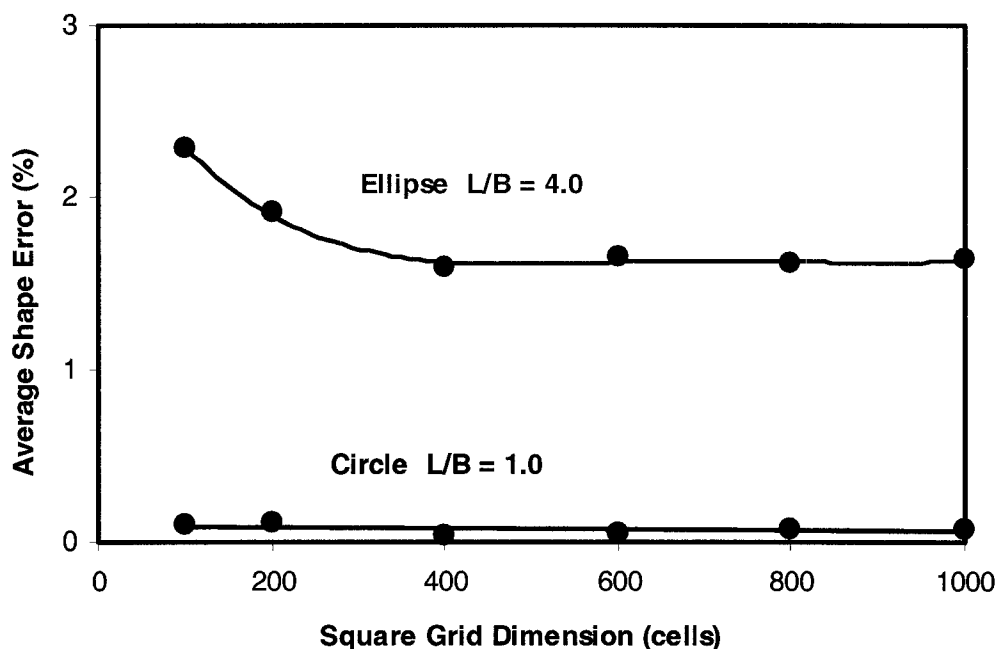
Figure 3-21. Average shape error as a function of square grid dimension. Circle shape errors are very small and nearly constant for increasing grid dimension. Ellipse shape errors converge to nearly constant values for grids larger than 400 cells. Constant shape errors for increasing grid dimensions show that the CA model is grid-independent.

The final parameter added to the CA weighting algorithm will account for variations in wind direction. Up to this point, the CA weighting algorithms have considered elliptical expansion with a major axis in the vertical direction. This would only be the case for a northerly wind. To account for winds in all directions, it is necessary to develop a coordinate rotation and adjust the wind factors for directions that fall between the 8 orthogonal or diagonal directions. Several assumptions will be considered: (1) Wind is measured clockwise from the vertical axis where a northerly wind corresponds to a wind direction angle of zero, as shown in Figure 3-22, (2) The previously calculated weighting functions will be called the reference weighting factors $W_X(ref)$, since they correspond to a zero degree wind direction, and (3) Wind direction will fall into one of 8 sectors (S), according to Figure 3-22.

Wind Direction Angle (α)
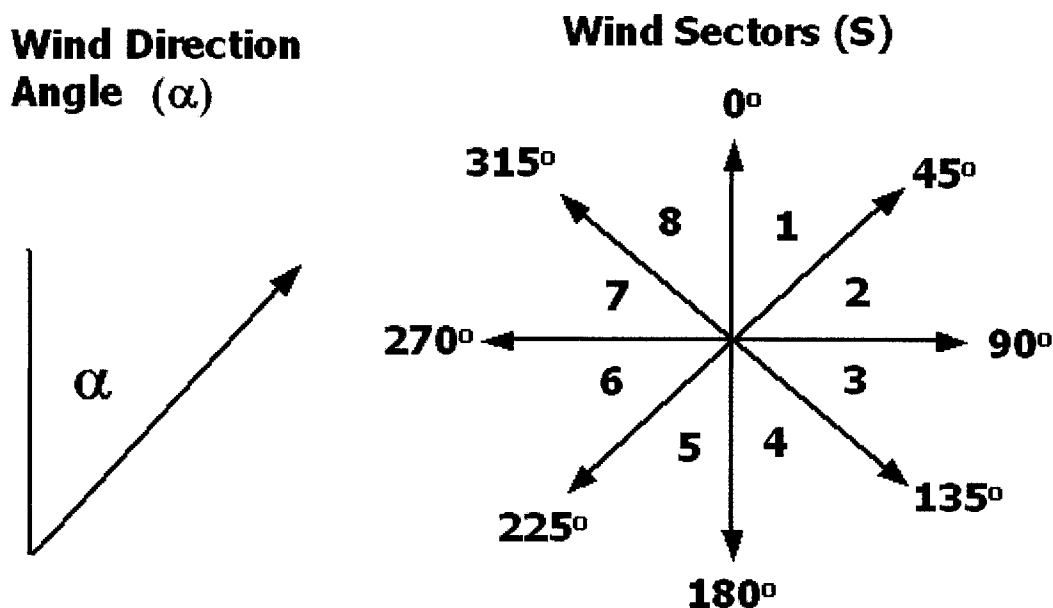
Wind Sectors (S)

Figure 3-22. Diagrams of wind direction and wind sector for calculating CA weighting factors. Factors can be adjusted for winds in any direction using a combination of the weighting factors closest to the sector containing the given wind direction.

Considering these assumptions, the wind weighting factor for any arbitrary wind

angle, $W_X(\alpha)$, can be written as a function of the wind angle (α), wind sector (S), and

the two reference weighting factors that bound the sector of that wind (W_{ref}). The wind

angle (α) is expressed in degrees, whereas the wind sector (S) is an integer value from

1 to 8.

$$W_X(\alpha) = \frac{\left[W_{X-S+8}(ref) \cdot \left[1 + \dfrac{\alpha}{45°} - S\right] + W_{X-S+9}(ref) \cdot \left[S - \dfrac{\alpha}{45°}\right]\right]}{45} \tag{3-9}$$

A variety of possible fire spread shapes and directions are possible with the

presented CA algorithm. Figure 3-23 shows a simulation of an elliptical fire in wind-

driven conditions emanating from a single point source. It is also possible to achieve

blended contours for spreading fires originating from numerous points with the same

elliptical spread shapes (Figure 3-24). In a typical space application, knowledge of the

wind direction is derived from the fire perimeter data which propagates in a direction

coincident with the wind.
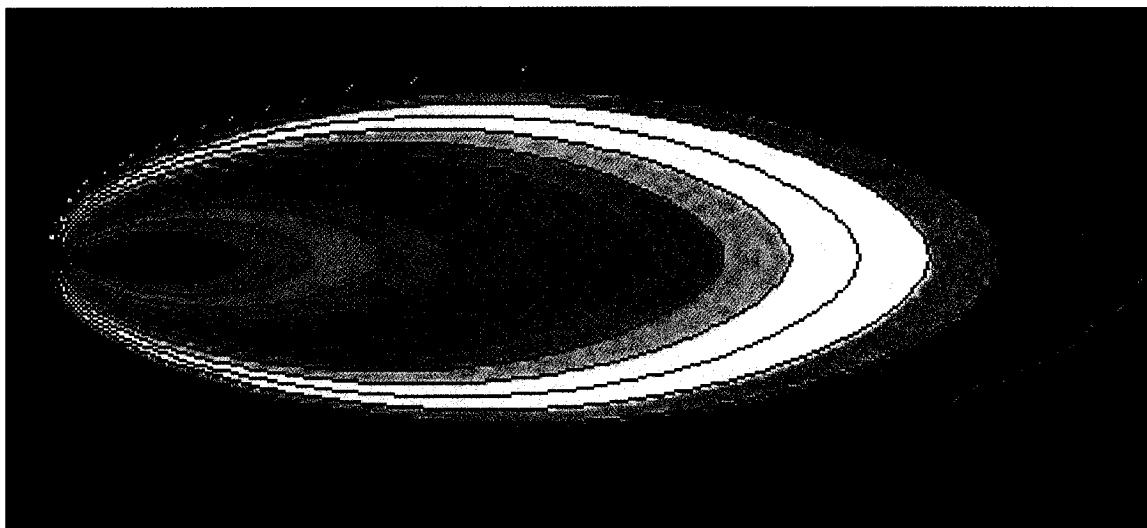
Figure 3-23. Cellular automata fire spread contours depicting fire boundary locations. The simulation used a wind angle of 90 degrees and a length-to-breadth ratio of 2.0, for 500 iterations. Unequal weighting factors create an elliptical fire spread shape typical of an actual fire in wind driven conditions.
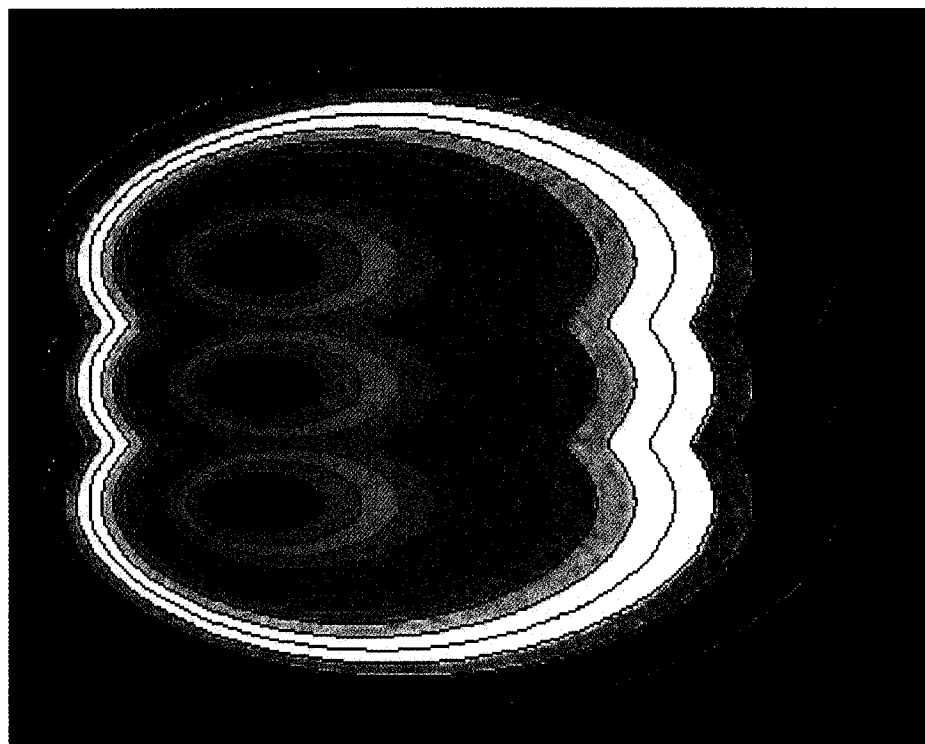
Figure 3-24. CA model fire spread contours considering a fire originating from 3 separate sources. The simulation used a wind angle of 90 degrees and a length-to-breadth ratio of 2.0, for 500 iterations. Spread algorithms easily allow blending of fire spread contours.

Wind direction and speed can also be changed to depict real-time changes in fire

growth. As an example, the baseline elliptical fire in Figure 3-23 was modified to change

the wind direction from westerly (90 degrees) to south-westerly (45 degrees) and to

increase the wind speed by increasing the elliptical length-to-breadth ratio. Additionally,

a solid obstruction such as a structure or water was included to display the spread shapes

as they are influenced in time. These complexities were simulated using the CA model

and the results shown in Figure 3-25.
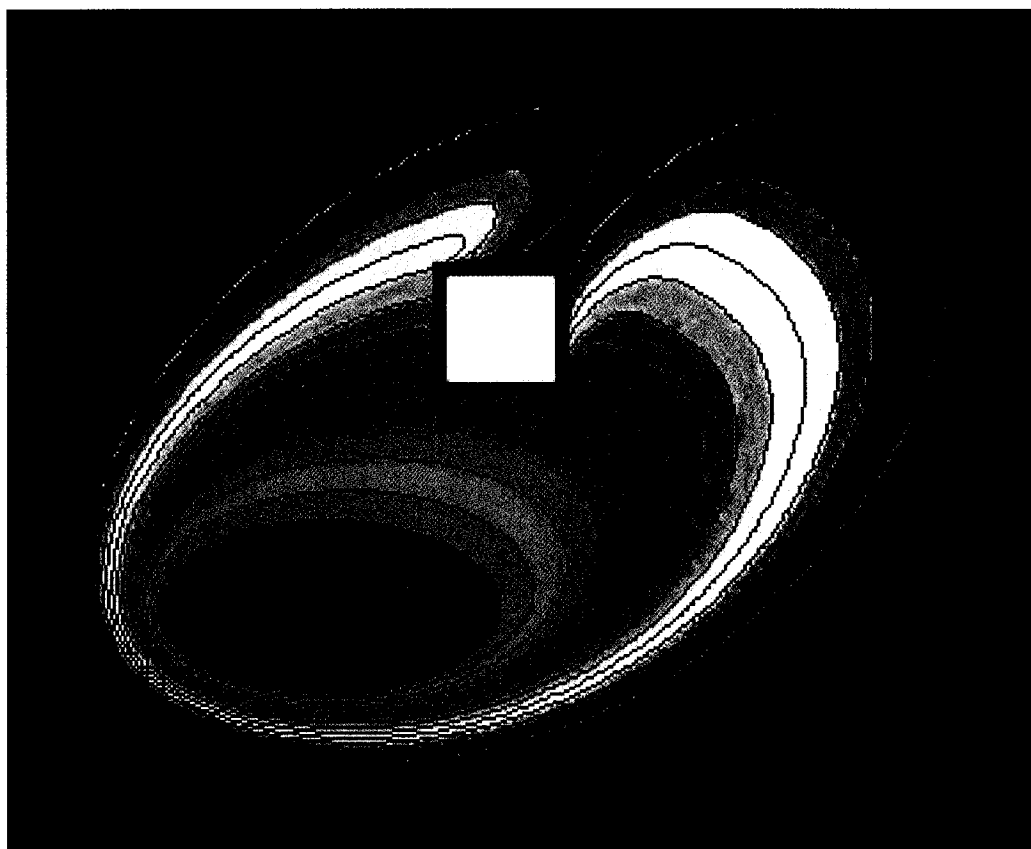
Figure 3-25. CA fire spread contours depicting fire boundary locations with changing
wind speed and direction and a solid obstruction in the spread path. The simulation used
a wind angle of 90 degrees and a length-to-breadth ratio of 2.0, for the first 200 iterations.
The wind angle was changed to 45 degrees and a length-to-breadth ratio of 3.0 for the
next 1000 iterations. CA models can be simply modified for a variety of wind and
surface obstruction conditions.

The formulation of CA weighting factors is a critical result of this research. It has also been shown that various combinations of wind speed and direction can be modeled with this single algorithm. Since the advantage of CA model lies in its simplicity, limiting the algorithm complexity while maintaining accuracy will be a key to proving the notion that this CA approach is an improvement over existing fire modeling approaches. The algorithm has been presented in several parts throughout this chapter. Appendix A contains the entire algorithm in summary format including the required CA model input parameters. Appendix B contains the basic FORTRAN-90 code required to implement the algorithm for any cellular automata fire model. The listed code does not include user-defined inputs, such as pre-burned areas or user-defined outputs such as perimeter output routines. It is expected that future researchers could add these routines for their particular application.

Real Fire Event Comparisons

As a final step, and one that ultimately tests the utility of the CA model, the model results were compared with two separate real fire events. After an extensive literature search, it was determined that there were very few real fire events with sufficient documentation to measure fire propagation boundaries over time. The two selected fire events were the 1996 Bee Fire (Fujioka, 2001) in San Bernardino National Forest, California and the 1967 Sundance Fire (Anderson, 1968) in Idaho.

The Bee Fire occurred in the California San Bernardino National Forest from June 2 to July 3 ,1996. The USDA Forest Service collected fire growth perimeters at several time intervals (Weise and Fujioka, 1998). The fire generally propagated to the northeast (45 degrees according to the directions defined in Figure 3-23) from its starting location at the base of the San Jacinto Mountains. After 3 days of uncontrolled movement, the fire was suppressed and contained within a 3848 ha area. Figure 3-26 shows three measured fire perimeters at 10, 43 and 103 minutes after ignition. Raw perimeter data was obtained directly from Francis Fujioka (Fujioka, 2001) to generate this plot.
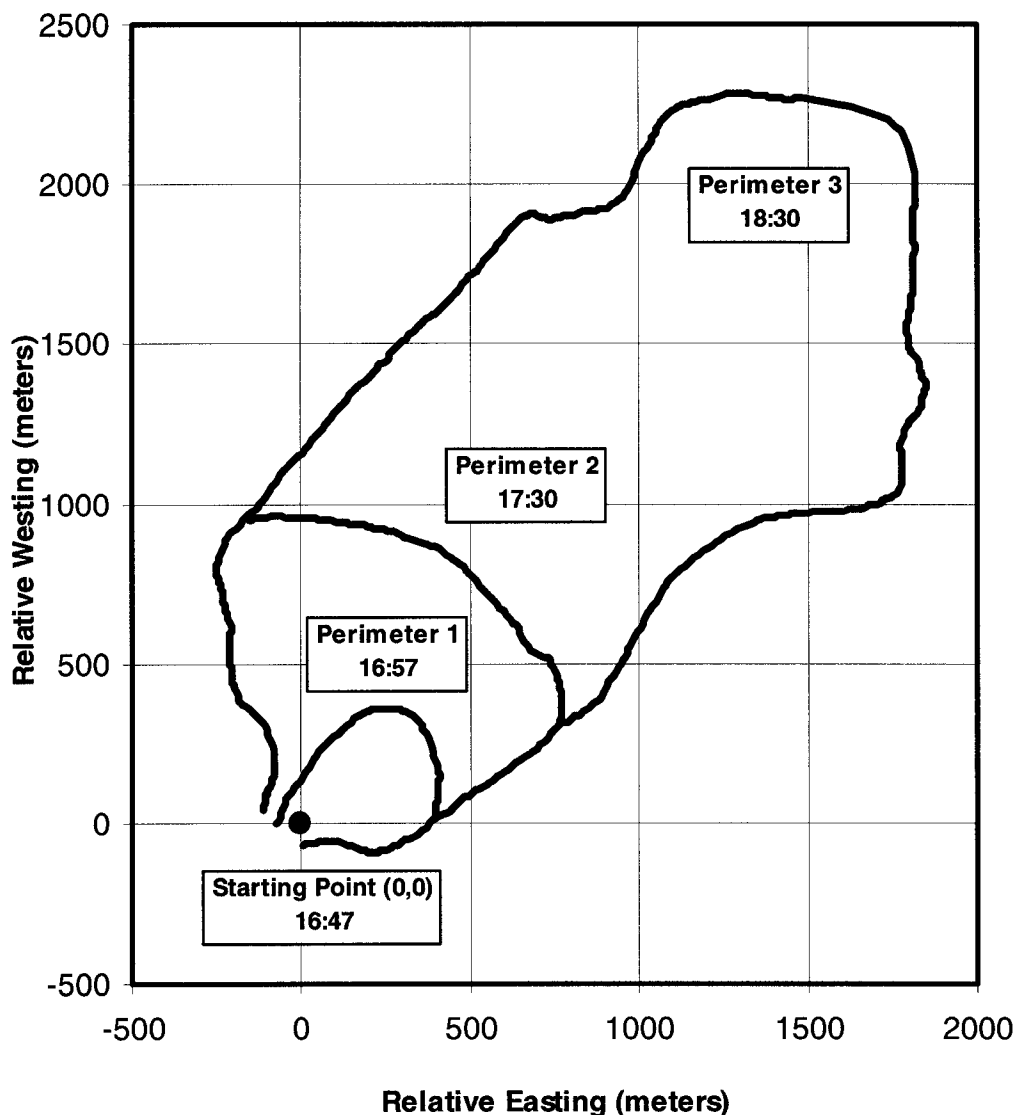
Figure 3-26. Observed fire perimeters from the 1996 Bee Fire. Axis units are in meters, relative to the starting location at the origin point. Southwest winds at approximately 2 m/s resulted in general fire propagation to the northeast.

The fire perimeter measurements were constrained in the backfire direction. This resulted in a lack of data near the ignition point. Perimeter 1 and 3 exhibited near-elliptical spread patterns in the headfire direction that were consistent with the southwest wind. Perimeter 2 exhibited an irregular growth lobe in the northwest corner that can be

partially attributed to a change in wind direction. A mesoscale model predicted winds out of the southeast near 17:00 hours (Fujioka, 2001). This analysis provides evidence of growth toward the northwest that would explain this irregular lobe.

Three CA model cases were compared with actual fire perimeters (Table 3-1). In each case the starting position was determined by the previous known perimeter, which is typical of the intended model application for space. The propagation angle was fixed at 45 degrees and the length-to-breadth ratio was calculated for each specific case. The number of iterations was varied to simulate the intended rate of spread from the known perimeter.

Case	Starting Point	Angle	L/B	Iterations
1	16:47 Origin (0,0)	45.0	2.66	428
2	16:57 Perimeter #1	45.0	2.66	1285
3	17:30 Perimeter #2	45.0	2.41	664

Table 3-1. Cellular automata fire model inputs for the 1996 Bee Fire simulation. Each case was initiated from the previous known fire perimeter, which is consistent with the intended model operation for a space application.

Case 1 was a special case, since it started from a fixed point (origin) and did not have a known perimeter. The measured rate of spread at perimeter 1 was 0.785 m/s and the estimated backfire spread rate was 0.030 m/s. Using equation 3-6, the calculated L/B ratio was 2.66. In order to achieve the appropriate spread rate at 45 degrees propagation angle, 428 iterations were required. Figure 3-27 shows the observed (solid black) and predicted (dotted red) perimeters based on these biased model parameters. Since this case started from a point versus an actual known perimeter, it does not truly

reflect the intended application for space. Conversely, the elliptical shape pattern does reflect the growth of the actual fire quite closely for most of the perimeter. The only area of poor correlation is the southeast lobe of the perimeter.
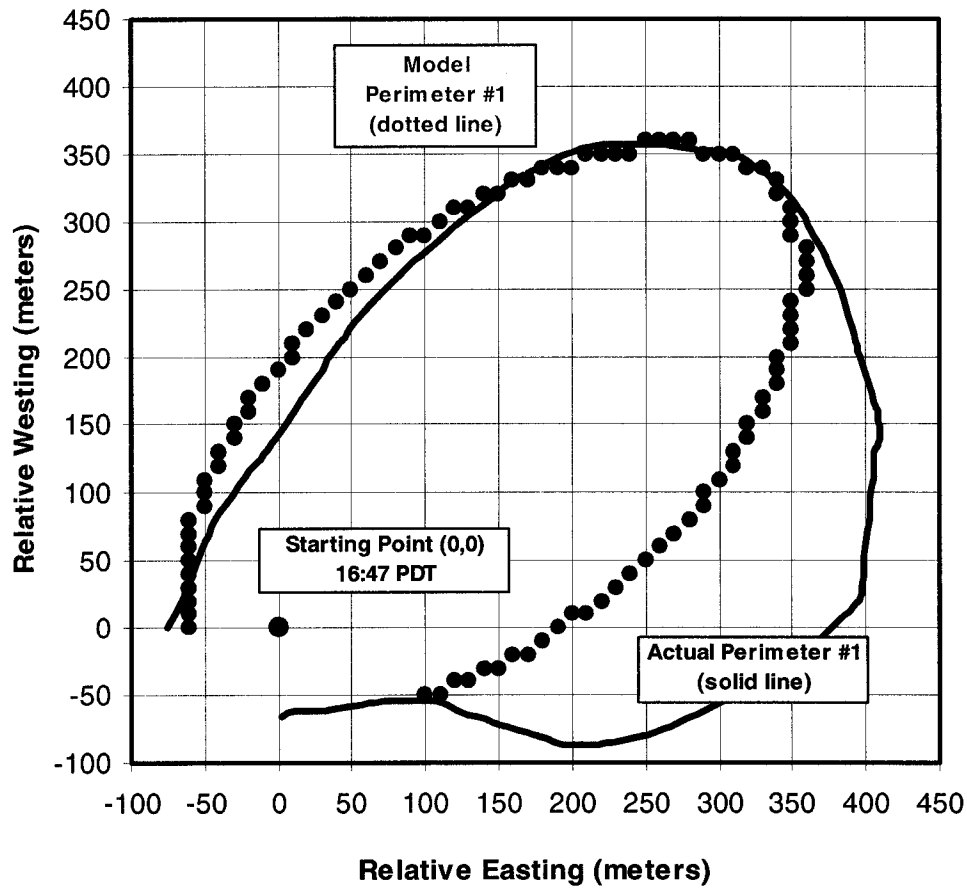
Figure 3-27. Observed and predicted fire perimeters originating from a single starting point for the 1996 Bee Fire. Axis units are in meters relative to the starting location. Cellular automata model predictions correlated well with observed perimeters for much of the fire perimeter.

Case 2 is more typical of the intended application of the propagation model, since

it starts at a known fire perimeter with measurable spread rates. The measured

propagation angle was consistent with the known wind direction of 45 degrees. As in

case 1, the L/B ratio was 2.66, based on measured headfire and backfire velocities. The

number of iterations was increased to 1285 to accommodate for the increased time (33

minutes) between perimeter 1 and 2. Figure 3-28 shows the results for case 2.
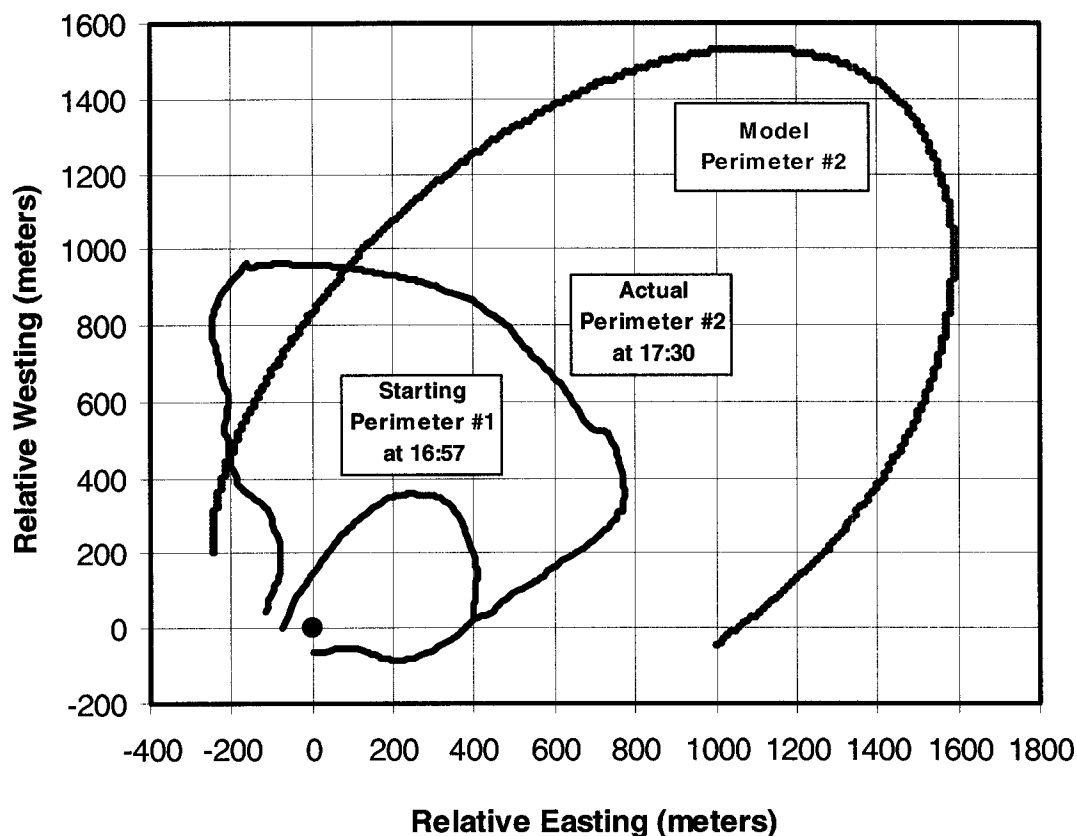
Figure 3-28. Observed and predicted fire perimeters originating from perimeter #1 for
the 1996 Bee Fire. Axis units are in meters relative to the starting location. Cellular
automata model predictions overpredicted the observed perimeter due to a decreasing
spread rate during the long time interval between measurements.

It is obvious from Figure 3-28, that the fire was changing rapidly over the 33 minute period between perimeter 1 and 2. The large errors in predicted perimeter locations can be attributed to the decreased rate of spread. With more frequent data acquisition it is likely the errors would be significantly reduced. Figure 3-29 shows the actual measured rate of spread over the time of the fire. The reduced rate of spread prior to the measurement of perimeter 1 caused on overprediction of the fire perimeter.
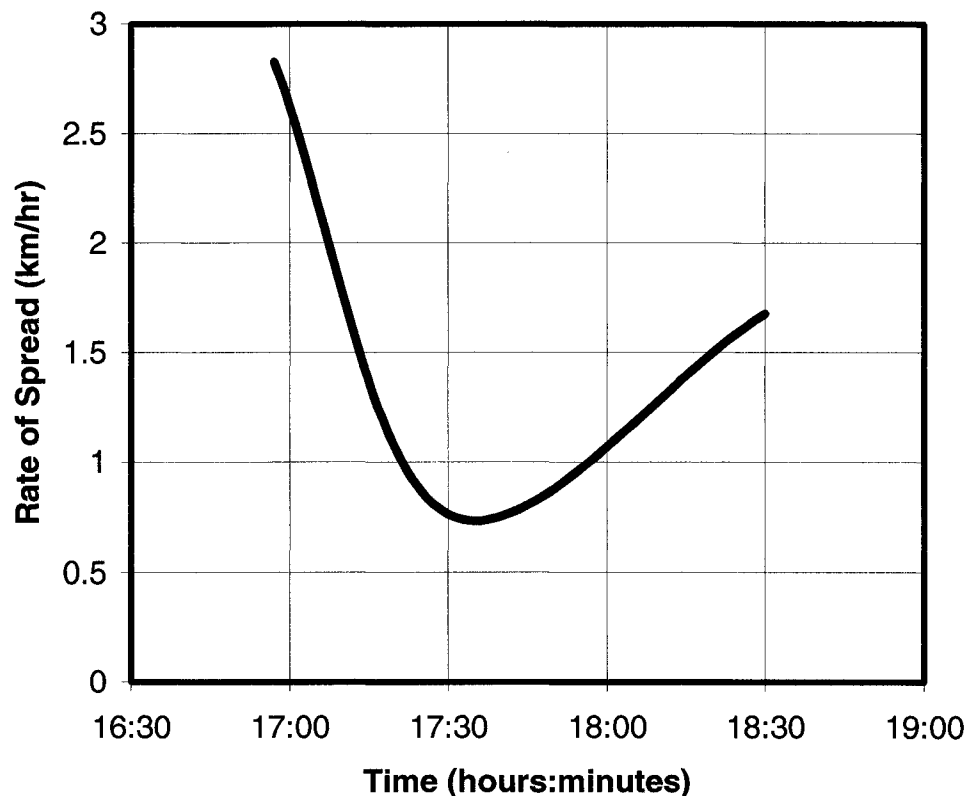
Figure 3-29. Observed rate of spread for the 1996 Bee Fire. Errors in model predictions can be largely attributed to the significant changes in rate of spread over the life of the fire.

Case 3 was run similar to case 2. A propagation direction of 45 degrees was selected to reflect the first measured perimeter and to be consistent with the known wind direction. Selecting a propagation angle solely based on perimeter 2 data would have skewed the results toward the northwest. Had more data been available, it is likely the measured direction would have neared 45 degrees. An analysis of perimeter 2 revealed a lower headfire spread rate (0.212 m/s) and lower backfire spread rate (0.010 m/s) that resulted in nearly the same L/B ratio (2.41). Similar to case 2, the number of iterations was based on the desired spread rate for the intended time period. Figure 3-30 shows the results for case 3.
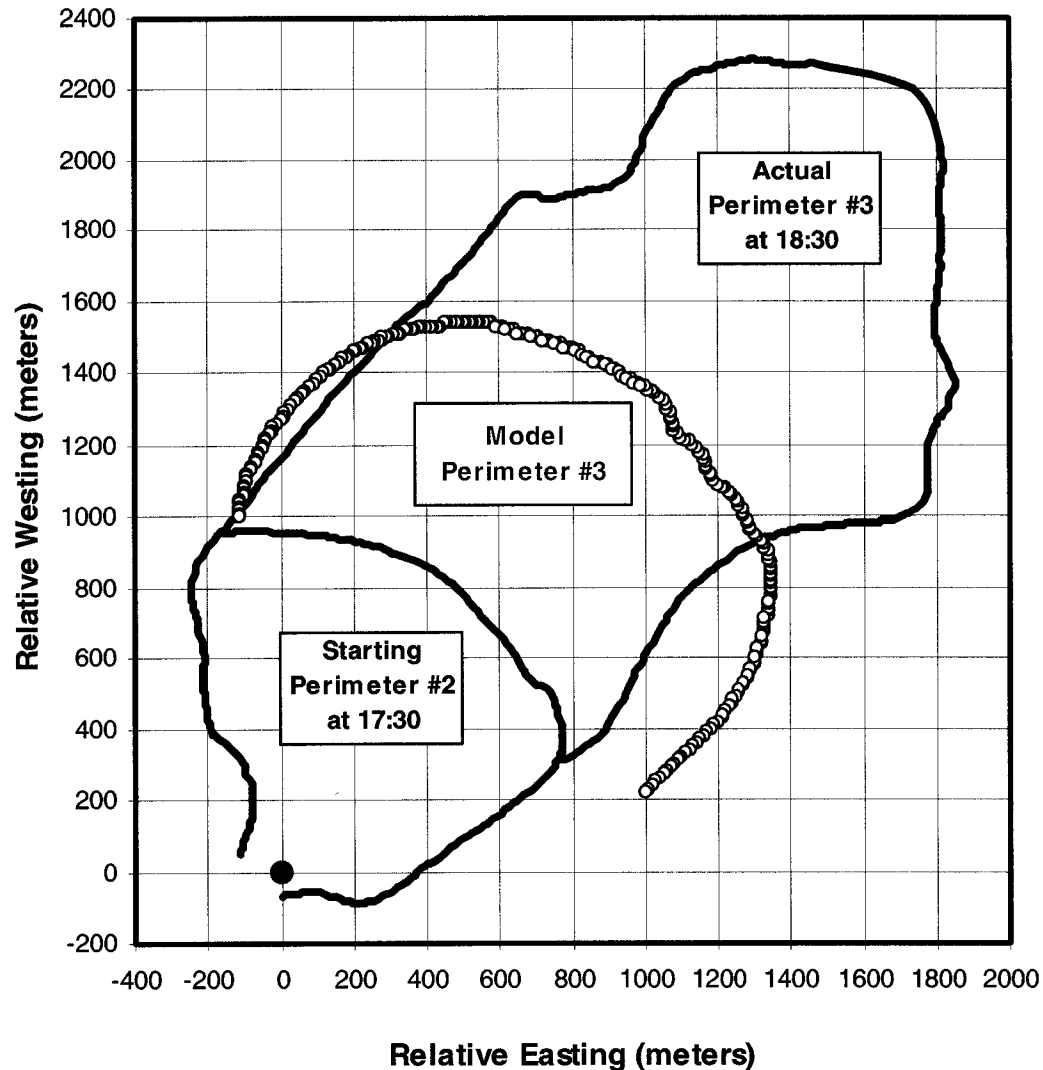
Figure 3-30. Observed and predicted fire perimeters originating from perimeter #2 for the 1996 Bee Fire. Axis units are in meters relative to the starting location. Cellular automata model predictions underpredicted the observed perimeter due to an increasing spread rate during the long time interval between measurements.

A summary of the results from all 3 cases is shown in Figure 3-31. The ratio of the observed to predicted perimeter radius is shown as a function of direction angle measured from the starting point. Though these simulations produced large errors for cases 2 and 3, the results were comparable to errors reported by Fujioka (2001) in his simulations using the FARSITE (Finney, 1998) partial differential equation code.

Reported perimeter errors varied from 0.6 to 2.6 in the cases analyzed by Fujioka. Aside

from the intermittent data acquisition, it is also likely that the light winds (near 2 m/s)

would allow minor perturbations in spread direction as local wind bursts could influence

the behavior.
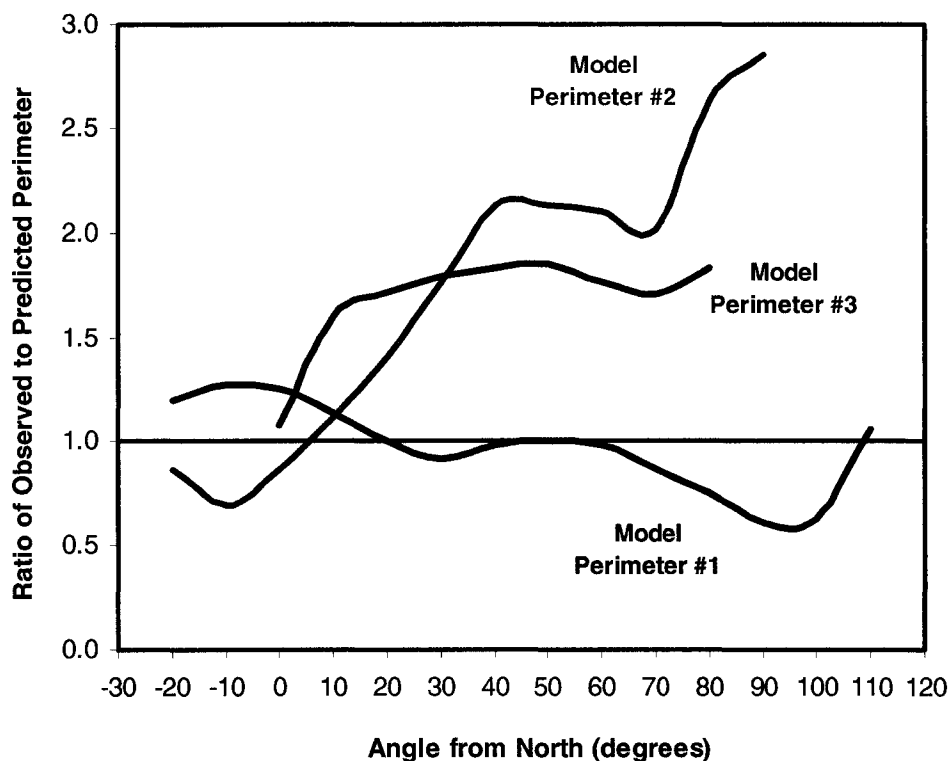
Figure 3-31. Ratio of observed to predicted perimeter radius versus direction angle for the 1996 Bee Fire simulation. Cellular automata predictions produced large errors in some directions. These errors were consistent with those reported by Fujioka (2001) using FARSITE (Finney, 1998).

A second set of simulations were compared to the 1967 Sundance Fire in northern

Idaho (Anderson, 1968). This rapidly moving fire originated near Sundance Mountain

and burned an area over 20,000 ha. On September 1, 1967, the fire traveled 16 miles in a

period of 9 hours. The Northern Forest Fire Laboratory was assigned to investigate the

physical phenomena of the fire and document historical development. Fire front

locations were determined by a combination of actual field measurements and personal interviews from multiple sources. The variance in data sources slightly diminished the credibility of the actual fire front, but its general path and shape were constructed with reasonable success. Figure 3-32 shows the constructed fire perimeters at 6 different time intervals in relation to the estimated starting location at the origin of the graph. These perimeters were digitized from fire perimeter plots in Anderson (1968). It is apparent from the figure that the fire perimeters exhibited elongated elliptical shapes typical of rapidly moving wind-driven fires.
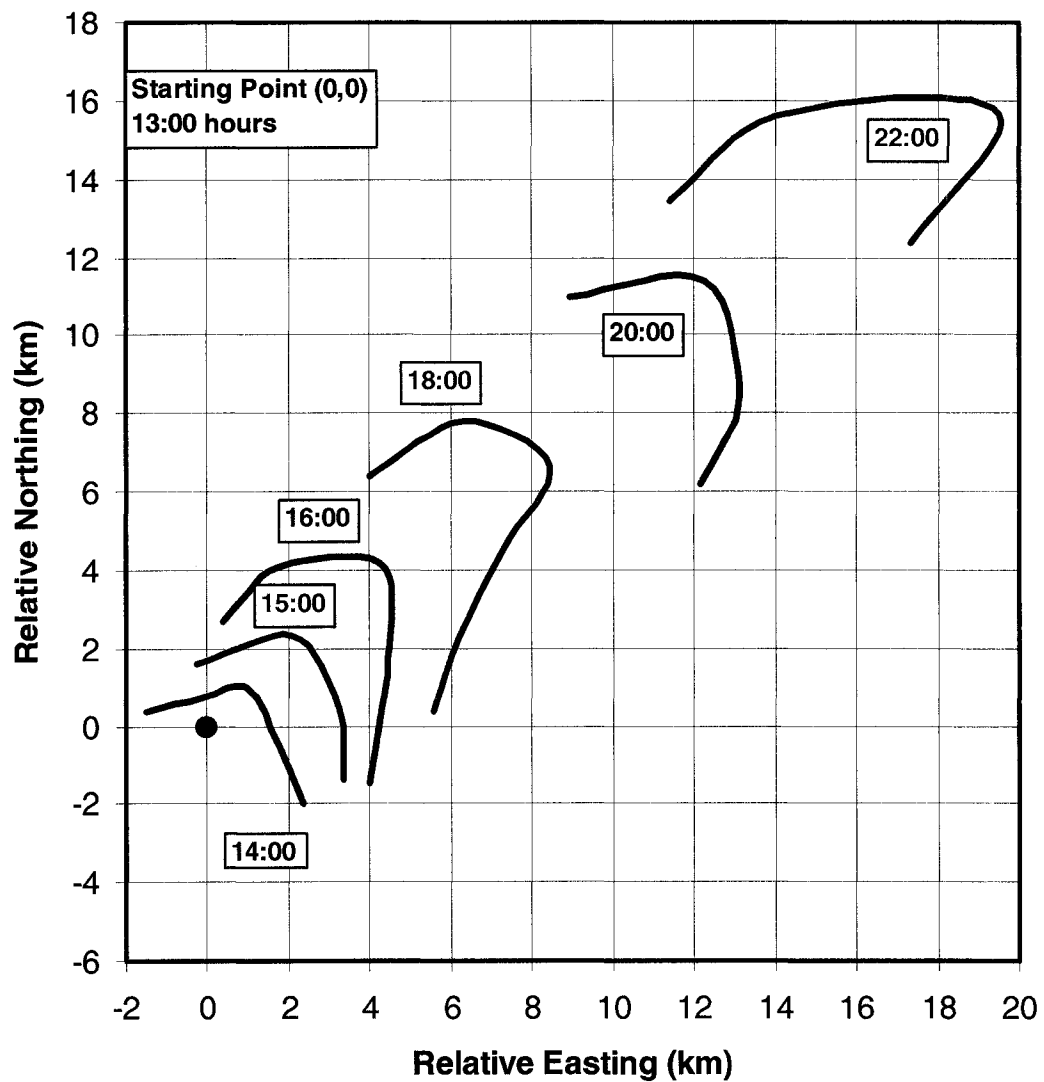
Figure 3-32. Observed fire perimeters from the 1967 Sundance Fire. Axis units are in meters, relative to the starting location at the origin point. Southwest winds resulted in general fire propagation to the northeast.

The measured winds during the Sundance Fire were recorded at regular intervals (Figure 3-33). In all but one measurement, the wind direction was southwesterly, with the lone anomaly exhibiting west-southwesterly wind. Over the course of the fire, wind speed steadily increased from approximately 34 to 71 km/hr.
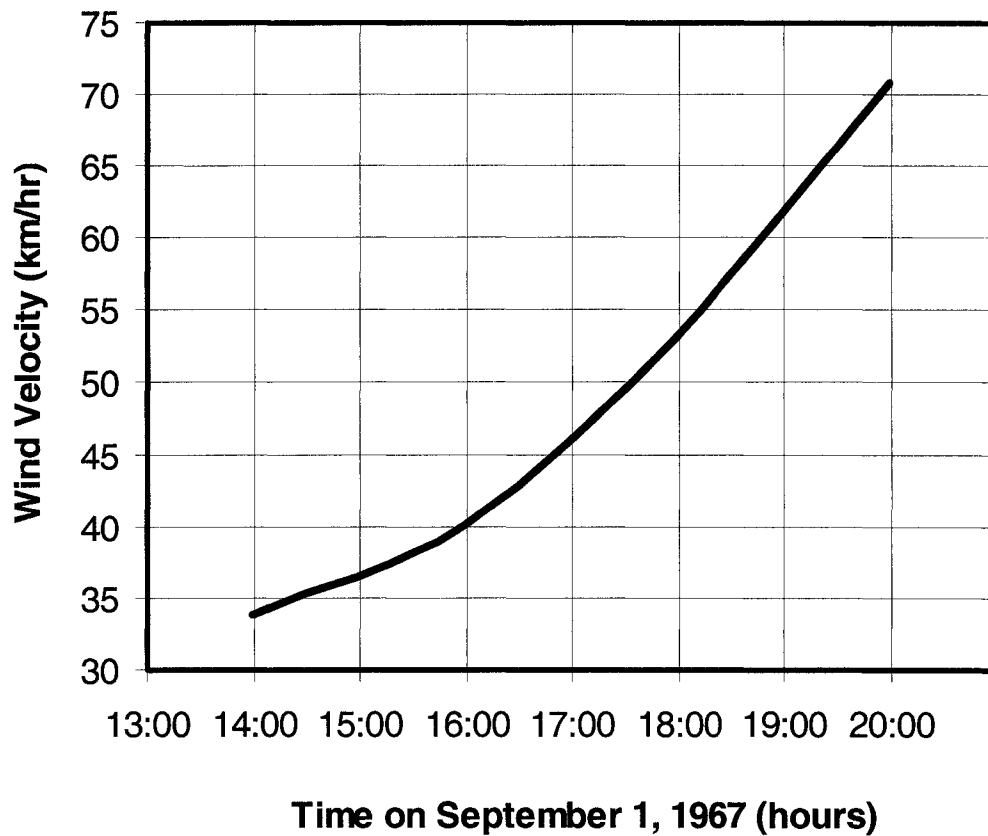
Figure 3-33. Measured wind velocity (km/hr) as a function of time during the Sundance Fire. A steady increase in wind speed resulted in increased rate of spread and elliptical spread shapes with more eccentricity, or a higher length to breadth ratio.

Five CA model cases were compared with actual fire perimeters (Table 3-2) such that each CA model cell was 24.8 meters wide. In each case the starting position and propagation direction were determined from the previous known perimeter. Length-to-breadth ratio was calculated similar to the previous simulation using equation 3-6. The backing fire rate of spread was fixed at 0.088 km/hr based on perimeter data from the 18:00 time sample. This was the only backfire perimeter data available for determining backfire spread rate. The number of iterations were determined by the required fire rate of spread for each starting fire perimeter and the scaling factor in the CA algorithm. These assumptions were used to simulate fire propagation for comparison with the measured fire perimeter at the next time interval. The results from these five CA model cases are shown in Figures 3-34 through Figure 3-38.

Case	Starting Point	Angle	L/B	Iterations
1	14:00 Perimeter #1	45.0	2.12	367
2	15:00 Perimeter #2	50.7	2.35	500
3	16:00 Perimeter #3	41.4	2.91	1090
4	18:00 Perimeter #4	30.5	2.71	1399
5	20:00 Perimeter #5	50.8	3.01	2818

Table 3-2. Cellular automata fire model inputs for the 1967 Sundance Fire simulation. Each case was initiated from the previous known fire perimeter, which is consistent with the intended model operation for a space application.
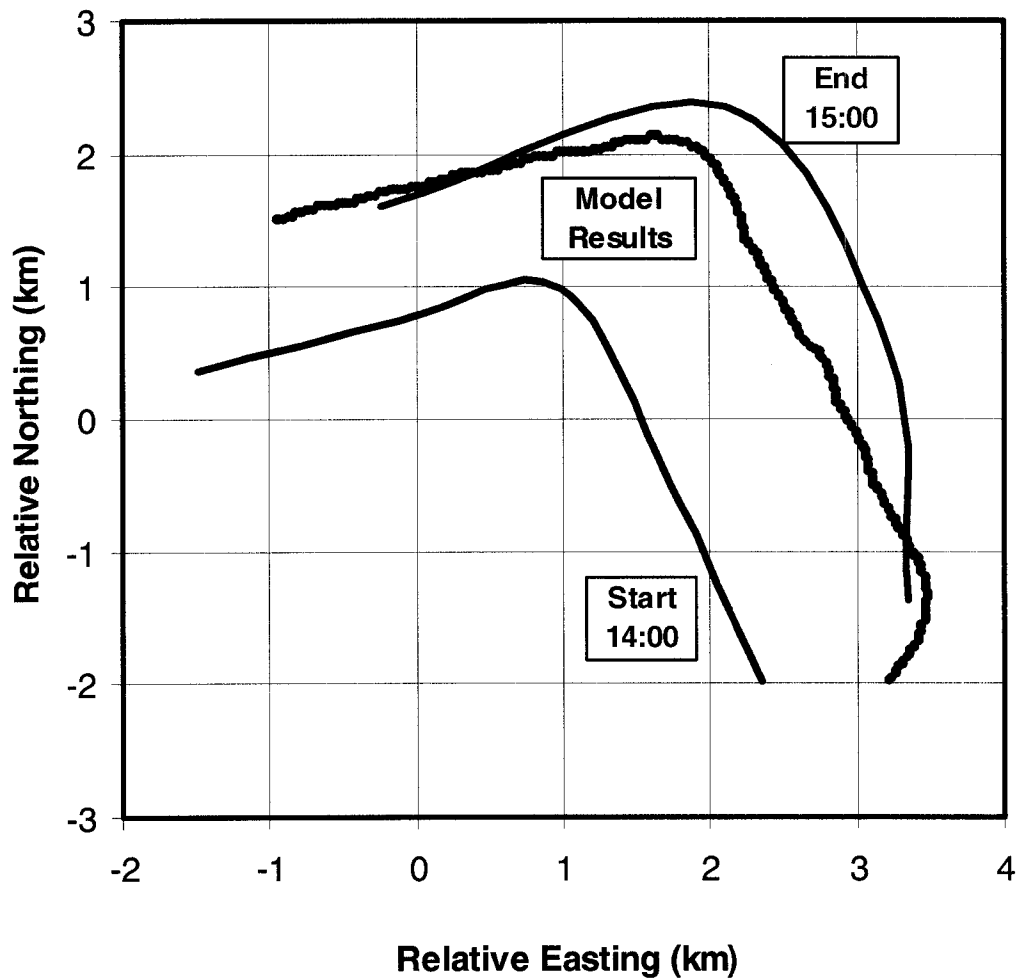
Figure 3-34. Observed and predicted fire perimeters for the 1967 Sundance Fire originating from the known perimeter at 14:00. Axis units are in kilometers relative to the starting location. Cellular automata model predictions correlated well with the observed perimeter with only slight underpredictions in the northeast quadrant.
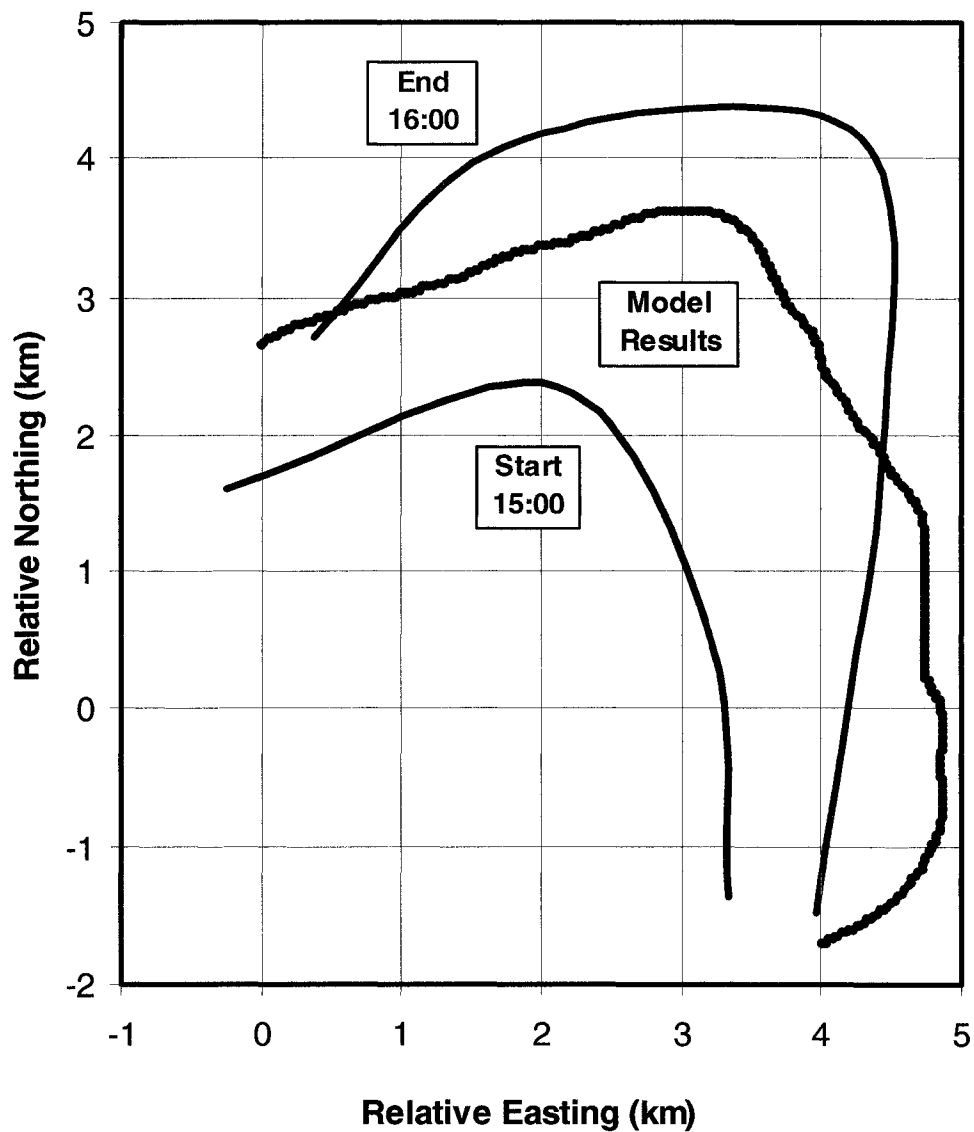
Figure 3-35. Observed and predicted fire perimeters for the 1967 Sundance Fire originating from the known perimeter at 15:00. Axis units are in kilometers relative to the starting location. Cellular automata model predictions correlated reasonably well with the observed perimeter with only slight underpredictions in the northeast quadrant.
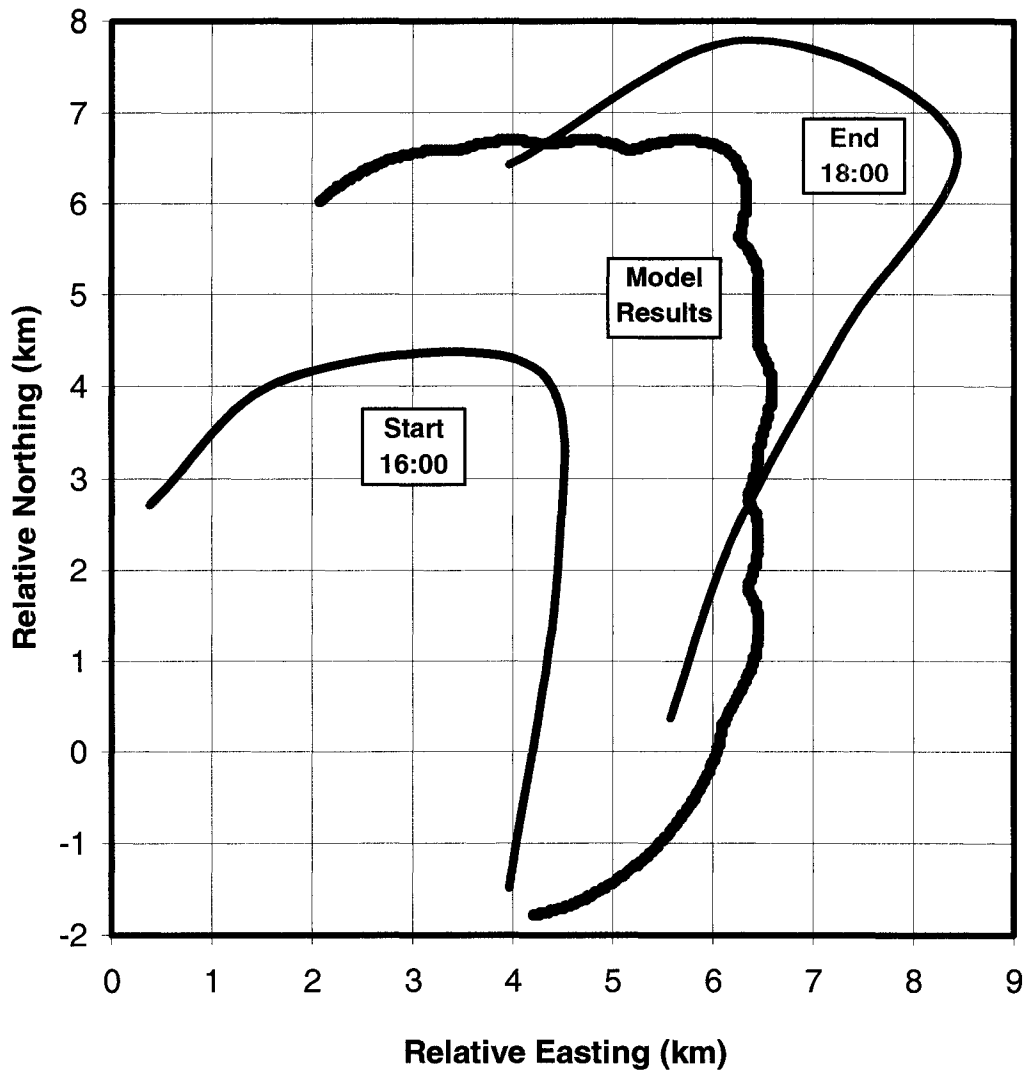
Figure 3-36. Observed and predicted fire perimeters for the 1967 Sundance Fire originating from the known perimeter at 16:00. Axis units are in kilometers relative to the starting location. Cellular automata model predictions correlated reasonably well with the observed perimeter with only slight underpredictions in the northeast quadrant.
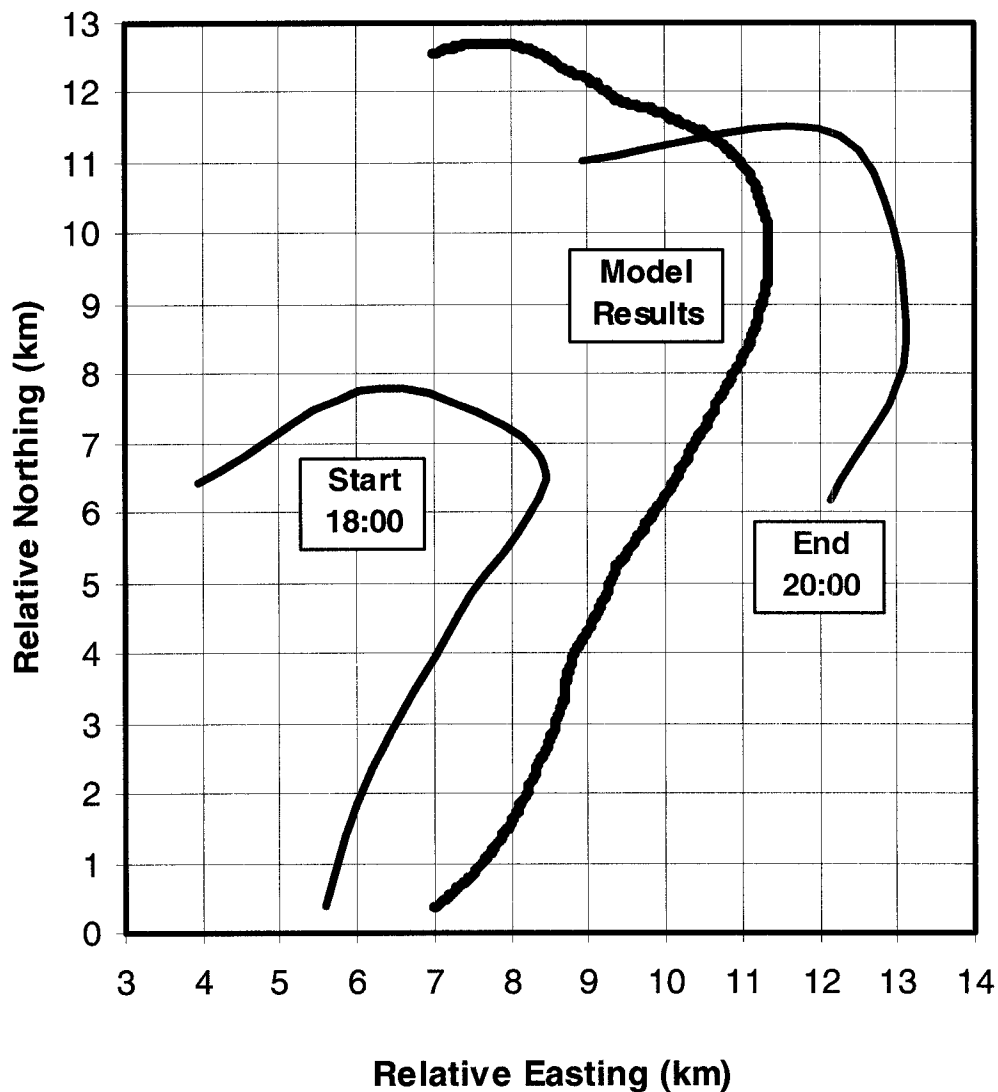
Figure 3-37. Observed and predicted fire perimeters for the 1967 Sundance Fire originating from the known perimeter at 18:00. Axis units are in kilometers relative to the starting location. Cellular automata model predictions correlated reasonably well with the observed perimeter with only slight underpredictions in the northeast quadrant.
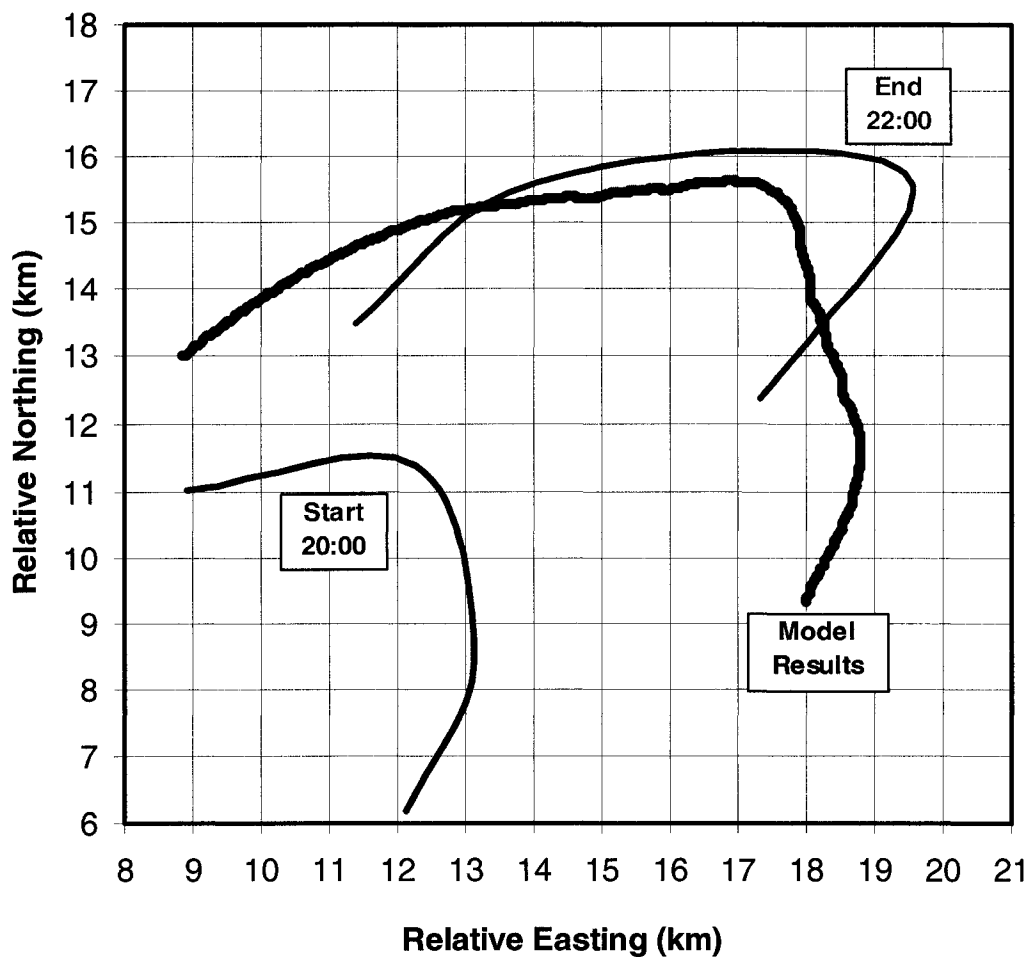
Figure 3-38. Observed and predicted fire perimeters for the 1967 Sundance Fire originating from the known perimeter at 20:00. Axis units are in kilometers relative to the starting location. Cellular automata model predictions correlated reasonably well with the observed perimeter with only slight underpredictions in the northeast quadrant.

All of the results from the 5 cases are shown in Figure 3-39. The ratio of the observed to predicted fire perimeter radius is shown as a function of direction angle. The average error of the observed to predicted perimeter length was 12%, for all cases. This is a reasonable correlation considering several factors. As shown in Figure 3-33, wind velocity steadily increased over the course of the fire, so slight underprediction of the headfire front was expected. Furthermore, the time separation between perimeters was one or two hours. In case 5, the actual perimeter traveled nearly 9 km over 2 hours. It is likely that predicted perimeters at smaller time intervals, such as 30 minutes or one hour, would have improved correlation errors.
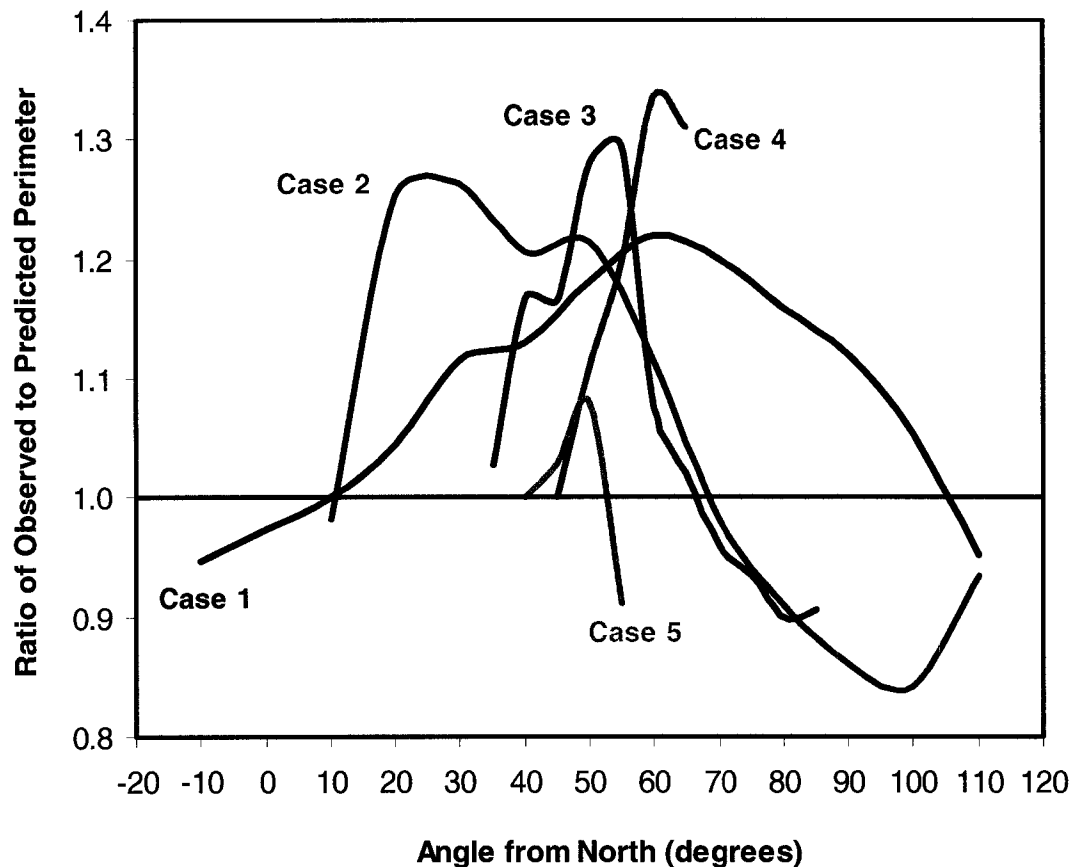
Figure 3-39. Ratio of observed to predicted perimeter radius versus direction angle for the 1967 Sundance Fire simulation. Cellular automata predictions underpredicted the actual fire perimeters by an average of 12%. Errors were highest in the primary headfire direction due to steadily increasing wind speed.

All of the reported simulations were conducted on a 1.6 GHz Pentium-4 PC. The computational time for an entire scene is relatively short and could likely be improved with optimization of the computer coding. As an example, a 1000 by 1000 grid required 206 seconds of actual clock time to complete 1000 iterations. Other variations of grid size and iteration quantity scaled as expected. In a typical space application, it would be possible to measure a fire perimeter, conduct a CA simulation for a 1000 by 1000 scene and repeat the process every few minutes. Real-time data could be transferred to the

ground on these same time intervals creating a functional data product for fire management.

   This chapter has presented a cellular automata fire propagation model suitable for space applications and wildfire management. Algorithms were developed using a coupled map lattice for a Moore neighborhood cellular structure. Weighting parameters for cell-state equations were determined for various elliptical eccentricities to minimize shape distortion below 2%. The presented algorithm was tested against two real fire events with favorable results. Simulations were conducted using known fire perimeter data without wind or fuel data. This is vastly different from existing fire propagation models which require highly variable and often undermeasured parameters. The presented simulations require minimal computational complexity and have the potential to provide a functional data product for future fire management.

Future Research

NASA Langley Research Center continues to pursue fire research and the development of a dedicated space-borne fire monitoring system. Up to this point, scientific support has been excellent, but funding approval for significant advancement has been insufficient. Priorities for Earth Science research have focused on climate modeling and atmospheric chemistry, with the study of fire as a secondary benefit gained from existing instrumentation. A full mission dedicated to fire research will require substantial technology development and demonstration of key operational and scientific concepts. Only at this point will the scientific and budget constraints reach an acceptable level to make this mission a reality. With this said, it is not only likely, but inevitable, that a dedicated fire mission will be part of our future.

Prior to this reality, it is possible to plan for a series of scaled tests and demonstrations. Once a functional fire detector system is developed, its performance can be evaluated using ground-based tests, balloons, manned aircrafts, or Unmanned Aerial Vehicles (UAV's). Even a "piggy back" mission in Low Earth Orbit (LEO) will be a cost savings over a geosynchronous mission. Many issues associated with saturation temperature, sampling methods, and general engineering design trades can be evaluated with these tests. In addition to the detector performance, it will be possible to perform early testing of fire propagation algorithms in controlled conditions with known spread conditions. Correlation with existing fire codes will be important to demonstrate the

flexibility and simplicity of the new algorithms. An extension of the algorithms to include Geographical Information System (GIS) data could certainly improve accuracy. The baseline grid-based scene could include known obstructions, terrain slope, and other pertinent data that could influence the fire spread weighting algorithms.

Ultimately the future of this research relies on the ability to measure the existence of fire, predict its movement and communicate that information to those fire managers and scientists with a desire for the information. With further improvements in communication and computer technology it may be possible to develop automated optimization algorithms that direct the available fire fighting resources in near real time. This will likely save lives and property, thereby achieving the ultimate goal of scientific research.

Conclusions

This research was motivated by the need for improved wildfire monitoring to complement existing fire management and ultimately reduce the loss of property and human life. An effective space-borne monitoring system will allow near real-time tracking of fire boundaries and the post-fire assessment of biomass burning emissions on our climate. Fire front location and intensity data can be used in propagation models to predict future frontal locations. Trace gas emissions from active fire fronts can be determined from measurements of fire temperature over time. Existing wildfire monitoring systems depend on aircraft or ground data with sparse temporal and spatial sampling. A space-borne satellite, detector system and propagation model can provide the foundation for the next generation of fire science. Such a system would be superior to standard methods with the potential to significantly contribute to future fire research and benefit the general public.

The geosynchronous satellite system uses a nutating detector array to yield a spatial resolution of 100 meters per pixel with a repeatable coverage rate approaching one minute. Careful selection of detector operating temperature, saturation temperature, signal charge capacity and integration time allows optimization of signal to noise performance. Radiation modeling was used to verify the selection of 3.7 μm for active fire detection and 10.2 μm for background ground temperatures. A temperature inversion technique utilizing both detector channels allows sub-pixel resolution of the scene.

Radiation attenuation due to clouds and aerosols was evaluated to define the limitations and capabilities of the detector system. Fire detection through thin cirrus clouds and intense smoke layers is possible. A survey of state-of-the-art detector capabilities and an assessment of active fire tests suggest the presented system is viable for active fire detection from space.

A coupled map lattice discrete cellular automata model was developed to predict wildfire propagation based on semi-empirical fire perimeters measured from a space-borne detector system. Cell state algorithms for an 8-cell neighborhood correlated within 2% of theoretical circular and elliptical spread shapes. Variations in wind speed and direction are accommodated in the cell weighting algorithms. The simplicity and efficiency of the model is an improvement over existing spread models based on partial differential equations. Simulations of the 1996 Bee Fire and the 1967 Sundance Fire suggest reasonable correlation of actual fire perimeters with accuracies near those of existing propagation models. Improved temporal sampling of perimeter data would likely improve correlation. These simulations require active fire perimeter locations and eliminate the need for insufficient wind and fuel data. The potential for a functional fire data product for the fire management community is certainly possible.

APPENDIX A: CELLULAR AUTOMATA ALGORITHM SUMMARY

Cellular Automata Local Rule:

$$S_{i,j}^{t+1} = \min \left[1.0, \quad S_{i,j}^t + R \cdot \begin{bmatrix} (W_7(\beta) * S_{i-1,j}^t + W_1(\beta) * S_{i,j+1}^t + \\ W_3(\beta) * S_{i+1,j}^t + W_5(\beta) * S_{i,j-1}^t) + \\ D_o \cdot (W_8(\beta) * S_{i-1,j+1}^t + W_2(\beta) * S_{i+1,j+1}^t + \\ W_4(\beta) * S_{i+1,j-1}^t + W_6(\beta) * S_{i-1,j-1}^t) \end{bmatrix} \right]$$

Constants:

V_H = Headfire Velocity V_B = Backfire Velocity

$$D_o = \frac{\sqrt{2}-1}{2} \approx 0.207 \quad R = 0.10 \quad \beta = \frac{\dfrac{V_H}{V_B}+1}{2\sqrt{\dfrac{V_H}{V_B}}}$$

Weighting Parameters:

$$W_1 = 1.0 \qquad 1 \le \beta \le 7$$

$$W_7 = W_3 = \begin{cases} e^{-3.52(\beta-1.0)} & 1 \le \beta \le 3 \\ 0.4e^{-0.88\beta} & 3 < \beta \le 7 \end{cases} \qquad W_4 = W_6 = \begin{cases} e^{-2.14(\beta-1.0)} & 1 \le \beta \le 3 \\ 0 & 3 < \beta \le 7 \end{cases}$$

$$W_8 = W_2 = \begin{cases} e^{-1.29(\beta-1.0)} & 1 \le \beta \le 3 \\ 0 & 3 < \beta \le 7 \end{cases} \qquad W_5 = \begin{cases} e^{-2.16(\beta-1.0)} & 1 \le \beta \le 3 \\ 1.44e^{-0.65\beta} & 3 < \beta \le 7 \end{cases}$$

Wind Direction Function:

$$W_X(\alpha) = \frac{\left[W_{X-S+8}(ref) \cdot \left[1 + \dfrac{\alpha}{45^\circ} - S \right] + W_{X-S+9}(ref) \cdot \left[S - \dfrac{\alpha}{45^\circ} \right] \right]}{45}$$

Wind Direction Angle (α)
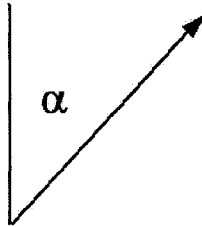
Wind Sectors (S)
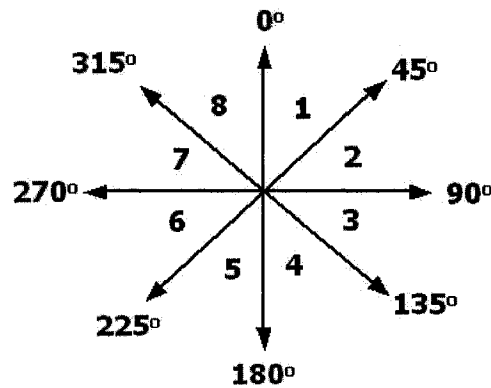
APPENDIX B: CELLULAR AUTOMATA FORTRAN-90 CODE

```fortran
****************************************************************
        Program MAIN
        INTEGER  I,J,DIMX,DIMY,LOOP,TEND,X,SEC2
        INTEGER  STARTX,STARTY
        REAL FAC,BETA,RFAC,WIND,SEC1
        REAL, DIMENSION(3000,3000) :: A,B,C,FX,FY
        REAL, DIMENSION(100) :: W,WNEW
        INTEGER, DIMENSION(3000) :: SUB1,SUB2
        OPEN(Unit=2,File='output.dat')
****************************************************************
* Define parameters
*
*       A = Final Matrix Values (after time step)
*       B = Initial Matrix Values (before time step)
*       C = Perimeter Contour Matrix
*       FX = Perimeter X-Coordinates
*       FY = Perimeter Y-Coordinates
*       DIMX = Lattice X-Dimension (meters)
*       DIMY = Lattice Y-Dimension (meters)
*       STARTX = Cell Starting X-Coordinate
*       STARTY = Cell Starting Y-Coordinate
*       w1 = North wind weighting
*       w2 = NE wind weighting
*       w3 = East wind weighting
*       w4 = SE wind weighting
*       w5 = South wind weighting
*       w6 = SW wind weighting
*       w7 = West wind weighting
*       w8 = NW wind weighting
*       WIND = True wind direction (CW from North=0.0 deg)
*       BETA = Length to Breadth Ratio
*       RFAC = ROS Factor (constant at 0.10)
*       TEND = Number of Iterations
****************************************************************
*       Input Parameters
*
        WIND = 90.0
        BETA = 2.00
        RFAC = 0.1
```

```
        TEND = 500
****************************************************
*       Cell Dimensions and Iterations
*
        DIMX = 1000
        DIMY = 1000
        STARTX = 500
        STARTY = 500
****************************************************
*       Matrix Initialization
*       Burn Fraction = 0
*       A = Current Time Step
*       B = Previous Time Step
*
        DO 80 I=1,DIMX
        DO 81 J=1,DIMY
            A(I,J)=0.0
            B(I,J)=0.0
            C(I,J)=0.0
  81    CONTINUE
  80    CONTINUE
*
*       Define Pre-Burned Areas
*
        B(STARTX,STARTY)=1.0
*
*********************************************
*       Calculate Weighting Algorithms
*
        W(1) = 1.0
*
        IF (BETA.LT.3.01) THEN
        W(4) = EXP(-2.14*(BETA-1.0))
        ELSE
        W(4) = 0.0
        ENDIF
*
        IF (BETA.LT.3.01) THEN
        W(5) = EXP(-2.16*(BETA-1.0))
        ELSE
        W(5) = 1.44*EXP(-0.65*BETA)
        ENDIF
*
        IF (BETA.LT.3.01) THEN
        W(8) = EXP(-1.29*(BETA-1.0))
        ELSE
        W(8) = 0.0
```

```
        ENDIF
*

        IF (BETA.LT.3.01) THEN
        W(7) = EXP(-3.52*(BETA-1.0))
        ELSE
        W(7) = 0.40*EXP(-0.88*BETA)
        ENDIF
*

        w(3)=w(7)
        w(2)=w(8)
        w(6)=w(4)
*******************************************************
*       Calculate Wind Direction Adjustments
*

        SEC1 = WIND / 45.0
        SEC2 = INT(SEC1)
*

        DO 130 X=1,8
            SUB1(X)=X-1-SEC2+8
        IF ((X-1-SEC2+8).GT.8.0) THEN
            SUB1(X)=X-1-SEC2
        ENDIF
            SUB2(X)=SUB1(X)+1
        IF ((SUB2(X)).GT.8.0) THEN
            SUB2(X)=SUB2(X)-8
        ENDIF
            WNEW(X)=W(SUB1(X))*(SEC1-SEC2)+W(SUB2(X))*(1-
SEC1+SEC2)
 130    CONTINUE
*

*******************************************************
*       General CA Local Rule
*

        DO 51 LOOP=1,TEND
        DO 82 I=1,DIMX
        DO 83 J=1,DIMY
                A(i,j)=B(i,j)+RFAC*((WNEW(3)*B(i-1,j)+
        >       WNEW(1)*B(i,j-1)+WNEW(5)*B(i,j+1)+
        >       WNEW(7)*B(i+1,j))+ 0.2071 *(WNEW(2)*B(i-1,j-
1)+
        >       WNEW(4)*B(i-1,j+1)+WNEW(8)*B(i+1,j-1)+
        >       WNEW(6)*B(i+1,j+1)))
 21     IF (A(i,j).GT.1.0) THEN
            A(i,j)=1.0
        END IF
 83     CONTINUE
 82     CONTINUE
```

```
*
        DO 85 I=1,DIMX
        DO 86 J=1,DIMY
           B(I,J)=A(I,J)
 86     CONTINUE
 85     CONTINUE
*
        FAC=LOOP*1.0
        DO 87 J=1,DIMY
        DO 88 I=1,DIMX
        IF ((B(i,j).GT.(0.999)).AND.
     >     (C(i,j).EQ.(0.0))) THEN
              C(i,j)=FAC
        ENDIF
 88     CONTINUE
 87     CONTINUE
************************************************************
 51     CONTINUE
************************************************************
*       Calculate Fire Perimeter Coordinates
*
        DO 92 J=1,DIMY
        DO 93 I=1,DIMX
           FX(I,J)=0.0
         , FY(I,J)=0.0
        IF (    (C(I,J).GT.(0.999)).AND.
     >     (    (C(I-1,J).EQ.(0.0)).OR.
     >          (C(I,J-1).EQ.(0.0)).OR.
     >          (C(I+1,J).EQ.(0.0)).OR.
     >          (C(I,J+1).EQ.(0.0)) )    )
     >THEN
           FX(I,J)=I
           FY(I,J)=J
        ENDIF
 93     CONTINUE
 92     CONTINUE
************************************************************
*       Write Perimeter
        DO 33 J=DIMY,1,-1
        WRITE(2,45) (C(i,j),i=1,DIMX)
 33     CONTINUE
 45     FORMAT(1x,100F7.2)
*
        WRITE(2,*)
        DO 152 J=1,DIMY
        DO 153 I=1,DIMX
        IF (    (FX(I,J).GT.(0.001))  .OR.
```

```
>          (FX(I,J).LT.(-0.001))  .OR.
>          (FY(I,J).GT.(0.001))  .OR.
>          (FY(I,J).LT.(-0.001))        )
>THEN
     FX(I,J)=(I-STARTX)
     FY(I,J)=(J-STARTY)
  WRITE(2,154) FX(I,J),FY(I,J)
  ENDIF
*
  IF (  (FX(I,J).GT.0.0).OR.(FY(I,J).GT.0.0) ) THEN
  WRITE(2,154) FX(I,J),FY(I,J)
  ENDIF
*
153  CONTINUE
152  CONTINUE
154  FORMAT(1x,2F10.2)
*****************************************************************
  PRINT *
  PRINT *,'Simulation Complete'
  PRINT *
  CLOSE (Unit=2)
  STOP
   END
```

BIBLIOGRAPHY

Albini, Frank A., Wildfire Behavior and Effects, *General Technical Report INT-30*, USDA Forest Service, Ogden, Utah, pp. 92, 1976.

Albini, F.A., Thermochemical properties of flame gases from fine wildland fuels. *USDA Forest Service Research Paper INT-243*, Intermountain Forest and Range Experiment Station, Forest Service, USDA, pp.42, 1980.

Albini, Frank A., Wildland Fires, *American Scientist*, Vol. 72, 590-597, 1984.

Alexander, M.E., Estimating the Length-to-Breadth Ratio of Forest Fire Patterns in *Proceedings of the Eighth Conference on Fire and Forest Meteorology*, 287-304, 1985.

Anderson, Hal E., Sundance Fire: An Analysis of Fire Phenomena, *Research Paper INT-56*, U.S. Department of Agriculture, Forest Service, Ogden, Utah, 1968.

Anderson, H.E., Predicting the Wind-Driven Wild Land Fire Size and Shape, *Research Paper INT-305*, U.S. Department of Agriculture, Forest Service, Ogden, Utah, pp. 26, 1983.

Andreae, M.O., Biomass Burning: Its history, use and distribution and its impact on environmental quality and global climate in *Global Biomass Burning: Atmospheric, Climatic and Biospheric Implications* , edited by J.S. Levine, The MIT Press, Cambridge, MA, 3-21, 1991.

Andrews, P.L., BEHAVE: Fire Behavior Prediction and Fuel Modeling System – BURN Subsystem, *General Technical Report INT-194*, USDA Forest Service, 1986.

Anon, *U.S. Standard Atmosphere Supplements 1966*, U.S. Government Printing Office, Washington, D.C., 1966.

Anon, *FORTRAN-90 Version 4.5 Software*, Lahey Computer Systems Inc., Incline Village, NV, 1998.

Anon, USDA Forest Service, National Strategic Plan: Modeling and Data Systems for Wildland Fire and Air Quality, *General Technical Report, GTR-450*, pp.60, February 1999.

Anon, *PcModWin 4.0 Software*, Version 1.01, Ontar Corporation, North Andover, MA, June 2001.

Beer, Tom, The Speed of a Fire Front and its Dependence on Wind Speed, *International Journal of Wildland Fire*, Vol. 3 (4), 193-202, 1993.

Born, Max and Emil Wolf, *Principles of Optics*, New York, Pergamon Press, pp. 805, 1975.

Burgan, Robert E. and Richard C. Rothermel, BEHAVE: Fire Behavior Prediction and Fuel Modeling System – Fuel Subsystem, *General Technical Report INT-167*, USDA Forest Service, pp. 126, 1984.

Cabelli, C.A., D. E. Cooper, Y. Bai, J. D. Blackwell, L. J. Kozlowski, C. Y. Chen, G. L. Bostrup, J. T. Montroy, K. Vural, A. K. Haas, Latest results on HgCdTe 2048x2048 and silicon focal plane arrays, Rockwell Science Center, *SPIE Proceedings*, Vol. 4028, 2000.

Catchpole, E.A., N.J. de Mestre, and A.M. Gill, Intensity of Fire at its Perimeter, *Australian Forest Research*, Vol. 12, 47-54, 1982.

Chandler, A.C., P. Cheney, P. Thomas, L. Trabaud, and D. Williams, *Fire in Forestry: Forest Fire Behavior and Effects*, John Wiley, New York, 1983.

Cheney, N.P., J.S. Gould, and W.R. Catchpole, Prediction of Fire Spread in Grasslands, *International Journal of Wildland Fire*, Vol. 8 (1), 1-13, 1998.

Chorier, Philippe and Philippe Tribolet, High Performance HgCdTe SWIR Detector Development at Sofradir, *SPIE Proceedings*, Vol. 4369, 2001.

Christopher, Sundar A., Donna V. Kliche, Joyce Chou, and Ronald M. Welch, First Estimates of the Radiative Forcing of Aerosols Generated from Biomass Burning using Satellite Data, *Journal of Geophysical Research*, Vol. 101, D16, 21265-21273, 1996.

Christopher, Sundar A., Min Wang, Todd A. Berendes, and Ronald Welch, The 1985 Biomass Burning Season in South America: Satellite Remote Sensing of Fires, Smoke, and Regional Radiative Energy Budgets, *Journal of Applied Meteorology*, Vol. 37, 661-678, 1998.

Chuvieco, E. and M.P. Martin, A simple method for fire growth mapping using AVHRR channel 3 data, *International Journal of Remote Sensing*, Vol. 15, No. 16, 3141-3146, 1994.

Cofer, W.R. III, E.L. Winstead, B.K. Stocks, D.R. Cahoon, J.G. Goldhammer, and J.S. Levine, Composition of Smoke from North American Boreal Forest Fires. In *Fires in Ecosystems of Boreal Eurasia*, edited by J.G. Goldhammer and V.V. Furyaev, Kluwer Academic Publishers, Dordrecht-Boston-London, 465-475, 1996.

Crutzen, P.J., and M.O. Andreae, Biomass burning in the tropics: Impact on atmospheric chemistry and biogeochemical cycles, *Science*, 250, 1669-1678, 1990.

Dozier, J., A method for satellite identification of surface temperature fields of sub-pixel resolution, *Remote Sensing of the Environment*, Vol. 11, 221-229, 1981.

Fenn, R.W., S.A. Clough, W.O. Gallery, R.E. Good, F.X. Kneizys, J.D. Mill, L.S. Rothman, E.P. Shettle and F.E. Volz. Optical and Infrared Properties of the Atmosphere in *Handbook of Geophysics and the Space Environment*, edited by Adolph S. Jursa, Air Force Geophysics Laboratory, Chap. 18, 1985.

Finney, M.A., FARSITE: Fire Area Simulator – Model Development and Evaluation, *USDA Forest Service Research Paper RMRS-RP-4*, Ogden, Utah, pp. 47, 1998.

Flannigan, M.D., and T.H. Vonder-Haar, Forest fire monitoring using NOAA satellite AVHRR, *Canadian Journal of Forest Research*, 16, 975-982, 1986.

Flasse, S.P. and P. Ceccato, A contextual algorithm for AVHRR fire detection, *International Journal of Remote Sensing*, Vol. 17, No. 2, 419-424, 1996.

Fujioka, Francis M., Case Study of an Integrated Weather/Fire Spread Modeling Application in *Proceedings of the Fourth Symposium on Fire and Forest Meteorology*, American Meteorological Society, Boston, MA, 1-8, 2001.

Fuller, D.O. and M. Fulk, Comparison of NOAA-AVHRR and DMSP-OLS for operational fire monitoring in Kalimantan, Indonesia, *International Journal of Remote* Sensing, Vol. 21, No. 1, 181-187, 2000.

Giglio, L., J.D. Kendall, and C.O. Justice, Evaluation of global fire detection algorithms using simulated AVHRR infrared data, *International Journal of Remote Sensing*, Vol. 20, No. 10, 1947-1985, 1999.

Giglio, L., J.D. Kendall, and C.J. Tucker, Remote sensing of fires with the TRMM VIRS, *International Journal of Remote Sensing*, Vol. 21, No. 1, 203-207, 2000.

Hobbs, Peter V., et al., Particle and Trace-Gas Measurements in the Smoke from Prescribed Burns of Forest Products in the Pacific Northwest in *Biomass Burning and Global Change*, edited by J.S. Levine, The MIT Press, Cambridge, MA, Vol. 2, 697-715, 1996.

Hobbs, Peter V., Jeffrey S. Reid, Robert A. Kotchenruther, Ronald J. Ferek, and Ray Weiss, Direct Radiative Forcing by Smoke from Biomass Burning, *Science*, 275, 1776-1778, 1997.

Houghton, J.T., G.J. Jenkins, and J.J. Ephraums (eds.). *Climate Change: The IPCC Scientific Assessment*, pp. 362, Cambridge Univ. Press, New York, 1990.

Karafyllidis, Ioannis and Adonios Thanailakis, A Model for Predicting Forest Fire Spread using Cellular Automata, *Ecological Modeling*, Vol. 99, 87-97, 1997.

Kaufman, Y.J., C.J. Tucker and I. Fung, Remote Sensing of Biomass Burning in the Tropics, *Journal of Geophysical Research*, Vol. 95, 9927-9939, 1990.

Kaufman, Y.J., et al., Biomass burning airborne and spaceborne experiment in the Amazonas (BASE A), *Journal of Geophysical Research*, Vol. 97, 14581-14599, 1992.

Kaufman, Yoram J., and Robert S. Fraser, The Effect of Smoke Particles on Clouds and Climate Forcing, *Science*, 277, 1636-1639, 1997.

Kaufman, Yoram J., and Chris Justice, *Algorithm Theoretical Basis Document: MODIS Fire Products*, Version 2.2, pp. 77, November 10, 1998.

Kennedy, P.J., A.S. Belward, and J.M. Gregoire, An improved approach to fire monitoring in West Africa using AVHRR data, *International Journal of Remote Sensing*, Vol. 15, No.11, 2235-2255, 1994.

Kidwell, K.B., *NOAA Polar Orbiter Data User's Guide*, NOAA/NESDIS, Washington, D.C., 1991.

Killough, B.D., A Simplified Orbit Analysis Program for Spacecraft Thermal Design in *Proceedings of the SAE International Conference on Environmental Systems*, SAE Paper 972540, July 1997.

Kneizys, F.X., E.P. Shettle, W.O. Gallery, J.H. Chetwynd, Jr., L.W. Abreu, J.E.A. Selby, S.A. Clough, and R.W. Fenn, Atmospheric Transmittance/Radiance: Computer Code LOWTRAN 6, Air Force Geophysics Laboratory, *Technical Report 83-0187*, August, 1983.

Knight, Ian and John Coleman, A Fire Perimeter Expansion Algorithm Based on Huygens' Wavelet Propagation, *International Journal of Wildland Fire*, Vol. 3, No. 2, 73-84, 1993.

Kummerow, C., W. Barnes, T. Kozu, J. Shiue and J. Simpson, The tropical rainfall measuring mission (TRMM) sensor package, *Journal of Atmospheric and Oceanic Technology*, 15, 808-816, 1998.

Langaas, S. and K. Muirhead, Monitoring bushfires in West Africa by weather satellites in *Proceedings of the 22nd Symposium on Remote Sensing of the Environment*, Vol.1, Ann Arbor, Michigan: Environmental Research Institute of Michigan, 253-268, 1988.

Le Canut, Phillippe, Meinrat O. Andreae, Geoffrey W. Harris, Frank G. Wienhold, and Thomas Zenker. Aerosol Optical Properties over Southern Africa during SAFARI-92 in *Biomass Burning and Global Change*, edited by J.S. Levine, The MIT Press, Cambridge, MA, Vol.1, 441-459, 1996.

Lee, Thomas F. and Paul M. Tag, Improved Detection of Hotspots using the AVHRR 3.7-um Channel, *Bulletin American Meteorological Society*, Vol. 71, No. 12, 1722-1730, 1990.

Levine, J. S., *Global Biomass Burning: Atmospheric, Climatic and Biospheric Implications*, The MIT Press, Cambridge, MA, 1991.

Levine, J. S., Biomass Burning and the Production of Greenhouse Gases in *Climate Biosphere Interactions: Biogenic Emissions and Environmental Effects of Climate Change* edited by R.G. Zepp, John Wiley and Sons, 139-159, 1994.

Levine, J. S., The 1997 fires in Kalimantan and Sumatra, Indonesia: Gaseous and particulate emissions, *Geophysical Research Letters*, Vol. 26, No. 7, 815-818, 1999.

Levine, J. S., Gaseous and Particulate Emissions Released to the Atmosphere from Vegetation Fires in *Health Guidelines for Vegetation Fire Events: Background Papers* (K.T. Goh, D. Schwela, J. G. Goldammer, and O. Simpson, Editors), United Nations Environmental Program, World Health Organization, World Meteorological Organization, and Institute for Environmental Epidemiology, 284-298, 2000.

Levine, J. S., Global Impacts and Climate Change in *Forest Fires and Regional Haze in Southeast Asia* (P. Eaton and M. Radojevic, Editors), Nova Science Publishers, Inc., New York, 165-193, 2001.

Levine, J. S., W.R. Cofer, D.R. Cahoon, and E.L. Winstead, Biomass Burning: A Driver for Global Change, *Environmental Science and Technology*, Vol. 29, No. 3, 120A-125A, 1995.

Levine, J. S., et al., FireSat and the Global Monitoring of Biomass Burning in *Biomass Burning and Global Change*, edited by Joel S. Levine, The MIT Press, Cambridge, MA, 107-129, 1996a.

Levine, J. S., et al., Biomass Burning, Biogenic Soil Emissions, and the Global Nitrogen Budget in *Biomass Burning and Global Change* edited by Joel S. Levine, The MIT Press, Cambridge, MA, 370-380, 1996b.

Levine, J. S., D.R. Cahoon, W.R. Cofer, E.L. Winstead, and B.J. Stocks, Fire and the Production of Greenhouse and Chemically Active Gases in the Boreal Forests in *Sustainable Development of Boreal Forests* (A. I. Pisarenko, Editor), Federal Forest Service of Russia, Moscow, Russia, 54-60, 1997a.

Levine, J. S., et al., Southern African Savannas as a Source of Atmospheric Gases in *Fire in Southern African Savannas: Ecological and Atmospheric Perspectives*, Wits University Press, Johannesburg, South Africa, 135-160, 1997b.

Lobert, J.M. and J. Warnatz, Emissions from the Combustion Process in Vegetation in *Fire in the Environment: The Ecological, Atmospheric, and Climatic Importance of Vegetation Fires*, edited by P.J. Crutzen and J.G. Goldhammer, John Wiley and Sons Ltd., 15-51, 1993.

Martins, J. Vanderlei, et al., Particle Size Distributions, Elemental Compositions, Carbon Measurements, and Optical Properties of Smoke from Biomass Burning in the Pacific Northwest of the United States in *Biomass Burning and Global Change*, edited by J.S. Levine, The MIT Press, Cambridge, MA, Vol. 2, 716-732, 1996.

Matson, Michael, George Stephens and Jennifer Robinson, Fire Detection using data from the NOAA-N satellites, *International Journal of Remote Sensing*, Vol. 8, No. 7, 961-970, 1987.

Mazurek, M.A., W.R. Cofer, and J.S. Levine, Carbonaceous aerosols from prescribed burning of a boreal forest in *Biomass Burning: Atmospheric, Climatic and Biospheric Implications*, edited by J.S. Levine, Cambridge, MA, MIT Press, 258-263, 1991.

Merrill, D.F. and M.E. Alexander, *Glossary of Fire Management Terms,* 4th Edition, National Research Council, No. 26516, Ottawa, Ontario, Canada, 1987.

Miller, August, Mie Code AGAUS-82, U.S. Army Atmospheric Sciences Lab, *Contractor Report CR-83-0100-3*, pp. 43, 1983.

Noble, I.R., G.A.V. Bary, and A.M. Gill, McArthur's Fire-Danger Meters Expressed as Equations, *Australian Journal of Ecology*, Vol. 5, 201-203, 1980.

Pan, Jianmei, Infrared Fire Detection from a Geosynchronous Space Platform, *NASA Contract L-16582*, Rockwell Scientific, September 2002.

Peet, G.B., The shape of mild fires in jarrah forest, *Australian Forestry*, Vol. 31, 121-127, 1967.

Penner, Joyce E., Robert E. Dickinson, and Christine A. O'Neill, Effects of Aerosol from Biomass Burning on the Global Radiation Budget, *Science*, Vol. 256, 1432-1433, 1992.

Pereira, M.C. and A.W. Setzer, Spectral characteristics of deforestation fires in NOAA/AVHRR images, *International Journal of Remote Sensing*, Vol. 14, No. 3, 583-597, 1993.

Pereira, E.B., A.W. Setzer, F. Gerab, P.E. Artaxo, M.C. Pereira, and G. Monroe, Airborne measurements of aerosols from burning biomass in Brazil related to TRACE A experiment, *Journal of Geophysical Research*, Vol. 101, 23983-23992, 1996.

Prins, E.M. and W.P. Menzel, Geostationary satellite detection of biomass burning in South America, *International Journal of Remote Sensing*, Vol. 13, No. 15, 2783-2799, 1992.

Prins, Elaine M. and W. Paul Menzel, Trends in South American biomass burning detected with the GOES visible infrared spin scan radiometer atmospheric sounder from 1983 to 1991, *Journal of Geophysical Research*, Vol. 99, No. 8, 16719-16735, 1994.

Richards, Gwynfor D., An Elliptical Growth Model of Forest Fire and its Numerical Solution, *International Journal for Numerical Methods in Engineering*, Vol. 30, 1163-1179, 1990.

Richards, Gwynfor D., A General Mathematical Framework for Modeling Two-Dimensional Wildfire Spread, *International Journal of Wildland Fire*, Vol. 5, No. 2, 63-72, 1995.

Richards, Gwynfor D. and Robert W. Bryce, A Computer Algorithm for Simulating the Spread of Wildland Fire Perimeters for Heterogeneous Fuel and Meteorological Conditions, *International Journal of Wildland Fire*, Vol. 5, No. 2, 73-79, 1995.

Robinson, Jennifer M., Fire from Space: Global Fire Evaluation using Infrared Remote Sensing, *International Journal of Remote Sensing*, Vol. 12, No.1, 3-24, 1991.

Rosenfeld, D., TRMM observed first direct evidence of smoke from forest fires inhibiting rainfall, *Geophysical Research Letters*, Vol. 26, 3105-3108, 1999.

Ross, John L., and Peter V. Hobbs, Radiative characteristics of regional hazes dominated by smoke from biomass burning in Brazil: Closure tests and direct radiative forcing, *Journal of Geophysical Research*, Vol. 103, No. D24, 31925-31941, 1998.

Rothermel, R.C., A mathematical model for predicting the spread and intensity of forest and range fires, *Research Paper INT-115*, U.S. Department of Agriculture, Forest Service, Ogden, Utah, pp. 40, 1972.

Rothermel, R.C., How to predict the spread and intensity of forest and range fires, *General Technical Report INT-143*, U.S. Department of Agriculture, Forest Service, Ogden, Utah, pp. 53, 1983.

Rothermel, Richard C., Roberta A. Hartford, and Carolyn H. Chase, Fire Growth Maps for the 1998 Greater Yellowstone Area Fires, *General Technical Report INT-304*, U.S. Department of Agriculture, Forest Service, Ogden, Utah, pp. 63, 1994.

Sarlot, Roland J., Donald W. McCarthy, James H. Burge, Jian Ge, Optical design of ARIES: the new near infrared science instrument for the adaptive f/15 Multiple Mirror Telescope in *Proceedings SPIE 3779, Current Developments in Optical Design and Optical Engineering VIII*, edited by Robert E. Fischer and Warren J. Smith, Denver, CO, July 1999.

Setzer, A.W. and M.M. Verstraete, Fire and glint in AVHRR's channel 3: A possible reason for the non-saturation mystery, *International Journal of Remote Sensing*, Vol. 15, No. 3, 711-718, 1994.

Tennant, W.E. and C. Cabelli, HgCdTe - An Unexpectedly Good Choice for (Near) Room- Temperature Focal Plane Arrays, *Materials Research Society Symposium Proceedings*, Vol. 484, 1998.

Toffoli, Tommaso and Norman Margolus, *Cellular Automatat Machines*, MIT Press, Cambridge, MA, 1985.

Toon, O., and T. Ackerman, Algorithms for the calculation of scattering of stratified spheres, *Applied Optics*, Vol. 20, 3657-3660, 1981.

Tsai, Nancy Y., The Emissions and Effects of Global Biomass Burning: A study of the 1998 Siberian Boreal Forest Fires, *Senior Research Paper for B.A. in Environmental Studies*, Univ. of Chicago, May, 2000.

Van De Hulst, H.C., *Light Scattering by Small Particles*, New York, Dover Publications, pp. 470, 1981.

Vasconcelos, Maria J. and D. Phillip Guertin, FIREMAP – Simulation of Fire Growth with a Geographic Information System, *International Journal of Wildland Fire*, Vol. 2, No. 2, 87-96, 1992.

Vines, R.G., Physics and chemistry of rural fires in *Fire and the Australian biota*, edited by A.M. Gill, R.H Groves, and I.R. Noble, Canberra: Australian Academy of Sciences, 129-149, 1981.

Von Neumann, J., *Theory of Self-Reproducing Automata*, edited by A.W. Burks, Univ. of Illinois Press, Urbana, Illinois, 1966.

Waterman, J.R., M. R. Kruer, J. M. Schuler, D. A. Scribner, P. R. Warren, Multicolor focal plane technology for Navy applications in *Proceedings SPIE 4820, Infrared Technology and Applications XXVIII*, edited by Bjorn F. Andresen, Gabor F. Fulop, and Marija Strojnik, Seattle, WA, July 2002

Weise, D.R. and F.M. Fujioka, Comparison of fire spread estimates using weather station observations versus nested spectral model gridded weather in *Proceedings of the Second Conference on Fire and Forest Meteorology*, Phoenix, Arizona, American Meteorological Society, Boston, MA, 75-79, 1998.

Wertz, James R. and Wiley J. Larson, *Space Mission Analysis and Design*, 3rd Edition, Kluwer Academic Publishers, pp. 1010, September 1999.

Wolfram, Stephen, Cellular automata as models of complexity, *Nature*, Vol. 311 (4), 419-424, 1984.

VITA

Brian D. Killough, Jr.

Born in Abington, Pennsylvania, November 9, 1965. Graduated from Council Rock High

School in Newtown, Pennsylvania, June 1983. Graduated from the University of

Virginia with a B.S. in Mechanical Engineering, May 1987. Graduated from George

Washington University with a M.S. in Mechanical Engineering, May 1991. Employed

with the NASA Langley Research Center in Hampton, Virginia since May 1987 as an

Aerospace Engineer responsible for the engineering design, development and program

management of atmospheric science instruments and technology. Entered the Applied

Science Program at the College of William and Mary with a concentration in

Atmospheric Sciences, August 1997.